# THE ANNALS OF "DUNAREA DE JOS" UNIVERSITY OF GALATI

## Fascicle IX
## METALLURGY AND MATERIALS SCIENCE

# Table of Content

# ESTABLISHING THE ROLLING - FRICTION COEFFICIENT FOR DIFFERENT CONTACTS BETWEEN BALLS AND TERMOCHEMICALLY TREATED STEEL ROLLING PATHS

**Daniel MUNTEANU, Luminița PÂRV**
Transilvania University of Brasov, Romania
e-mail: muntean.d@unitbv.ro, lumiparv@unitbv.ro

## ABSTRACT

*Within the frame of this work, the influence of four very well-known and often used thermochemical treatments (carburizing, carbonitriding, nitriding and nitrocarburizing) of steel rolling paths applied on rolling-friction coefficient has been studied. The rolling - friction tests supposed different arrangements of the semi-couples (plates) and intermediary balls. Because of the difficulty in estimating the value (dimension) of the rolling friction coefficient, an equivalent static friction coefficient $\mu_0$ (at the start) was established for all the couples. According to the experimental results of this study, the carburized rolling paths seemed to offer the best conditions for rolling, the initial move appearing at the earliest. In addition, the presence of nitrogen and the possible $Fe_xN$ compounds on the contact rolling surface leads to an increased friction coefficient $\mu_0$. Finally, the study demonstrated that there is a slight tendency for a certain decrease in $\mu_0$ when increasing the intermediary balls diameter.*

KEYWORDS: rolling-friction coefficient, rolling-path, steel, ball, carbon, nitrogen

## 1. Introduction

### 1.1. Rolling – contact theoretical aspects

Bearings and gears commonly exhibit Hertzian point or line contacts when operated under rolling or rolling/sliding conditions. Even for constant loads, the rolling motion produces a variable superficial state of efforts characterized by normal and tangential-shear stresses.

The difficulty of researching into this kind of contacts is further increased by the presence of lubricants [1]. Thus, in this type of study several factors such as: load, speed, rolling-sliding ratio (if the sliding exists), lubricant presence and quality, surface topography etc. must be considered.

Generally, contact micro surfaces and higher pressures in the contact zones characterize the Hertzian rolling contact cases. Therefore, surface deformations must be taken into account. The appearance and evolution of surface fatigue phenomena have been theoretically explained in the literature using the *space stress state condition* and the models of Hertz and Boussinesq [1-3].

In this kind of contacts, wear processes of hardened steel surfaces usually occur in a mild way, in comparison with the unhardened surfaces. The Hertzian contacts are characterized by the appearance of a typical "material wave" on the rolling guide path, in front of the rolling body (ball or roll) [1-3]. Depending on the rolling-surface qualities and rolling body dimensions as well, this wave could be more or less important in size. Its appearance has an important role in rolling the rolling contacts because it leads to the development of a rolling-friction moment. This moment is in opposition with the rolling motion and plays an important role not only in the motion but also in the start-move.

If we consider a rolling contact in which the ball is harder than the rolling plane surface, an indentation cup on the contact zone will appear. This phenomenon leads to a specific material accumulation not only in front of the contact (where it is more consistent) but also behind the contact (see Fig. 1).

Very often, the practical physical explanations of the rolling-friction process take into account the plastic deformations appearance in the contact zone [1].

In fact, the rolling-friction process is characterized by a typical friction torque which gives a specific rolling - friction moment $M_{rf}$.
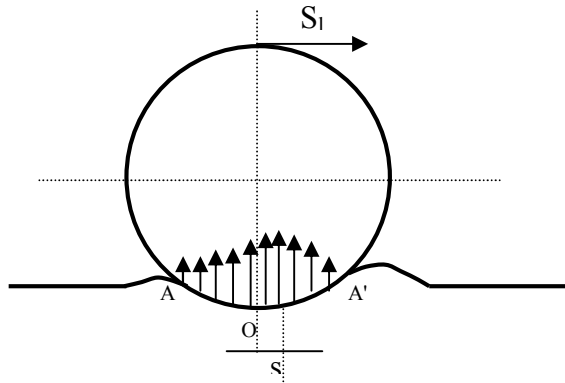


*Fig. 1. Schematic arrangement of a Hertzian punctual contact in plane coordinates; W – ball weight, N – result of typical force-reaction distribution on the contact zone AA', s – the reaction force's arm, $S_l$– the ball's linear speed*

According to Fig. 1, the reaction force $N$ on the AOA' section is given by an infinity of elementary forces. The general force-moment of these elementary forces related to the theoretical contact point $O$ is the rolling friction moment $M_{rf}$. These elementary reaction forces are not symmetrically distributed. Thus, in front of the contact, where more material is concentrated, the reaction forces are stronger. Owing to this reason, the elementary reaction forces result - $N$, generates the moment $M_{rf}$, which is opposite to the rolling sense of the ball [1]. The practical research discussed in the literature shows that for an equilibrium state, the value of this moment must be lower than a certain maximum value, as follows:

$$M_{rf} \leq s \cdot N \tag{1}$$

In relation (1), $s$ represents the rolling-friction coefficient. In comparison with the well-known sliding friction coefficient $\mu$ which does not have a dimension, the rolling-friction coefficient $s$ has a slight dimension which is very difficult to measure. It represents the maximum displacement distance of the normal reaction support $N$ compared to the theoretical contact point $O$ (see Fig. 1).

For static equilibrium conditions, (if we consider the rolling body harder than plane path support), when the rolling body (ball or role) is not moving and the rolling plane surface is in a perfectly horizontal position, the accumulation of material is symmetrically distributed in front and behind the ball.

However, for very little inclinations of the plane support, at rolling-move initiation, because the rolling-friction coefficient $s$ is very difficult to measure, the friction phenomenon can be evaluated considering ***the equivalent (conventional) sliding-friction coefficient $\mu_0$ at the start*** (see Fig. 2).
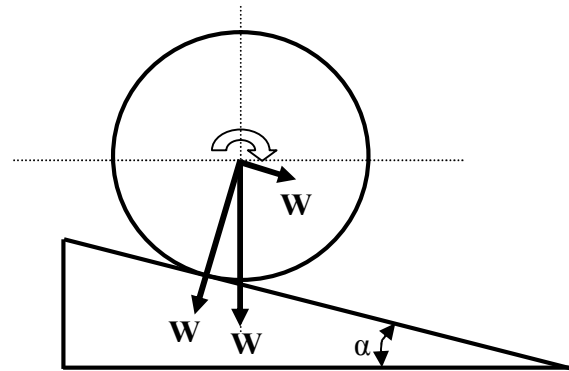


*Fig. 2. Schematic arrangement of rolling on an inclined plane (the ball weight and its components on normal and tangential directions)*

Thus, it is known that for the ball displacement guide paths, the necessary start-moving force of the mobile half-couple is bigger than the dynamic force which keeps the displacement-motion. In these conditions, the start-moving force can be estimated to be equal to the normal component ($W_n$) of load $W$ multiplied by the equivalent friction coefficient $\mu_0$ (see Fig. 2).

## 1.2. Diffusional thermochemical treatments

In practice on the other hand, there are certain applications in which this kind of contacts appears very often. One of the most important contacts refers to the case of bearings. For bearings manufacturing an alternative variant used in terms of materials is the replacement of the traditionally hypereutectoid bearing steels (e.g. AISI 52100 with 1% wt. C and 1.5 wt. Cr) with other cheaper steels in which the percentage of carbon is under 0,3. In order to be able to sustain Hertzian-contact solicitations, these low carbon steels have to be improved on the superficial contact path-regions, by means of various thermochemical treatments. The most important ones are carburizing and carbonitriding.

As it is known, carburizing is the addition of carbon to the surface of low-carbon steels at temperatures generally between 850 and 950 °C, at which austenite, with its high solubility for carbon, is the stable crystal structure. Carbonitriding is a modified form of gas carburizing rather than a form of nitriding. Typically, carbonitriding is carried out at a lower temperature and for a shorter time than gas

carburizing which produces a shallower case than the usual one obtained by carburizing [4-11].

In both cases, hardening is accomplished when the high-carbon surface layer is quenched to form martensite so that a high-carbon martensitic case with good wear and fatigue resistance is superimposed on a tough, low-carbon steel core.

These two superficial heat treatment variants are known in the field of heat-treating sector as high temperature thermochemical treatments and they always suppose each time a case hardening by quenching and low tempering.

There are also other practical applications which suppose certain mechanical properties in terms of high toughness for all bulk structure and this aspect supposes the use of heat-treatable steels for parts manufacturing. This means the use of steels with carbon content between 0.3 and 0.6 wt.%. These steels can offer, after the secondary bulk heat treatment, an excellent toughness to the part during dynamic work conditions. Very often, for this kind of steel-parts, in order to improve the superficial friction/wear properties, two successful variants of thermochemical treatments are used: the nitriding and the nitrocarburizing.

Nitriding is a surface-hardening heat treatment that introduces nitrogen into the surface of steel at a temperature ranging from 460 to 550 °C while it is in the ferrite condition. This is a thermochemical diffusion process where nitrogen, carbon, and to a very small extend oxygen atoms diffuse into the surface of the steel part, forming a compound layer at the surface, and a diffusion layer below. Nitrocarburizing is a shallow case variation of the nitriding process [4, 12-16]. Both procedures are performed mainly to provide an anti-wear resistance to surface parts and to improve fatigue resistance.

Although the rolling-friction contact has been studied very often in mechanics, there is not much information about the influence of a certain kind of rolling surface material on the evolution of rolling motion, especially in terms of the rolling-friction coefficient. Because of the difficulty to measure the rolling-friction coefficient, this paper tries to establish an equivalent friction coefficient value (at move-start) for different types of hertzian contacts (ball on carburized, nitrided, carbonitrided and nitocarburized plane steel surfaces) for rolling conditions.

## 2. Experimental aspects

### 2.1. The tribosystem

In order to establish the equivalent static friction coefficient value for all the sample combinations, a typical method such as the inclined plane was used. A home-made tribosystem, inclined – plane type

(schematically shown in Fig. 3), have been used to estimate the friction coefficient value based on some typical linear size measurements [17-19]. Thus, according to Fig. 3, for a plane-contact area between two bodies (the base one being fixed) the correlation between the friction angle $\alpha$ and the friction coefficient $\mu$ is:

$$tg\alpha = \mu \tag{2}$$

The system allows a plane inclination of the friction couple (that is in a rest state), with variable angles, until the sliding phenomenon appears in the couple.
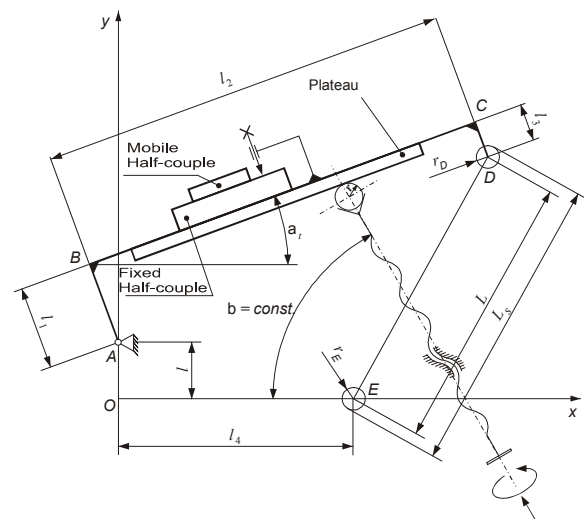


**Fig. 3.** *The inclined plane tribosystem based on linear measurements (schematic arrangement)* [17- 19]

According to equation 2, the angular value $\alpha_{limit} = \alpha_0$ where the sliding appears (at the start moment), is in direct correlation with the static sliding-friction coefficient $\mu_0$ at the start, according to:

$$tg\alpha_0 = \mu_0 \tag{3}$$

In order to test different pairs of half-couples on the system plateau it is possible to mount the driving (fixed) semi-couple by means of some clamping claws.

The lowering of the tribosystem driving plate $p$ is achieved with a motion screw to which is fitted an inclined axis nut fillet, whose inclination is under 60°. The screw inclines the driving plate $p$ through a ball $r$. The ball is situated inside a cone-shaped socket at the head in the screw. The driving plate $p$ leans against the ball by means of a plane section which is perfectly parallel to the surface which the fixed semi-couple is placed on. The establishment of the driving

plate $p$ slope is given by the $L_S$ size measurement (between the pins D and E which are characterized by $r_D$ and $r_E$ radius – Fig. 3) in accordance with a non-linear function [17-19]:

$$\alpha_0 = 2arctg \frac{-C_2 + \sqrt{C_2^2 - (C_1 - L^2)^2 + C_3^2}}{C_1 - C_3 - l^2} \qquad (4)$$

where:

$$L = L_S - r_D - r_E$$
$$C_1 = l_2^2 + (l_1 - l_3)^2 + l_4^2 + l_5^2$$
$$C_2 = 2l_4(l_1 - l_3) + 2l_2 l_5$$
$$C_3 = 2l_5(l_1 - l_3) - 2l_2 l_4$$

For practical applications, and for different values of $L_s$, the non-linear function values can be computer-assisted. Thus, in accordance with the measured length it is possible to find the static friction coefficient directly. The measurement of $L_s$, has been carried out by means of a digital micrometer.

## 2.2. The rolling-couples

In order to measure the equivalent friction coefficient (at start) by means of inclined plane method, special pairs of rolling-motion couples have been designed and manufactured (see Figures 5 and 6). In these rolling-motion couple systems, each semi-couple has a parallelepiped form, with 141x100x15 mm (see Fig. 4) and three identical longitudinal parallel V-guide paths on the rolling - friction surface.
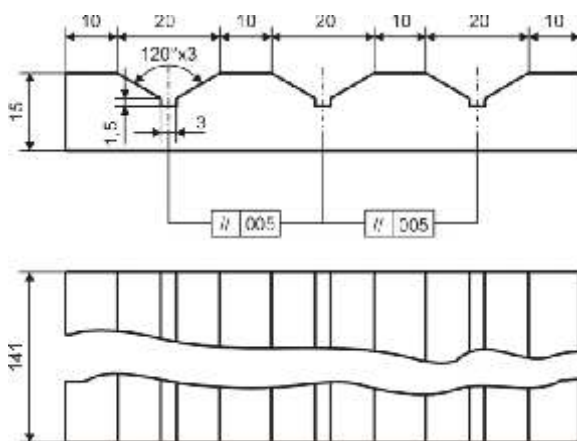
**Fig. 4.** *The schematic drawing of the semi-couples with longitudinal V-guide paths* [17, 18]

The rolling - friction tests supposed different arrangements of the semi-couples and balls (see Fig. 5a, b). In this configuration, the upper plate is moving on the lower one (stationary) by means of the identical three balls.

Thus, sets of three identical balls of different sizes have been used. They measure 8, 10, 12, 15.9, 18, 19.8, 22, 25 and 26 mm in diameter, are manufactured from ball-bearing steel (AISI 52100) hardened and low tempered and have a final hardness value of 63 HRC and final roughness $R_a$ = 0.04 μm.

**Fig. 5. (a, b)** *Details on the rolling-contact elements: a) the set of 3 identical balls; b) the whole rolling couple*

Each rolling-friction couple was fixed in a perfectly horizontal position of start by means of a horizontal level dial-gauge on the tribosystem base plateau (see Fig. 6).

**Fig. 6.** *The rolling couple arrangement*

## 2.3. The contact surfaces: steels and thermochemical treatments

The steels used in the manufacture of the rolling-motion couples are: 5115 AISI case-hardening steel (0.17% C, 0.30% Si, 1.20% Mn, 0.90% Cr) and 4140 AISI heat-treatable steel (0.41% C, 0.30% Si, 0.70% Mn, 1.10% Cr, 0.20% Mo).

The lower (stationary) semi-couples were thermochemically treated. It is important to mention here that the upper-mobile semi-couple was the same in all the tests, being manufactured from 4140 AISI heat-treatable steel. This choice was made in order to prevent a possible influence of a small mass difference of the upper semi-couples on the rolling-friction tests. The experimental program supposed 6 couple variants for rolling-friction tests. Table 1 presents the steels used for preparing the six different lower semi-couples and the thermochemical treatments applied of the rolling paths.

**Table 1.** *The stationary semi-couple types used in the experimental program*

| The lower semi-couple | Steel | The type of thermochemical treatment |
|---|---|---|
| A. | 5115 AISI case-hardening steel | Carburizing |
| B. | 5115 AISI case-hardening steel | Carbonitriding |
| C. | 4140 AISI heat-treatable steel | Nitriding |
| D. | 4140 AISI heat-treatable steel | Nitrocarburizing |
| E. | 5115 AISI case-hardening steel (annealed state) | Without thermochemical treatment |
| F. | 4140 AISI heat-treatable steel (tempered state) | Without thermochemical treatment |

The carburizing and carbonitriding procedures were conducted in a gas-tight multi-purpose chamber furnace with an integrated double-walled oil quench bath and a mixture of endothermic atmosphere (90%) and $CH_4$ (10%), at 920$^o$C for carburizing and a mixture of endothermic atmosphere (85%), $CH_4$ (10%) and $NH_3$ (5%), at 870$^o$C for carbonitriding. In both cases, the carbon potential in the furnace chamber was kept at 1.1% and the maintaining period at the treatment temperature (in the main diffusion phase) was 7 hours for each treatment. After the thermochemical treatments, the samples were slowly cooled till 820$^o$C and then case hardened (from 820$^o$C) in oil-like quenching agent.

Finally, both types of samples were low tempered at 180$^o$C for 2 hours.

The gas-nitriding process supposed a single diffusion phase at 530$^o$C, for 20 hours in 50% $NH_3$ + 50% $N_2$ atmosphere, $NH_3$ dissociation rate α = 25%. The gas − nitrocarburizing treatment was conducted at 560$^o$C, for 5 hours in 50% endothermic gas + 50% $NH_3$ atmosphere, with $NH_3$ dissociation rate of 40%. Before nitriding and nitrocarburizing, the semi-couples were hardened (from 840$^o$C) in oil like quenching agent and high tempered at 550$^o$C for 2 hours. After tempering, the semi-couples were finely polished.

Two lower plates for each category of treatment type were used for the bottom (fixed) semi-couple. According to the description of this method 10 rolling-friction tests were performed for each variant: 5 in one direction and 5 abeam so that the one-way roughness should not influence the movement of the samples. 120 tests for each couple type and 1080 tests in total were performed for all the samples (taking into account the 9 sets of balls). In each case, the utmost values were eliminated.

The results discussed in section 3 represent these final average values. Before all the tribological tests, the semi-couples and the balls were first degaussed and then alkaline cleaned and wiped. The environmental conditions of the tribological tests were: T = 20.5$^o$C and 63% humidity.

## 2.4. The friction coefficient (plane contact) – parallel measurements

In order to have enough information on the influence of the surface material nature on the equivalent static friction coefficient value, small parallel parallelepiped samples (PS) were prepared. These samples were used to establish the static friction coefficient (plane on plane) in order to compare the friction tendencies both for rolling/plane and plane/plane contacts. Their dimensions were 20x10x5 mm, they were manufactured from ball-bearing steel (AISI 52100) which was next hardened, low tempered and fine-polished. These PSs were manufactured from the same material (steel) and had the same final hardness value and aproximatively the same roughness as the balls. These tests were performed for each couple, between the PSs and the flat surface placed between two of the longitudinal V-guide paths and this resulted in the frictional movement being parallel to the longitudinal axis of this V-path. Except for the number of balls, the number of the tests in this case was the same as that in the rolling tests: 60 for all the couples.

## 2.5. Hardness and roughness measurements

The surface hardness values of the thermochemically treated surfaces were established by means of microhardness-equipment FM-700 at a load of 100 g (HV0.1). The roughness values of the surfaces were also established based on the profilometer method with a TR-220 portable roughness tester.

## 3. Experimental results and discussion

### 3.1. Equivalent rolling – friction coefficient

Figures 7, 8 and 9 present the equivalent rolling-friction coefficient values registered for all the couple types considered in the experimental program. The same conclusion is valid if we consider, for each type of rolling-contact couple, the medium value of friction coefficient reported to all ball sizes (Fig. 9a).
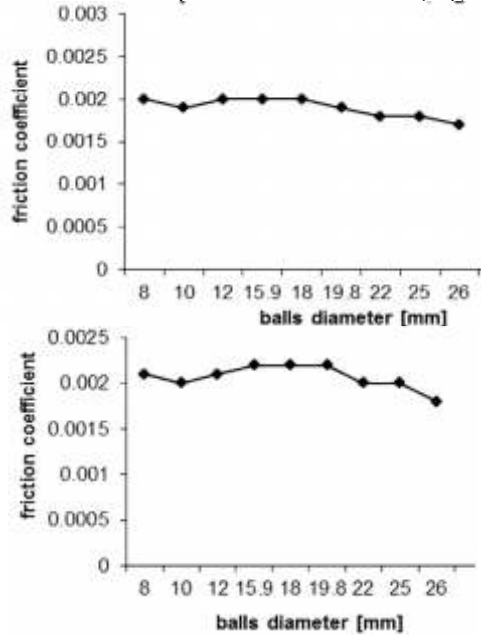


**Fig. 7. (a, b)** *The equivalent rolling-friction coefficient (average values) for different ball set sizes in contact with carburized (a) and carbonitrided (b) surfaces (A, B variants-Table 1)*
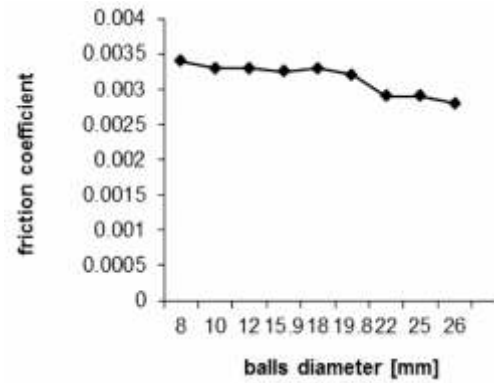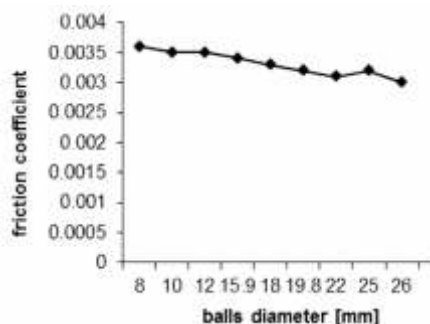


**Fig. 8. (a, b)** *The equivalent rolling-friction coefficient (average values) for different ball set sizes in contact with nitrided (a) and nitrocarburized (b) surfaces (C, D variants-Table 1)*
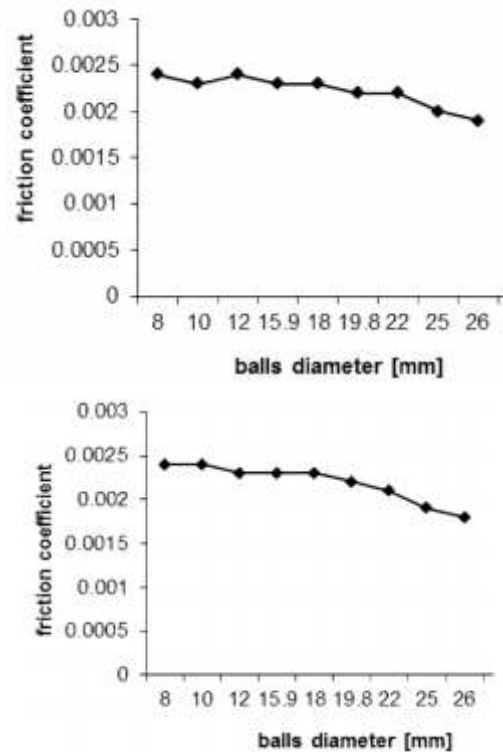


**Fig. 9. (a, b)** *The equivalent rolling-friction coefficient (average values) for different ball set sizes in contact with uncoated steels, 5115 AISI annealed conditions (a) and 4140 AISI hardened and high tempered (b) surfaces (E, F variants – Ttable 1)*

Although the input of nitrogen is not considerably related to carbon, in the case of high temperature thermochemical treatments like carbonitriding, its presence leads to a slow increasing tendency of the friction coefficient value.

These friction coefficient values are lower but almost comparable to the ones obtained for non-treated steel rolling paths. However, the major advantage for the carburized variants is the path's hardness, considerably higher in comparison with the non-treated ones.

Regarding the rolling contacts on the nitrided and nitrocarburized paths, here the experimental results revealed the maximum values for the friction coefficient and a visible increase by comparison with the remaining variants.

### 3.2. Hardness, rolling-surface nature and roughness

Taking into account all the results related to equivalent friction coefficient, there are a few parameters that are worth mentioning and discussed here: firstly, the evolution of rolling-path hardness, secondly the nature of the rolling–path surface-material influenced by the thermochemical treatment and thirdly, the rolling–path surface roughness. All these three aspects have to be correlated to the experimental values registered for equivalent rolling – friction coefficients.

Table 2 presents the average experimental values of roughness $R_a$ and Vickers hardness for all the sample categories, after removing the extreme values for each kind of measurement.

**Table 2.** *The roughness and micro-hardness ($HV_{0.1}$) values of the rolling-contact surfaces*

| Sample surfaces | Roughness average values $R_a$ [μm] | Vickers Hardness (on surface top) $HV_{0.1}$ |
|---|---|---|
| Carburized rolling path (5115 AISI) | 0.42 | 796 |
| Carbonitrided rolling path (5115 AISI) | 0.46 | 820 |
| Nitrided rolling path (4140 AISI) | 0.58 | 876 |
| Nitrocarburized rolling path (4140 AISI) | 0.52 | 588 |
| Untreated steel (annealed steate) – 5115 AISI | 0.56 | 348 |
| Untreated steel (tempered state) – 4140 AISI | 0.44 | 393 |

All hardness values of thermochemically treated paths are normal and comparable to others registered in different experimental or practical procedures involving these kinds of superficial treatments [5-11]. The hardness values registered for the high-temperature diffusion treatments (after case hardening and low tempering processes) are not very different, with a plus for carbonitrided surfaces. This aspect could be explained by taking into account the formation during the carbonitriding process of very hard and dense compounds, Fe(C,N) and Cr(C,N) types, which are known to be harder in comparison with the correspondent carbon compounds Fe-C and Cr-C.

Regarding the hardness, the nitriding process gives the steel surface the maximum value; these aspects are in accordance with other well-known results in terms of nitriding and they could be explained by taking into account the long diffusion time and the development of a very dense and hard compound layers zone (known in the nitriding practical applications as "the white layer") – $Fe_4N$ (the γ' compound) and possible $Fe_{2-3}N$ (the ε compound) [12, 13, 15, 16, 20, 21]. The nitrocarburizing represents a shorter-time process; it usually builds up a thin compound layer on the surface of the steel, which consists essentially of ε - phase iron carbonitride, below which there is a non-consistent diffusion region.

In terms of the nature of rolling – path surface-material, in Fig. 10a, it can be seen that the best rolling-friction behavior is provided by the paths with the highest carbon contents. This reveals the importance of the rolling–surface composition and the solid lubricant effect of carbon. The appearance of nitrogen in the composition of surface–rolling paths is correlated with the increase of the friction coefficient (see Fig. 11a). Here the worst behavior is registered for the nitrided paths where carbon is missing.

According to the roughness results in Table 2 and related to the non-treated steel surfaces, it is clear that the diffusion processes based mainly on carbon lead to the decrease of the surface roughness ($R_a$ from 0.56 to 0.42 for carburizing and 0.46 for carbonitriding). In an opposite sense, the enriching in nitrogen by diffusion increases the steel surface roughness, from 0.44 to 0.58 for nitriding and 0.52 for nitrocarburizing. The presence of carbon close to nitrogen in the diffusion process diminished this tendency of roughness increase. An increase in surface roughness after nitrocarburizing was also observed by Qiang in [22].

Thus, one may conclude than indeed the rolling – path roughness and the rolling - path surface-material nature may play important roles in the variation of the friction coefficient. At the same time, we could conclude that all surface treatments

achieved on the samples examined in this study contribute to the superficial hardness enhancement and to the minimizing of rolling path deformations. For this reason, if we consider the surface deformation of the treated rolling paths in the contact region, when the superficial hardness increases the contact area could decrease and the contact pressure could become higher. Although these increased pressures should contribute to flatten the roughness and to start the balls earlier on the treated surfaces, this process is not unfold. In this sense, the nitriding paths case is illustrative. Related to this, Xiao reported in [23] a study on the influence of surface roughness and the pressure distribution on the frictional behaviour in rolling/sliding contacts. He showed that the friction coefficient increases linearly with increasing contact pressure up to a maximum limit above which the friction coefficient is constant. Regarding nitriding, this observation is in accordance with the present experimental work results (maximum friction coefficient for nitriding), where the maximum hardness could explain the minimum deformation of surface rolling – path and the increased contact pressure.
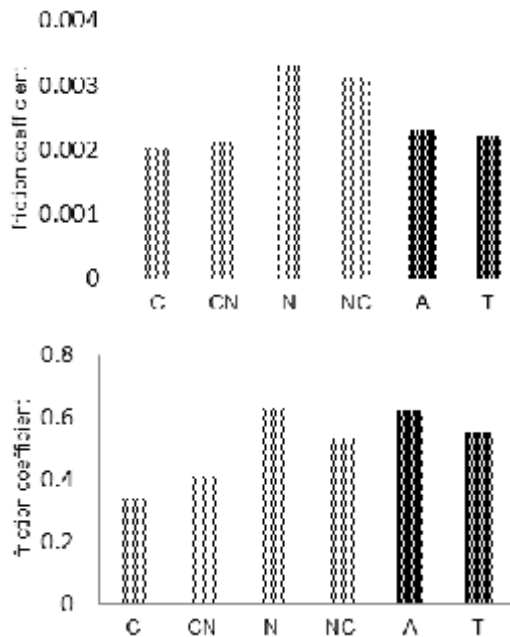


**Fig. 10. (a, b)** *The medium value of equivalent rolling-friction coefficient for the smallest ball diameter: balls in contact with different thermochemically treated plane rolling paths (a) and the friction coefficient for the plane contact between PSs and the same different plane rolling paths (b); C–carburized, CN–carbonitrided, N–nitrided, NC–nitrocarburized, A–annelead, T–tempered*

According to these aspects, the hardness could not be taken into consideration like a main parameter to explain the variation of the equivalent rolling-friction coefficient. Besides, if the rolling-surface deformations are not taken into account, the increased roughness of the treated surfaces seems to have a strong enough and dominant influence on balls start movement. This is in accordance with the registered values for roughness of carburized (the minimum ones) and of nitriding (the maximum ones) rolling paths and the correspondent friction coefficients (Table 1, see Figures 7a, 8a and 10a). Moreover, in the case of parallel measurements performed with PSs (see Fig. 10b).

In fact, the parallel measurements performed on PSs are in accordance with the ones obtained for the rolling contacts (see Fig. 10b).

However, in this case, there is a very small difference between the friction coefficients registered for non-treated paths and the nitrided ones. At the same time, for this type of plane contact, the lower value of friction coefficient is visible in comparison with the remaining variants. Its variation shows a straight dependence on the steel surfaces particular composition (and consequently their structural features), namely that of C. Besides the solid lubricant role that this carbon could be playing, one must consider that this moderate roughness value could give the contact the best conditions for friction.

## 4. Conclusions

This work presents an experimental procedure for establishing the rolling–friction coefficient for certain contacts that suppose steel balls and thermochemically treated rolling steel paths. The rolling motions were realised by balls on a steel plateau with longitudinal V-guide paths. The difficulty in measuring the rolling friction coefficient could be avoided if the friction phenomenon is evaluated considering *the equivalent (conventional) sliding-friction coefficient at start.* In order to establish the equivalent friction coefficient value, a typical method such as the inclined plane slope was used.

The best conditions for rolling seem to be provided by the carburized paths while the nitrided paths worsen this movement.

Taking into account our experimental conditions and results, we conclude that both nature (composition) of material and surface roughness are able to influence the equivalent rolling-friction coefficient. Although the non-treated steel paths revealed a good tendency for rolling, it is important to notice the role of superficial hardness and the strengthening of the rolling paths provided by the

superficial treatments on the fatigue phenomena typical for Hertzian rolling contacts.

# References

[1]. **Popinceanu N, Gafitanu M.** - *The basic problems of the rolling contact*, Bucharest: Technical Publishing House, 1985.

[2]. **Pavelescu D.,** *Tribotechnics*, Bucharest: Technical Publishing House, 1983.

[3]. **Pavelescu D., Tudor A.** - *Tribology*, Bucharest: Pedagogical and Didactical Publishing House, 1980.

[4]. **\*\*\*,** http://steel.keytometals.com/articles.

[5]. **Munts V. A., Baskatov A. P.** - *Rate of carburizing of steel*, Metal Science and Heat Treatment (English Translation of Metallovedenie I TermicheskayaObrabotkaMetalov), 1983, 25, p. 98-102.

[6]. **Moiseev B. A., Brunzel Y. M., Shvartsman L. A.** - *Kinetics of carburizing in an endothermal atmosphere, Metal Science and Heat Treatment*, (English Translation ofMetallovedenie I TermicheskayaObrabotkaMetalov), 1979, 21, p. 437-442.

[7]. **Totten G. E., Howes M. A. H.** - *Steel Heat Treatment*, Handbook, NewYork: Marcell Dekker Inc., 1997.

[8]. *Surface Hardening of Steel*, ASM International. Materials Park. Ohio, 2002.

[9]. *ASM Handbook*. ASM International. Materials Park. Ohio, 1991.

[10]. **Slycke J., Ericsson T.** - *A study of reactions occurring during the carbonitring process*, Journal of Heat Treating, 1981, 2, p. 3-19.

[11]. **Slycke J., Ericsson T.** - *A study of reactions occurring during the carbonitring process*, Part II. Journal of Heat Treating, 1981, 2, p. 97-112.

[12]. **Pye D.** - *Practical nitriding and ferriticnitrocarburizing*, ASM International, Materials Park, Ohio, 2003.

[13]. **Somers M. A. J., Mittemeijer E. J.** - *Layer-grow kinetics on gaseous nitriding of pure iron: Evaluation of diffusion coefficients for nitrogen in iron nitrides*, Metallurgical and Materials Transactions A, 1995, 26, p. 57-74.

[14]. **Somers M. A. J., Mittemeijer E. J.** - *Modeling the kinetics of the nitriding and nitrocarburizing of iron*, Heat Treating 1997, Proceedings of the 17th Conference ASM International, 1998, p. 321-330.

[15]. **Maldzinski L., Liliental W., Tymowski G., Tacikowski J.** - *New possibilities for controlling gas nitriding process by simulation of growth kinetics of nitride layers*, Surface Engineering, 1999, p. 15:377-384.

[16]. **Sola R., Giovanardi R., Veronesi P., Poli G.** - *Improvement of wear and corrosion resistance of ferrous alloys by post – nitrocarburizing treatments*, Metalurgical Science and Technology, 2011, 29-2, p. 14-24.

[17]. **Bobancu S., Cozma R., Cioc V.** - *Tribology and Inventics - Practical Applications*, Brasov, Transilvania University Publishing House, 2000.

[18]. **Cozma R., Bobancu S., Cioc V.** - *Equipment and devices for tribological characterizations*, Bucuresti, Matrix Rom, 2005.

[19]. **Munteanu D., Vaz F.** - *Tribological researches on rolling – friction coefficient for carburized and carbonitrided steel surfaces*, Journal of the mechanical behavior of materials, 2005, 16, p. 407-418.

[20]. **Somers M. A. J.** - *Thermodynamics, kinetics and microstructural evolution of the compound layer; a comparison of the states of knowledge of nitriding and nitrocarburizing*, Heat Treatment of Metals, 2000, 4, p. 92-102.

[21]. **Du H., Somers M. A. J., Agren J.** - *Microstructural and compositional evolution of compound layers during gaseous nitrocarburizing*, Metallurgical and Materials Transactions A, 2000, 31, p. 195-211.

[22]. **Qiang Y. H., GE S. R., Xue Q. J.** - *Microstructure and tribological behaviour of nitrocarburizing - quenching duplex treated steel*, Tribology International, 1999, 32, p. 131–136.

[23]. **Xiao L., Bjorklund S., Rosen B. G.** - *The influence of surface roughness and the contact pressure distribution on friction in rolling/sliding contacts*, Tribology International, 2007, 40, p. 694–698.

# CHALLENGES IN CORROSION PROTECTION USING VEGETABLE EXTRACTS AS INHIBITORS - ELECTROCHEMICAL STUDIES

**Lidia BENEA[1], Eliza Mardare DĂNĂILĂ[1], Iulian BOUNEGRU[1,2]**

[1]Research (Competences) Centre: Interfaces-Tribocorrosion and Electrochemical Systems (CC-ITES),
Faculty of Materials and Environmental Engineering, Dunărea de Jos University of Galati,
47 Domnească Street, RO-800008, Galati, Romania
[2]Research (Competences) Centre: Interfaces-Tribocorrosion and Electrochemical Systems (CC-ITES),
Faculty of Medicine and Pharmacy, Dunărea de Jos University of Galati, 47 Domnească Street,
RO-800008, Galati, Romania
e-mail: Lidia.Benea@ugal.ro

## ABSTRACT

*Corrosion is an irreversible chemical or electrochemical reaction of a material with its surrounding environment or medium which results in consumption of the material or in dissolution into the material of a component of the environment. Corrosion can provoke severe and expensive destructions in any field of activity from transportation, home appliances, water and gas alimentary systems, energy production systems, chemistry, metallurgy, semi-finished production, bridges and public buildings, etc. The main important reasons of corrosion phenomena study are: economics, safety and conservation. The economic point of view includes the cost of material losses resulting from the above activity fields and may involve piping, tanks, ships, hulls, marine structures, etc. The corrosion costs also include the losses of energy and water reserves accompanying the production of metals and the need for expensive replacements for the corroded ones. Unexpected failures of equipment and devices because of weakening of structures induced by corrosion may reduce the safety criterion, which in the design of equipment for nuclear power plants and for disposal of nuclear wastes is critical. The effects of corrosion on the safe, reliable and efficient operation of equipment or structures are often more serious than the simple loss of a mass of metal. Finally, the third important consideration for which the corrosion phenomena must be studied is conservation of mineral and metal resources, whose world supply is limited. Several techniques have been applied to protect metallic structures against corrosion. One of the most important methods in that regard is the use of corrosion inhibitors. A corrosion inhibitor is a chemical substance that, when added in small concentration to an environment effectively prevents or decreases the corrosion rate. Inhibitors slow down the corrosion process by: increasing the anodic or cathodic polarization behavior, reducing the movement or diffusion of ions to the metallic surface and increasing the electrical resistance to the metallic surface. The paper presents some experimental results with vegetable extracts acting as corrosion inhibitors for carbon steel and copper in acidic and neutral environments.*

KEYWORDS: corrosion, corrosion protection, green inhibitor, electrochemical methods, eco-friendly pickling process

## 1. Introduction

**Technical and economic aspects of corrosion:** Corrosion is one of the main causes of the accelerated degradation of metal constructions, a destructive process which tales place by modifying the surface geometry, through structural and chemical transformations of a metal material [1]. Corrosion phenomena occurr in various aspects and in various environments: in air, water, soil, industrial plants [2].

For the contemporary world economy, corrosion has become one of the acute problems to face. The

high development rate of the modern industry involves high consumption of construction materials, among which the most important are ferrous metals and alloys; on the other hand, the crisis of raw materials occurring nowadays makes it imperative the restriction of metals use, their reasonable use, their saving.

Corrosion phenomena are significantly present not only in industry but also in other economic sectors and even in everyday life, especially under current pollution. The negative economic consequences of corrosion are briefly called *corrosion cost*.

Apart from the losses of metal as such permanently unrecoverable, corrosion causes frequent interventions to ensure uninterrupted operation, for repairing or replacing parts or machinery along with production losses caused by these interventions.

The negative economic consequences of corrosion are briefly called *corrosion cost*.

Estimation of the corrosion cost assumes clear and systematic records of both expenses and incurred losses caused by the corrosive degradation of the metal constructions.

Although in recent years there has been a high development of the protection methods such as the use of coatings, however, the rapidly developing method over the past 20 years has been the method of corrosion protection by means of inhibitors extending the area of application fields and the technical and variety of the products used. This method, in addition to being the most adequate method of protection of the plants in operation, has other advantages as well: simplicity of the solution in terms of its practical application (installations do not raise technical, maintaining or operating difficulty issues); it provides uniform protection of the whole surface in contact with the inhibitor; economy due to lower consumption of metallic materials, because in most cases use is made of conventional steel alloys, carbon steels, that are cheap, affordable and easy to process, etc.

To illustrate the advantage of the simplicity of the corrosion inhibitor treatment facilities on drilling and extraction equipment it should be noted that these inhibitors can be relatively easily introduced into wells (including old ones) and can get to any place on metal surfaces exposed to aggressive fluids, including depth machinery.

On the definition of corrosion inhibitors, experts in the field are unanimous that these are chemicals which added to the aggressive (corrosive) environment slow or stop the corrosion processes. The corrosion inhibitors are used in small amounts, calculated to the aggressive environment, namely at a concentration of 0.005 to 0.5%, which economically justifies the adoption of the solution of the corrosion

protection of metallic materials by using corrosion inhibitors. Therefore, the corrosion inhibitors can not be mistaken for agents of stoichiometric deactivation of the corrosive environment, as a result of neutralization reaction, oxygen blocking, etc. although they finally have a positive effect on the protection of materials. It is obvious that in the latter case, consumption of chemicals is very high (maximum) as imposed by the chemical reaction that occurs to disable the aggressive agent.

Corrosion inhibitors act on a variety of metals but especially on alloys of iron and zinc, which are frequently used as materials in machinery manufacturing and industrial installations in recent years due to the development of metallurgy alloys of Cr, Ni Mo as imposed by certain conditions of temperature and environments under specific technological processes; as a result of all these, the issue of corrosion protection in the case of these types of alloys became necessary. It is obvious that in such conditions, the problems of the mechanism of inhibitors action and their types are different from the case of protection of carbon steel alloys.

With respect to aggressive environments the most often encountered in industrial practice to be inhibited are hydrochloric acid, sulfuric acid, nitric acid, hydrofluoric acid, citric acid, sulfanilic acid, or mixtures of them in various concentrations.

In the attempt to find the eco friendly corrosion inhibitors, there is a growing trend to use natural products such as plants, spices, vegetable peels, seeds etc, as corrosion inhibitors. This is because these natural products serve as a rich source of naturally synthesized chemical compounds which are environmentally acceptable, inexpensive, readily available and renewable sources of materials [5-11].

The objectives of this work are the followings: laboratory experiments to assess the effectiveness of the inhibitor Usinhib (from a vegetal extract) in a hydrochloric acid environment by electrochemical methods and Vegetal inhibitor efficiency calculation. The results will asses a **new eco-friendly anti-corrosion inhibitor.**

Electrochemical testing of inhibitors shows a major advantage, namely, short time of measurement while providing vital information on the mechanism of inhibition. Corrosion rate can be measured in minutes, while the weight loss methods can take days. Inhibitors protect by changing anode or cathode reactions thus forming a barrier between the metal and the electrolyte or a combination of both.

Corrosion inhibitors in acidic media are important in the pickling of metals covered with oxides. During pickling operations, oxide layers, thinner and slightly soluble, are removed before the thicker and poorly soluble layers. Consequently, part of the base metal is attacked before the pickling

operations are completed. In order to reduce attack by acids, special adsorption organic inhibitors are used. Because the majority of organic compounds are toxic nowadays, the obtaining and testing of vegetal extract were approached in the work (USINHIB) as a green inhibitor.

## 2. Experimental procedures

### 2.1. Materials and methods

The tested material selected for study is mild steel, whose composition (wt.%) was 0.16 C, 0.53 Mn, 0.30 Si, <0.045 P, <0.055 S, and Fe balance.

The test solution was 0.5 M Hydrochloric acid (HCl) considering the importance of pickling of steel foils in this media.

The mild steel samples with a rectangular shape of 50 mm x 20 mm x 1.5 mm were connected with a protected copper fill in order to be used as working electrode in an electrochemical cell. Prior to the measurements, the samples were degreased ultrasonically in ethanol and acetone, and dried at room temperature. Insulation resin was used to separate well the active surface area.

As inhibitor it was used a vegetable extract called USINHIB in different concentration.

The electrochemical cell used is formed by: double-walled glass vessel to maintain a constant temperature, electrode connection system to the electrochemical equipment, the working electrode (WE), which is always the sample being analyzed, reference electrode against which all potentials (RE) are measured. The RE used was Ag/AgCl (saturated KCl) that has the stable potential value of +199 mV against normal hydrogen electrode (NHE).As auxiliary electrode (CE) it was used a platinum-rhodium mesh. Auxiliary electrode or counter - electrode should be inert in relation with the tested solution. The electrochemical measurements applied were: Free potential E (t), time variation of the electrode potential (WE) in open circuit, determination of the polarization resistance, Rp, and corrosion rate by linear polarization around OCP with ± 50 mV and potentiodynamic polarization curves with a potential sweep rate of 5 mV/sec.

## 3. Results and Discussion

### 3.1. Free potential (Open circuit potential – OCP)

When an electrically conductive material is immersed in an electrolyte, there is a potential difference E or U – at the **solution material interface** called **electrode potential**. This is not directly measurable; we only know how to measure the potential difference across an electrochemical cell formed by a complete electrochemical chain. If the electrode inserted to form the chain is well-defined and stable in time, it is a **reference** and it is then possible to compare different electrodes between them in relation to the adopted electrode reference [3]. **Analysis of the potential versus time** is useful information to track the **behavior of a material in contact with a wet corrosive environment**. Physico-chemical reactions present on the material surface change the solid-solution interface, which explains the evolution of the potential. This can be ensured by means of an acquisition device (interface millivoltmeter and micro computer) or simply by registering on a tracking board connected to the output which records an electronic millivoltmeter.

Figure 1 presents the evolution of the free potential (OCP) of mild steel since its immersion in the solution and monitored for 30 minutes, without inhibitor (blue curve) and with inhibitor (red curve).
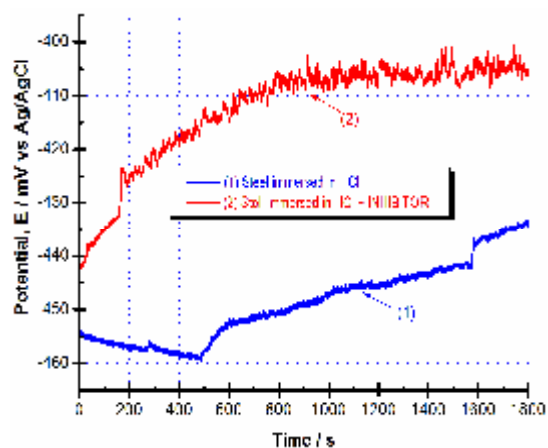


**Fig. 1.** *Open circuit evolution of steel immersed in 0.5 M HCl without and with inhibitor*

From Figure 1 it is observed that the open circuit potential of mild steel is shifted to more noble values in the presence of inhibitor. This means a more corrosion resistance of steel in HCl with inhibitor as compared to the behavior of steel immersed in HCl without inhibitor.

### 3.2. Measuring the polarization resistance (Rp) values during immersion time

Determination of polarization resistance (Rp) was performed by the method of linear polarization around the free potential with a very small potential difference (50 mV) to preserve the stady state balance of the surface relative to the solution. The results obtained after 1 hour without inhibitor and with inhibitor respectively are shown in Figure 2.
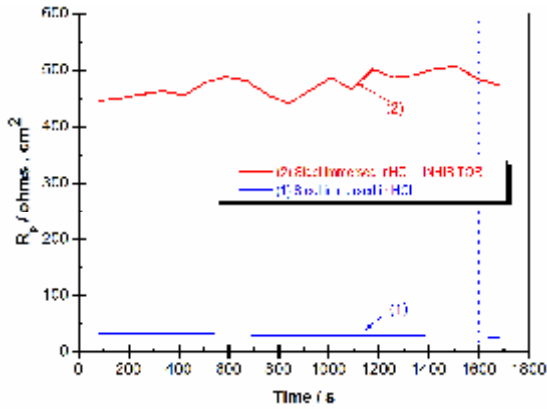
***Fig. 2.*** *Evolution of polarization resistance values of mild steel immersed in HCl solution without inhibitor and in the presence of added vegetable inhibitor*

For simple corrosion systems, the corrosion reactions are strictly controlled by the charge transfer resistance and the corrosion current density, $i_{cor}$ can be correlated with the polarization resistance $R_p$, by the relation [1], which represents the Equation Stern - Geary for the evaluation of the corrosion resistance:

$$i_{cor} = \frac{B}{R_p} \qquad (1)$$

The corrosion rate in this case is expressed in A/cm$^2$.

B is a constant specific to the material – environment system given by Equation [2]:

$$B = \frac{b_a |b_c|}{2.303(b_a + b_c)} \qquad (2)$$

Where: $b_a$ and $b_c$ are the Tafel slopes for anodic and respectively cathodic corrosion reactions. Increasing the polarization resistance means lower corrosion current density and thus lower rate of corrosion.

From Figure 2 it is observed that the polarization resistance value of steel immersed in HCl with vegetable inhibitor is about 10 times higher as compared to the value obtained for immersion in HCl without any inhibitor proving the increasing of corrosion resistance of steel 10 times compared to the behavior resulted from HCl solution without inhibitor.

Figure 3 illustrates the evolution of corrosion rate in time, corresponding to the polarization resistance in Figure 2, calculated as thickness loss.

Increasing polarization resistance in the hydrochloric acid with green inhibitor (Figure 2)

means the lowering of the corrosion current density and hence lower corrosion rate (the loss of thickness), Figure 3.
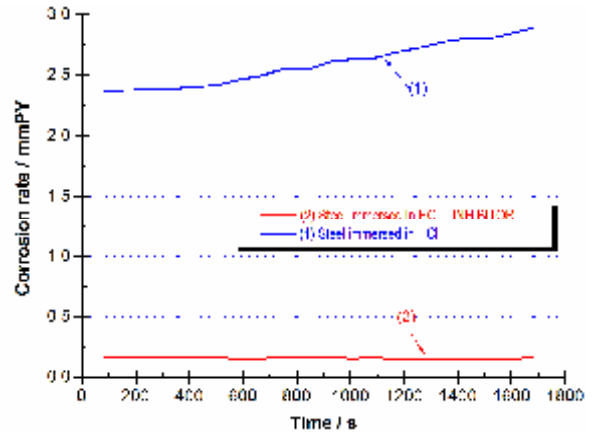


***Fig. 3.*** *Evolution of corrosion rate values of mild steel immersed in HCl solution without inhibitor and in the presence of added vegetable inhibitor*

The steel immersed in HCl solution without inhibitor shows a corrosion rate at about 10 times higher compared to the corrosion rate of steel immersed in HCl solution in the presence of vegetable inhibitor.

### 3.3. Potentiodynamic polarization curves (PD)

Diagrams i = f (E) (intensity-potential curves) drawn in a wide range of cathodic potential to anodic potential with a constant scanning sweep of 5 mV/s allow us to make some predictions on the material and the environment as it is shown in Figure 4 (a, b).
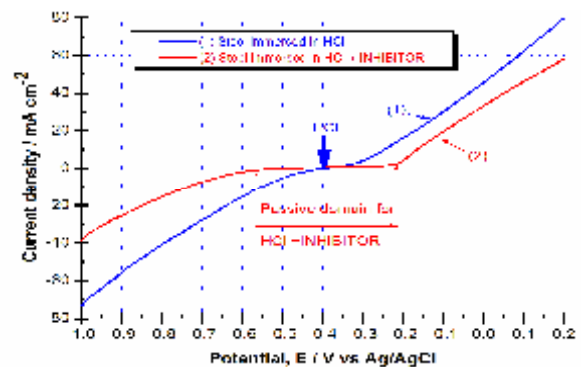


***Fig. 4 (a).*** *Potentyodynamic diagrams for mild steel in HCl solution with and without inhibitor obtained at a scan rate of 5 mV/s for the entire potential domain (-1000 mV vs Ag/AgCl to + 200 mV vs Ag/ AgCl)*

In Figure 4 three distinct potential domains are shown as follow:

► Cathodic domain: the passive film is destroyed by hydrogen reduction reaction.

► The passive domain where the passive film is formed by oxidation or adsorbtion of inhibitor. The width of this field depends always on the material studied and the corrosive environment.

► Domain of trans-passivation where the passive film is dissolved and damaged.
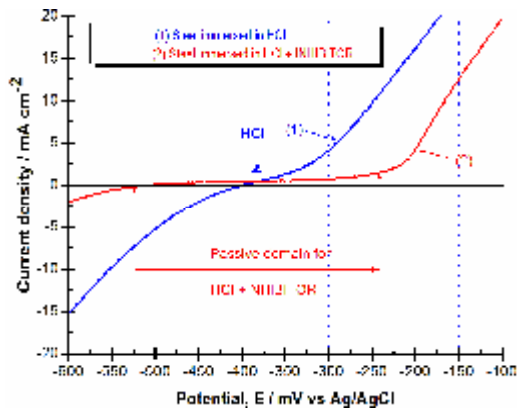


**Fig. 4 (b).** *Potentyodynamic diagrams for mild steel immersed in HCl solution with and without inhibitor obtained at a scan rate of 5 mV/s - zoom of diagrams from Fig. 4(a) in the passive domain of potentials*

The diagrams in Figure 4 show the different domains with the corresponding current densities and potentials. The status of "*cathodic*" is followed by those of "*passivity*" (stable domain) and "*transpassivity*". The potential domain for the passive state is indicated on specific diagrams with the passivation current density $i_p$. In the range of transpassivity, where the potential (E) becomes bigger than the passive potential ($E_p$), ($E > E_p$), the current density increases, since this is transpassive dissolution. In this domain the passive film loses its protective properties and even disappears at higher potentials [3].

It is illustrated from the data plotted in the diagrams in Figure 4 (a,b) that both anodic metal dissolution of iron and cathodic hydrogen evolution reaction were inhibited after the addition of green inhibitor Usinhib to 0.5 M HCl solution. The inhibition of these reactions has the effect of lowering the corrosion process.

From a practical point of view, the relative width of each potential domain and the associated values depend directly on the material/environment system. The same material, the carbon steel in this study, behaves differently in the solutions of hydrochloric acid with and without inhibitor.

In the presence of vegetable extract as inhibitor the passive domain of steel is enlarged (red curve in Figure 4). By increasing the passive domain of mild steel indicating that the adsorption of vegetable extract on mild steel surface is consistent with the mechanism of physical adsorption and therefore acting as a passive film on the steel surface.

Corrosion inhibition is caused by the stabilization of the surface film formed on steel. The effect of chemically stable surface active inhibitors increases the energy of activation of iron dissolution reaction and leads to diminution of surface available for corrosion [12].

Calculation of the Tafel slopes and the corrosion current densities (as corrosion rates) from polarization potentiodynamic curves are presented in Figure 5 (a) for mild steel immersed in hydrochloric acid without inhibitor and Figure 5 (b) for mild steel immersed in hydrochloric acid with green inhibitor.
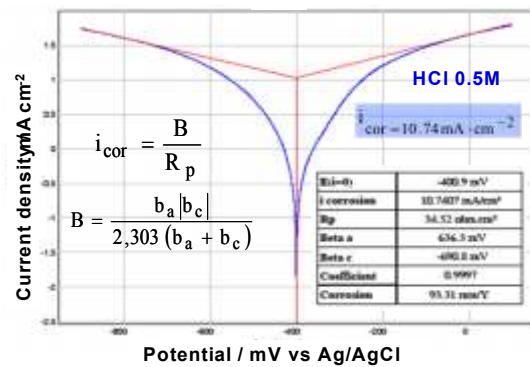


(a)
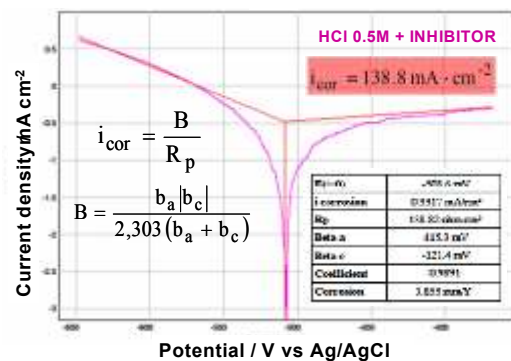


(b)

**Fig. 5.** *Application of Stern methods to evaluate the polarization resistance of carbon steel immersed in hydrochloric acid with and without green inhibitor: (a) the polarization resistance and corrosion rate of steel in HCl without vegetable inhibitor; (b) the polarization resistance and corrosion rate of steel in HCl with vegetable inhibitor*

As it is shown in Figure 5 (a, b) there is a good agreement between the values of corrosion rate and polarization resistance evaluated by the two methods like measurements of polarization resistance by linear polarization with a small amplitude around the free potential (Figures 2 and 3) and the last one by applying the Stern method and Tafel slopes.

## 3.4. Evaluation of Inhibitor's efficiency

When expressing the corrosion rate in terms of current density relative to the surface area, the efficiency of the inhibitor can be expressed as follows:

$$Inhibitor\,efficiency = \frac{(i_0 - i_i)}{i_0} x100\% \qquad (3)$$

where: $i_0$ = corrosion current density in HCl 0.5M without inhibitor; $i_i$ = corrosion current density in HCl 0.5M with inhibitor.

The result of inhibitor efficiency is about 97.2%, concluding that this vegetable extract as a green inhibitor could be utilised in the industrial applications for piclink of carbon steel in hydrocloric acid reducing in this way the material loss by dissolution during the technological process.

## 4. Conclusions

Using the green inhibitors from plant extracts as USINHIB in hydrochloric acid pickling operations of steel will have the following advantages:

- environmentally friendly, therefore pollution reduction.

- non-toxic, reducing the risk of manipulation.

- the process reduces the acid consumption by breaking the metal dissolution reaction, and also due to decreasing the process of carrying away the solution of $H_2$ gas evolved in the cathodic reaction of the corrosion process.

- it avoids the surface darkening due to the accumulation of fine particles of coal remaining after dissolution of iron in the case of carbon steel pickling.

- it prevents metal embitterment with $H_2$ of the metal being pickled, having serious consequences for its subsequent mechanical strength.

- the inhibitor reduces the rate of anodic dissolution of steel and reduces the rate of the corresponding cathodic reactions, with overall effect of slowing the corrosion process.

- by enlarging the potential domain of the passivation resulted from potentiodynamic polarization curves, it is clear that the green inhibitor USINHIB from vegetable extract is adsorbed on the steel surface to form further a protective layer.

## Acknowledgments

## References

[1]. Angela Lupu, Maria Constantinescu, Iosif Drimuş - Inhibitori de coroziune pentru protecţia metalelor, Editura tehnică, Bucureşti.

[2]. Benea Lidia - Chimie generală, Editura Academica, 2009, ISBN: 978-973-8937-45-1.

[3]. Benea Lidia - Curs anul III - Electrochimie şi coroziune.

[4]. Benea Lidia - Electrodepuneri compozite în teorie şi practică, Editura Porto- Franco Galaţi, 1998, ISBN: 973-557-490-X.

[5]. E. A. Noor - Potential of aqueous extract of Hibiscus sabdariffa leaves for inhibiting the corrosion of aluminum in alkaline solutions, Journal of Applied Electrochemistry, 39 (9), 2009, p. 1465-1475.

[6]. D. G. Ladha, U. J. Naik, N. K. Shah - Investigation of Cumin (Cuminum Cyminum) extract as an eco-friendly green corrosion inhibitor for pure Aluminium in Acid medium, Journal of Materials Environmental Science, 4 (5), 2013, p. 701-708.

[7]. E. E. Oguzie, C. K. Enenebeaku, C. O. Akalezi, S. C. Okoro, A. A. Ayuk, E. N. Ejike - Adsorption and corrosion-inhibiting effect of Dacryodis edulis extract on low-carbon-steel corrosion in acidic media, Journal of Colloid and interface Science, 349 (1), 2010, p. 238-292.

[8]. I. B. Obot, N. O. Obi-Egbedi, S. A. Umoren, E. E. Ebenso - Synergistic and antagonistic effects of anions and ipomoea invulcrata as green corrosion inhibitor for aluminium dissolution in acidic medium, International Journal of Electrochemical Science, 5(7), 2010, p. 994-1007.

[9]. A. K. Satapathy, G. Gunasekaran, S. C. Sahoo, Kumar Amit, P. V. Rodrigues - Corrosion inhibition by Justicia gendarussa plant extract in hydrochloric acid solution, Corrosion Science, 51, Issue 12, p. 2848-2856.

[10]. Olusegun K. Abiola, J. O. E. Otaigbe - The effects of Phyllanthus amarus extract on corrosion and kinetics of corrosion process of aluminum in alkaline solution, Corrosion Science, 51, Issue 11, 2009, p. 2790-2793.

[11]. Bei Qian, Baorong Hou, Meng Zheng - The inhibition effect of tannic acid on mild steel corrosion in seawater wet/dry cyclic conditions, Corrosion Science, 72, July 2013, p. 1-9.

[12]. F. Bentiss, M. Bouanis, B. Mernari, M. Traisnel, H. Vezin, M. Lagrenee - Understanding the adsorption of 4H-1,2,4-triazole derivatives on mild steel surface in molar hydrochloric acid, Applied Surface Science, 253, 2007, p. 3696.

# STRUCTURAL CHANGES ASSOCIATED WITH THE PSEUDOELASTIC RESPONSE OF Fe-BASED SHAPE MEMORY ALLOYS

**Bogdan PRICOP[1], Nicoleta Monica LOHAN[1], Firuța BORZA[2], Nicoleta LUPU[2], Marius-Gabriel SURU[1], Elena MIHALACHE[1], Radu Ioachim COMĂNECI[1], Leandru-Gheorghe BUJOREANU[1*]**

[1]Faculty of Materials Science and Engineering, "Gheorghe Asachi" Technical University of Iaşi
61A, Avenue D. Mangeron, 700050 Iaşi, Romania
[2]National Institute of Research and Development for Technical Physics,
47 Avenue Mangeron, 700050, Iaşi, Romania
* Corresponding author
e-mail: lgbujor@tuiasi.ro

## ABSTRACT

*The pseudoelastic responses of two types of iron base shape memory alloys (SMAs) were introduced and discussed. The former was based on Fe-Mn-Si system, obtained by classical (CM) and by powder metallurgy (PM) manufacturing. The latter was based on Fe-Ni-Co system being processed by a non conventional technology comprising melt spinning and heat treatment. In the case of FeMnSi-based SMAs, CM specimens obviously experienced larger ductility and a more pronounced pseudoelastic response while PM specimens were stiffer and underwent larger work-hardening. On the other hand, melt spun FeNiCo-based SMAs revealed an outstanding superelasticity in the case of micro-indentation tests. By means of scanning electron microscopy (SEM) observations, a martensitic morphology was identified in FeMnSi-based SMAs while FeNiCo-based SMAs revealed an austenitic structure. The presence of both α' and ε martensites was confirmed in FeMnSi-based SMAs by means of X-ray diffraction (XRD). In fully austenitic melt-spun and aged FeNiCo-based SMAs, no martensite was indentified on XRD patterns. These results sustain the conclusion that FeMnSi-based SMAs, that contain pre-existing martensite, experienced a pseudoelastic behavior caused by crystallographic reorientation of martensite plate variants while austenitic FeNiCo-based SMAs experienced a reversible stress-induced martensitic transformation, at room temperature.*

KEYWORDS: shape memory alloys, pseudoelasticity; tensile tests; micro-indentation; superelasticity, stress induced martensite

## 1. Introduction

Shape memory alloys (SMAs) are metallic materials exhibiting the ability to return to some previously defined shape or size when subjected to an appropriate thermal or mechanical procedure, a response that characterizes the so-called "thermal memory" or "mechanical memory" respectively [1]. These two different types of memory responses are illustrated by one way and two way effects (1-WE, 2-WE) and by superelastic behavior, respectively [2].

In general, pseudoelasticity (PE) represents any additional spring back on the elastic unloading portion of a force-displacement curve [3], while superelasticity (SE) is a particular form of PE associated with the presence of a stress plateau on the unloading portion of an isothermal stress-strain curve, caused by a reversible stress-induced martensitic transformation [4].

Iron-based SMAs have been extensively studied in the last years due to their promising results concerning mostly their thermal memory behavior and less their superelastic behavior [5]. Thus, FeMnSi-based SMAs cannot develop SE responses [6] in spite of cumbersome thermo-mechanical training processes meant to improve the shape

memory and superelastic properties [7]. Partial PE was observed in FeMnSi-based SMAs, being associated with incomplete γ (face centre cubic, fcc) → ε (hexagonal close-packed, hcp) stress-induced martensitic transformation (MT) that was slightly enhanced by pre-strain increase up to 8% [8]. The PE response of the FeMnSi-based SMAs is incomplete, since the deformation above reverse martensitic transformation temperatures induces slip deformation due to the large temperature hysteresis [9].

On the other hand, in FeNiCo-based SMAs the precipitation of the disperse $(CoNi)_3Ti$ particles with $L1_2$-type atomic-ordered structure results in a change of the kinetics of γ (fcc)−α′ (body centre cubic, bcc) MT from a non-thermoelastic kinetics with large temperature hysteresis H = 400 K to a γ (fcc)−α′ (body centre tetragonal, bct) thermoelastic one with the hysteresis H ~ 30–100 K in the heterophase state [10]. $(CoNi)_3Ti$ particles, designated as γ' precipitates, do not undergo martensitic transformation, but in turn they favor the accumulation of the elastic energy in martensite crystals, thus causing a back stress which enhances martensite reversion to parent phase (austenite) [11]. Concerning FeNiCo-based SMAs a remarkable result was recently reported by Tanaka *et al.* who developed a polycrystalline FeNiCoAlTaB alloy characterized by a superelastic response that was never observed in polycrystalline SMAs [12]. Due to the superelastic strain of more than 13%, presented by Tanaka *et al.* correlated with a tensile strength above 1 GPa, the SE response obtained in highly textured FeNiCo-based SMAs authorized the term "huge superelasticity" to be used for the first time in association with SMAs [13]. The present paper aims to compare the pseudoelastic responses of a FeMnSi-based and a FeNiCo-based SMA, obtained by different manufacturing technologies, and to corroborate these responses with the structures of the respective alloys.

## 2. Experimental procedure

An Fe-18Mn-3Si-7Cr-4Ni (mass. %) SMA was produced by classical metallurgy (CM) and by powder metallurgy (PM), using high frequency induction melting, pressing and sintering at 1390 K. Mechanical alloying (MA) was applied in order to attained compositional homogenization of FeMnSi-based SMAs [14] and for this purpose a ball to powder ratio (BPR) of 1/8 and a 2 mass. % fraction of Stearic Acid (SA) were used [15]. After homogenization annealing, (1370 K/ 1 hr. /water) specimens' thickness was reduced to about $1 \times 10^{-3}$ m by hot rolling, at 1270 K. Both CM and PM specimens, cut to $1 \times 5 \times 40 \times 10^{-3}$ m, were subjected to tensile loading-unloading tests on an INSTRON

3382 tensile testing machine with a deformation rate of $2.77 \times 10^{-4} sec^{-1}$.

After embedding into cold mounting resin and metallographic preparation, SEM analysis was conducted on a SEM - VEGA II LSH TESCAN scanning electron microscope (SEM), coupled with an EDX - QUANTAX QX2 ROENTEC detector. X-ray diffraction (XRD) patterns were recorded on a BRUKER AXS D8 Advance diffractometer with Cu $K_\alpha$ [16].

$Fe_{40.95}Ni_{28}Co_{17}Al_{11.5}Ta_{2.5}B_{0.05}$ ribbons, with cross-section of $43 \times 70 \times 10^{-6}$ m, were prepared by melt spinning and were aged for 2× 3.6 ks at 923 K. Micro-indentation tests were performed with a sharp indenter, on a UMT-CETR universal tester at a maximum load of 15 N. Load-depth indentation curves were recorded, at a position precision of $1 \times 10^{-7}$m, by means of the CETR data viewing software.

Embedded ribbons were observed by means of a JEOL JSM 6390 SEM microscope and analyzed on a D8 Advance - Bruker AxS GmbH diffractometer with Cu-$K_\alpha$ radiation, radiation intensity $I_e$=40mA and Voltage= 40KV [17].

## 3. Results and discussion

Two stress-strain curves obtained during two successive loading-unloading tensile tests of CM Fe-18Mn-3Si-7Cr-4Ni SMA specimens are illustrated in Fig. 1.
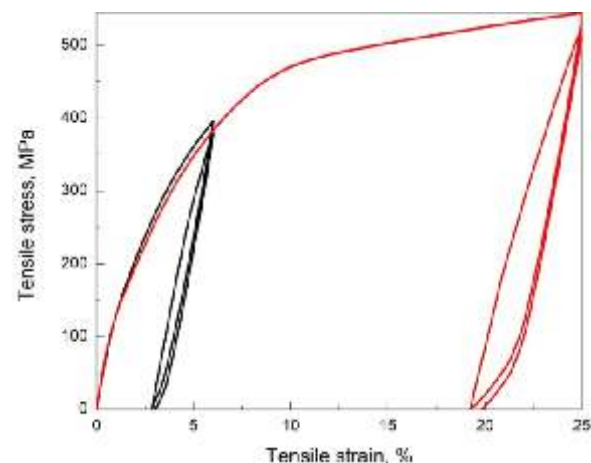


***Fig. 1.*** *Stress-strain curves, recorded on two specimens of Fe-18Mn-3Si-7Cr-4Ni (mass. %) SMA processed by classical metallurgy. Two loading-unloading tensile tests were performed up to 5% and to 25% total strains, respectively, in order to illustrate the augmentation tendency of PE response with the increase of total strain*

The loading portions reveal rounded plastic regions, characteristic for transformation induced plasticity (TRIP) [18], which are visible only during first loading. This change suggests that stress induced martensitic transformation is the governing deformation mechanism only during first loading while slip becomes prominent during subsequent loadings. On the other hand, in both cases unloading has been accompanied by a PE response. Considering the values of pseudoelastic strain ($\varepsilon_{pe}$) as the difference between unloading recovery strain ($\varepsilon_{rec}$) and elastic strain ($\varepsilon_e$) [8], it follows that for 5% the total strain is $\varepsilon_{pe}$ = 2.8 - 2.4 = 0.4% while for 25% total strain is $\varepsilon_{pe}$ = 5.2 - 3.7 = 1.5%, which suggests that PE response tends to increase with total strain.

In the case of PM Fe-18Mn-3Si-7Cr-4Ni SMA, total strain could not exceed 4%. However, TRIP-characteristic deformation behavior during first loading has also been noticeable in the case of PM specimens, as shown in the representative tensile stress-strain curves illustrated in Fig. 2.
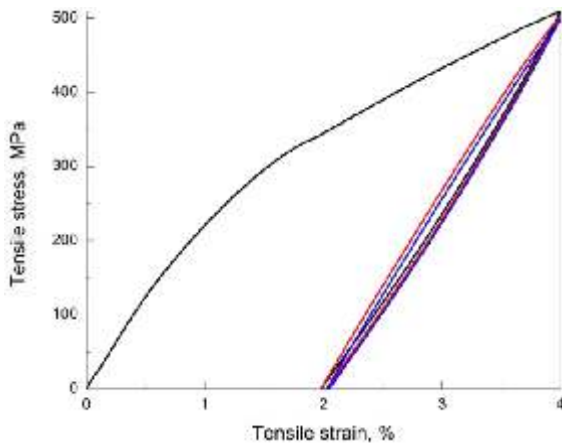


*Fig. 2. Stress-strain curves, recorded on a specimen of Fe-18Mn-3Si-7Cr-4Ni (mass. %) SMA processed by powder metallurgy with mechanical alloying. Three loading-unloading tensile tests were performed up to 4% total strain which illustrate a slight diminution tendency of PE response with the increase of the number of cycles*

As compared to CM specimens, PM specimens revealed less marked TRIP behavior and less PE response, yet higher strength and stiffness. With increasing the number of cycles, pseudoelastic strain decreased from 0.37% in the first cycle, to 0.34% in the second and to 0.33% in the third, in good agreement with the general decreasing tendency with increasing the number of loading-unloading cycles, previously reported in the variation of strain recovery degree of PM FeMnSi-based SMAs [19].

These hardening effects could be caused by mechanical alloying (MA) which, in the case of low-Mn Fe-based alloys, enhances deformation hardening due to the formation of brittle α' martensite [20]. In addition, since TRIP effect is mainly caused by stress-induced formation of ε –hcp martensite [21], it is expectable that PM FeMnSi-based specimen contains less amount of this phase.

A different insight into the PE and SE responses of the FeMnSi-based and FeNiCo-based alloys under study is given by micro-indentation tests. Figure 3 illustrates the micro-indentation curve of CM FeMnSi-based SMA.
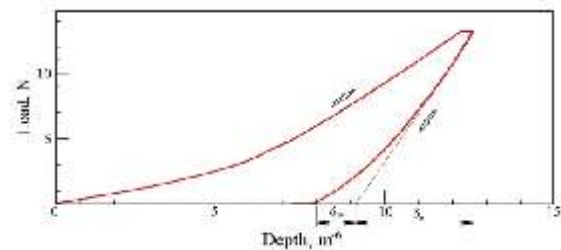


*Fig. 3. Micro-indentation curve of Fe-18Mn-3Si-7Cr-4Ni (mass. %) SMA processed by classical metallurgy illustrating a PE response characterized by 38.1% recoverable penetration depth and 10.3% pseudoelastic penetration depth*

In contrast to spherical-indenter tests [22], the micro-indentation curve from Fig. 3 reveals a notable PE response. Considering that reversible stress-induced phase transition mechanisms require the presence, on the unloading stage of indentation curves, either of load plateaus or of "pop-out events" [23], it is obvious, from Fig. 3, that none of these events is noticeable. Therefore, during indentation tests, in good agreement with tensile stress-strain curves shown in Fig. 1, it can be considered that stress-induced formation of martensite is irreversible in CM FeMnSi-based SMA under study. The change of the slope in Fig. 3 suggests a change in the deformation mode, form stress-induced formation of martensite in the lower part, to dislocation slip, corresponding to the upper part of indentation curve, according to similar results obtained at FeMnSi-based SMAs [24]. By determining the values of recovery depth and elastic depth as $\delta_{rec}$ = 4.8 × $10^{-6}$ m and $\delta_e$ = 3.5 × $10^{-6}$ m, respectively it follows that pseudoelastic penetration depth has the value $\delta_{pe}$ = $\delta_{rec}$ - $\delta_e$ = 1.3 × $10^{-6}$ m. The PE response of CM FeMnSi-based SMA can be expressed, as percentages of total penetration depth of 12.6 × $10^{-6}$ m.

Thus, recoverable depth ($\delta_{rec}$) represents 38.1% and pseudoelastic depth ($\delta_{pe}$) only 10.3%.

A different micro-indentation curve was recorded in the case of melt spun and aged FeNiCo-based SMA ribbons, as shown in Fig. 4.

The load plateau noticeable on the unloading portion of micro-indentation curve upholds the reversible character of stress-induced martensitic transformation, characteristic to superelastic behavior in two-phase region, of FeNiCo-based SMAs [25]. In this case, considering total indentation depth as $19.7 \times 10^{-6}$ m and permanent indentation depth $8.6 \times 10^{-6}$ m, it follows that recovery indentation depth is $\delta_{rec} = 11.1 \times 10^{-6}$ m. In this case elastic indentation depth is $\delta_e = 2.3 \times 10^{-6}$ m and pseudoelastic indentation depth becomes $\delta_{pe} = 8.8 \times 10^{-6}$ m. As compared to total indentation depth, recovery depth represents $11.1/19.7 \times 100 = 56.3\%$ while pseudoelastic depth is $8.8/19.7 \times 100 = 44.6\%$. These values justify the use of SE response instead of PE response in relation to FeNiCo-based SMAs.
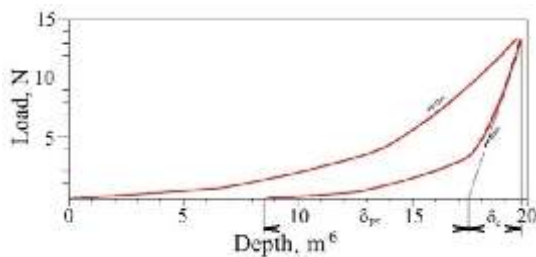


**Fig. 4.** *Micro-indentation curve of melt spun $Fe_{40.95}Ni_{28}Co_{17}Al_{11.5}Ta_{2.5}B_{0.05}$ aged for $2 \times 3.6$ ks at 923 K illustrating a SE response characterized by 56.3% recoverable penetration depth and 44.6% pseudoelastic penetration depth*

From the structural point of view, CM FeMnSi-based SMAs reveal martensite plates in an austenite matrix, as illustrated in Fig. 5, by means of representative SEM micrograph.

The triangle morphology, typical to ε - hcp martensite [26], is hardly noticeable on the micrograph shown in Fig. 5, thus suggesting that most of martensite plates would belong to α'-bct martensite, which is common presence in low-manganese FeMnSi-based SMAs [27].

A typical SEM micrograph of the surface of melt spun and aged FeNiCo-based SMA ribbons is presented in Fig.6.

The micrograph shows a fully austenitic structure [25] with an average grain size of approximately 10 micrometers [17]. Some of austenite grains contain parallel bands which can be identified as twins. White-color dispersed particles, with an average size estimated to 90 nanometers, were identified by energy dispersive X-ray (EDX) measurements as Ta.

The total absence of martensite plates, which are indispensable for a FeNiCo-based SMA alloy to exhibit shape memory effect (SME), supports the assumption that α'-bct martensite cannot be stabilized at room temperature [28]. In good accordance with the SE response observed in Fig. 5, it can be assumed that α'-bct stress-induced martensite formed from austenite during loading and, being unstable, reverted to austenite during unloading [29].
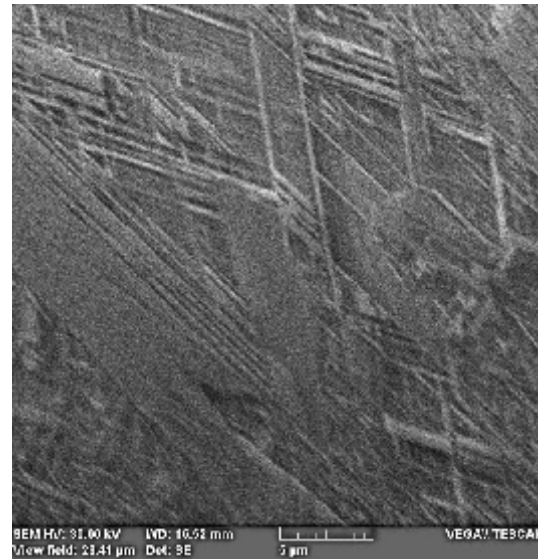


**Fig. 5.** *Typical SEM micrograph of Fe-18Mn-3Si-7Cr-4Ni (mass. %) SMA processed by classical metallurgy revealing multivariant martensite plates in a matrix of retained austenite*
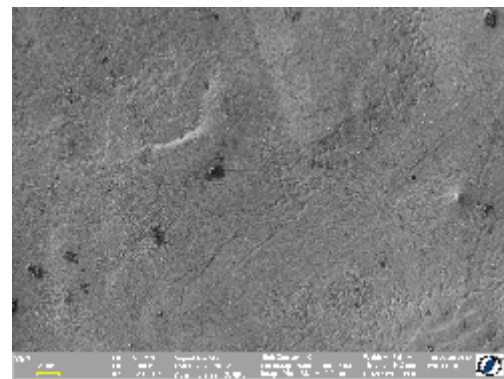


**Fig. 6.** *Typical SEM micrograph of melt spun $Fe_{40.95}Ni_{28}Co_{17}Al_{11.5}Ta_{2.5}B_{0.05}$ aged for $2 \times 3.6$ ks at 923 K revealing fully austenitic structure with twins*

A proper identification of phase structure of the two alloys under study was performed by XRD. The first representative XRD patterns for FeMnSi-based SMAs under study are shown in Fig. 7.

It is obvious that the amount of ε - hcp martensite is very low since, in PM specimen, the main diffraction maximum $(10\bar{1}1)$ is absent and the only basal plane, (0002), is present with a very low intensity. This coexistence of the two types of martensite can be a consequence of the complex thermal phenomena prone to occur in powder mixtures of mechanically alloyed particles, such as magnetic transition of Ni, glass-transition of amorphous regions and surface oxidation, only α'-bct is noticeable [30]. Normally, the amount of ε - hcp martensite should markedly increase after a tensile loading-unloading cycle [31]. In initial state, the structure of PM FeMnSi-based SMA specimen contains an approximate amount of 10.5% ε - hcp martensite. Conversely, the amount of α'-bct martensite can be estimated around 17.4% in PM specimen and 15.2% in CM specimen. The larger amount of martensite, pre-existing in PM specimen can be the cause of its higher stiffness.
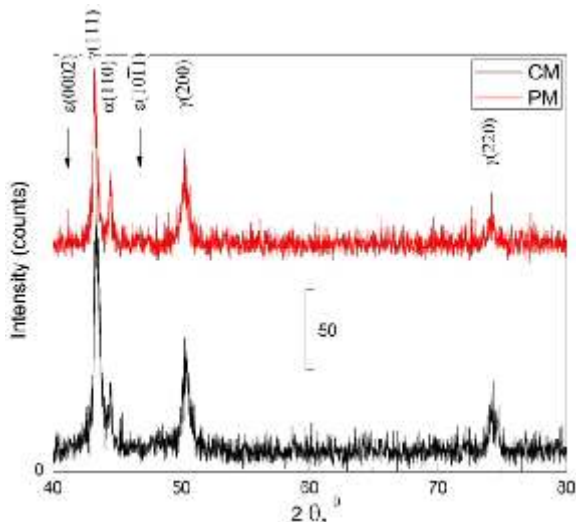


**Fig. 7.** *Representative XRD patterns for Fe-18Mn-3Si-7Cr-4Ni (mass. %) SMA processed by classical metallurgy (CM) and by powder metallurgy (PM)*

As expected, the structure of melt spun and aged FeNiCo-based ribbons are fully austenitic with γ' precipitates, as resulting from the XRD - pattern shown in Fig. 8.

The inset gives a detail of the diffraction peak of γ'-phase, meant to harden austenitic matrix in such a way as to give martensitic transformation a thermoelastic character [32]. The amount of γ'-phase was estimated to approx. 11.7% but, due to its nanometric size [7, 13, 29], the precipitates cannot be observed by SEM [33].
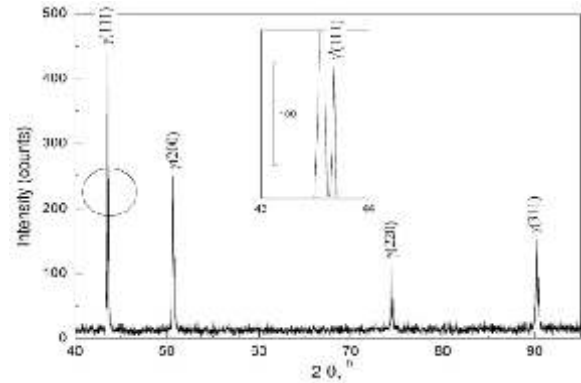


**Fig. 8.** *Representative XRD patterns for melt spun $Fe_{40.95}Ni_{28}Co_{17}Al_{11.5}Ta_{2.5}B_{0.05}$ aged for 2 × 3.6 ks at 923 K with inset detail of γ' diffraction peak*

## 4. Conclusions

The differences in the pseudoelastic behavior of two Fe-based SMAs were associated with:

- the pre-existence of martensite in a classical metallurgy processed FeMnSi-based specimen which experienced a pseudoelastic response of 1.5% in tension and of 10.3% at micro-indentation tests;

- the reversible stress-induced formation of martensite in melt spun and aged ribbons of FeNiCo-based SMA which experienced a superelastic response of 44.6% at micro-indentation tests.

## Acknowledgement

## References

[1]. **Hodgson D. E., Ming H. W., Biermann R. J. -** *Properties and Selection: Nonferrous Alloys and Special-Purpose Materials*, ASM Handbook, Vol. 2, (ASM International), 1990, p. 897-902.
[2]. **Sun L., Huang W. M., Ding Z., Zhao Y., Wang C. C., Purnawali H., Tang C. -** Mater Design, 33 (2012), p. 577-640.
[3]. **Duerig T. W., Zadno R.,** *Engineering Aspects of Shape Memory Alloys*, edited by Duerig T W, Melton K N, Stöckel D, Wayman C M, (Butterworth-Heinemann) 1990, p. 369-393.
[4]. **Wasilewski R. J. -** *Shape Memory Effects in Alloys*, edited by Perkins J, (Plenum Press, New York-London), 1975, p. 245-271.
[5]. **Dunne D. -** *Phase transformations in steels: Diffusionless transformations, high strength steels, modelling and advanced analytical techniques*, Vol. 2, edited by Pereloma E & Edmonds D V, (Woodhead Publishing), 2012, p. 83-125.
[6]. **Xiao-Xiang Wang, Chu-Yang Zhang -** *J Mater Sci Letters*, 17 (1998), p. 1795-1796.
[7]. **Ma J., Kockar B., Evirgen A., Karaman I., Luo Z. P., Chumlyakov Y. I. -** *Acta Mater,* 60, 2012, p. 2186-2195.

**[8]. Zhao C. -** *J Mater Sci Letters,* 19, 2000, p. 1711 – 1713.
**[9]. Sawaguchi T., Kikuchi T., Kajiwara S. -** *Smart Mater Struct,* 14, 2005, p. S317-S322.
**[10]. Chumlyakov Y. I., Kireeva I. V., Panchenko E. Y., Aksenov V. B., Kirillov V. A., Ovsyannikov A. V., Zakharova E. G., Sehitoglu H. -** *Russ Phys J.*, 46 (8), 2003, p. 811-823.
**[11]. Chumlyakov Y. I., Kireeva I. V., E. Panchenko Y., Zakharova E. G., Kirillov V. A., Efimenko S. P., Sehitoglu H. -** *Dokl Phys*, 49 (1), 2004, p. 47-50.
**[12]. Ma J., Karaman I. -** *Science*, 327, 2010, p. 1468-1469.
**[13]. Tanaka Y., Himuro Y., Kainuma R., Sutou Y., Omori T., Ishida K. -** *Science*, 327, 2010, p. 1488-1490.
**[14]. Söyler A. U., Özkal B., Bujoreanu L. G. -** *Sintering Densification and Microstructural Characterization of Mechanical Alloyed Fe-Mn-Si based Powder Metal System*, Supp. Proc.TMS, 3, 2010, p. 785-792.
**[15]. Söyler A. U., Özkal B., Bujoreanu L. G. -** *Investigation of Mechanical Alloying Process Parameters on Fe-Mn-Si Based System*, Supp. Proc. TMS, 1, 2010, p. 577-583.
**[16]. Bujoreanu L. G., Stanciu S., Ozkal B., Comaneci R. I., Meyer M. -** ESOMAT 2009, 05003, 2009.
**[17]. Paraschiv A. L., Suru M. G., Lohan N. M., Pricop B., Bujoreanu L. G., Borza F., Lupu N. -** *Factors influencing the structure and proprieties of polycrystalline magnetic Fe-Ni-Co-Al-Ta-B shape memory alloy*, Proceedings of the International Conference on Shape Memory and Superelastic Technologies May 20–24, 2013, Prague, Czech Republic, p. 27-28.
**[18]. Gu N., Lin C., Song X., Peng H., Yin F., Liu Q. -** *Mater Sci Forum*, 327-328, 2000, p. 231-234.
**[19]. Pricop B., Söyler U., Comăneci R. I., Özkal B., Bujoreanu L. G. -** *Phys Proced*, 10, 2010, p. 125-131.

**[20]. Cherdyntsev V. V., Pustov L. Y., Kaloshkin S. D., Tomilin I. A., Shelekhov E. V., Laptev A. I., Baldokhin Y. V., Estrin E. I. -** *Phys Met Metallogr*, 104(4), 2007, p. 408-414.
**[21]. Guo Y.-M., Wang G.-X., Feng J.-H., Chen C.-X., Peng H.-F. -** *J Iron Steel Res Int*, 23(9), 2011, p. 50-54.
**[22]. Wenyi Yan, Qingping Sun, Xi-Qiao Feng, Linmao Qian -** *Int J Solids Struct,* 44, 2007, p. 1-17.
**[23]. Maletta C., Furgiuele F., Sgambitterra E., Callisti M., Mellor B. G., Wood R. J. K. -** *Frattura ed Integrità Strutturale*, 21 2012, p. 5-12.
**[24]. Sekido K., Ohmura T., Sawaguchi T., Koyama M., Park H. W., Tsuzaki K. -** *Scripta Mater,* 65, 2011, p. 942-945.
**[25]. Titenko A. N., Demchenko L. D. -** *J Mater Eng Perform*, 21, 2012, p. 2525-2529.
**[26]. Sawaguchi T., Bujoreanu L.-G., Kikuchi T., Ogawa K., Yin F. -** *ISIJ Inter*, 48(1), 2008, p. 99-106.
**[27]. B. Pricop, U. Söyler, B. Özkal, N. M. Lohan, A. L. Paraschiv, M. G. Suru, L. G. Bujoreanu -** *Mater Sci Forum*, 738-739, 2013, p. 237-241.
**[28]. Sagaradze V. V., Kabanova I. G., Kataeva N. V., Klyukina M. F. -** *Mater Sci Forum*, 738-739, 2013, p. 200-205.
**[29]. Yonghong Geng, Mingjiang Jin, Wenjing Ren, Weimin Zhang, Xuejun Jin -** *J Alloy Compd*, 2012, doi:10.1016/j.jallcom.2012.03.033.
**[30]. Pricop B., Söyler U., Lohan N. M., Özkal B., Chicet D., David A., Bujoreanu L. G. -** *Optoelectron Adv Mat*, 5(5), 2011, p. 555-561.
**[31]. Bouraoui T., Jemal F., Ben Zineb T. -** *Strength Mater*, 40(2), 2008, p. 203-211.
**[32]. Hayashi R., Murray S. J., Marioni M., Allen S. M. O'Handley R. C. -** *Sensors Actuat A*, 81, 2000, p. 219–223.

# RESEARCH REGARDING THE WEAR LEVEL FOR A NEW CONSTRUCTIVE SOLUTION OF A CUTTING TOOL

**Liliana Georgeta POPESCU**

"Lucian Blaga" University of Sibiu, 10, Victoriei Boulevard, Sibiu, Romania
e-mail: liliana.popescu@ulbsibiu.ro

## ABSTRACT

*The paper presents a study of wear made to implement a constructive solution for a new cutting tool. The design of the cutting tool can be checked from a functional perspective, as well as reliability during the cutting process (process simulation). The purpose of the cutting process simulation is to check the new solution using the finite element analysis method. The criterion to assess the effectiveness of the constructive solution is the study of the tool wear level depending on cutting regime parameters. The implementation of the wear model in the DEFORM software was used to establish the wear level.*

KEYWORDS: cutting tool, simulation, DEFORM Machining software

## 1. Introduction

The research literature revealed that Deform 2D software is effective in both research and industrial applications.

Machining 2D software developed by Scientific Deform Forming Technologies Corporation, Columbus, Ohio has, in addition to the previous embodiments, the predictive model on the basis of the cutting tool wear analytical model of Usui.

$$\frac{dw}{dt} = C_1 \cdot \sigma \cdot v_s \cdot e^{\left(\frac{-C_2}{T}\right)} \qquad (1)$$

where: $\frac{dw}{dt}$ – wear intensity

$C_1$, $C_2$ - coefficients that depend on the workpiece and tool material;

$v_s$ - the flow rate of the cut, [m/min];

$T$ - cutting temperature;

$\sigma$ - normal pressure (specific pressing).

Machining Software Deform shapes and simulates the cutting process using orthogonal cutting assumptions.

## 2. Simulation of the chamfer process

The purpose of the chamfering process simulation is to check the proposed solution design with the terms of finite element analysis. The assessing criteria for the effectiveness of the solution is the wear of the constructive tool depending on cutting regime parameters: cutting speed, feed and cut depth. The possibility of the wear calculation is given by the implementation of the wearing model in the Deform software.
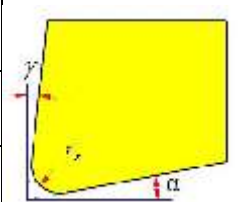
In the simulation of the chamfer process it has been used metal carbide, type P30, coated with a layer of 5 micron titanium carbonitride (TiCN), with the rake angle γ = 10, the clearance angle α = 8, the attack angle κ = 45. As processed material was used OLC 45 improved steel.

Usui's model coefficients for equivalent material OLC 45 (ANSI 1045) for the boring operation have the values: a = 0.0000002; b = 650.5.

From the finite element calculation point of view, the tool is considered rigid because the program does not calculate the deformations and tensions inside the tool, but only the specific temperature and pressing.

For the workpiece it is chosen the elastic-plastic environment. Cutting conditions (chosen as intensive) shown in Table 1 and the working conditions are introduced in the pre-processor of the program. Here are defined all the initial conditions. The process is finalised with the positioning of the tool and of the workpiece as is shown in Figure 1.

***Table 1.*** *The simulation process parameters*

| No. | Tool geometry | | feeding, [mm/rot] | Cutting depth, [mm] | Cutting speed, [m/min] |
|---|---|---|---|---|---|
| 1. |  | $\alpha = 6^0$ $\gamma = 6^0$ $r_\varepsilon = 0.05$ | 0.03 | 1.0 | 75 |
| 2. | | | | | 100 |
| 3. | | | | | 200 |



***Fig. 1.*** *The initial position of the simulation*
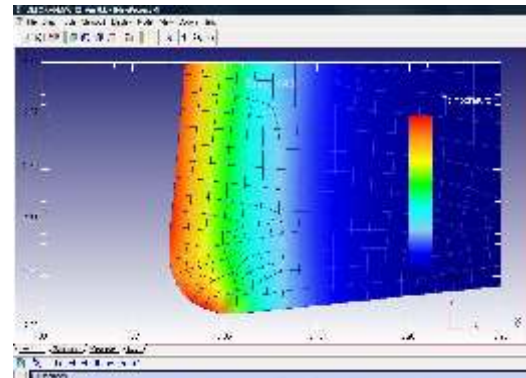


***Fig. 3.*** *Temperature map inside the piece and cutting tool*

Note that, for each combination shown in Table 1 the meshing of the tool and of the workpiece was done.

After running the finite element program for chamfering operation (bore processing), the output of the procces is represented by the following sets of parameters values, that are included in the graphs in Figures 2 and 3). The temperature field in the cutting area and in the cutting tool are shown in Figure 2.
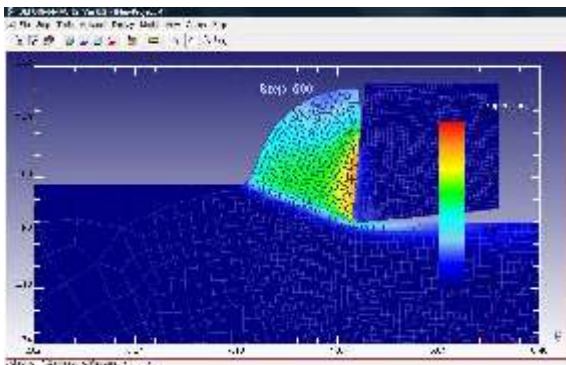


***Fig. 2.*** *Map temperature into the piece and cutting tool*

The isotherms of the thermal field in the cutting tool and the workpiece, by means of which it is possible to predict the wear of the tool, are shown in Figure 4 a and b.
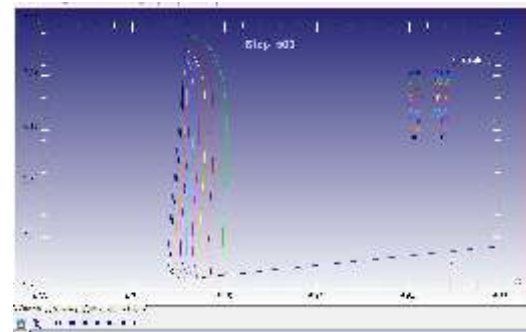


*a.*
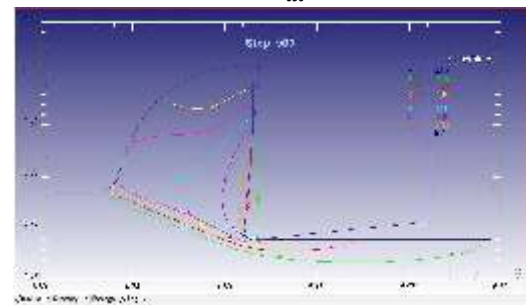


*b.*

***Fig. 4.*** *Isotherms of the thermal field*

The chart of Loading splinter elements in [N] (X axis) is shown in Figure 5, and Figure 6 shows the plane stress state in the workpiece and chip highlighting actual voltage, $\overline{\sigma}$ [N/mm$^2$].
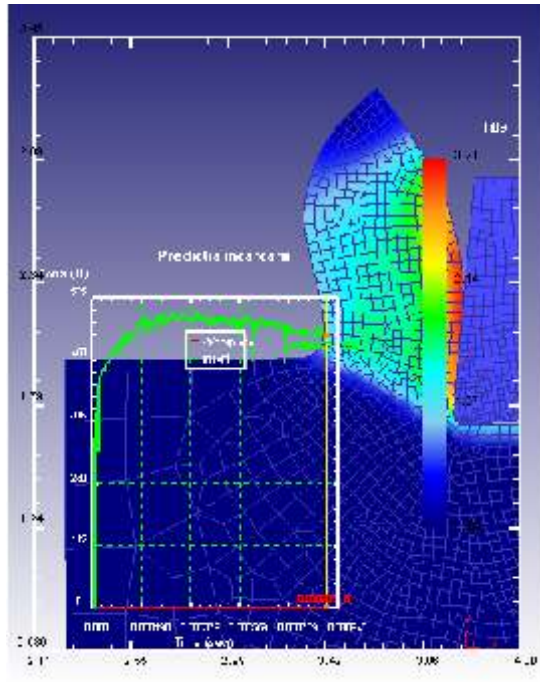
***Fig. 5.*** *Prediction loading in the workpiece and in the tool*
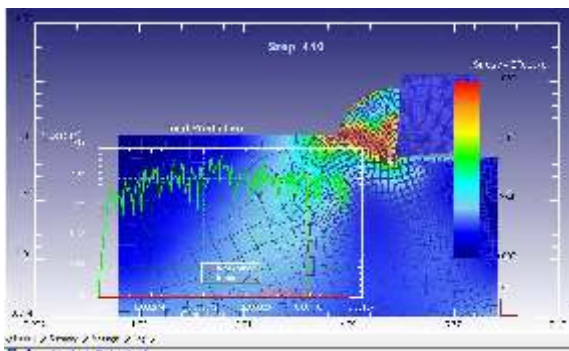


***Fig. 6.*** *Plane stress condition,* $\overline{\sigma}$
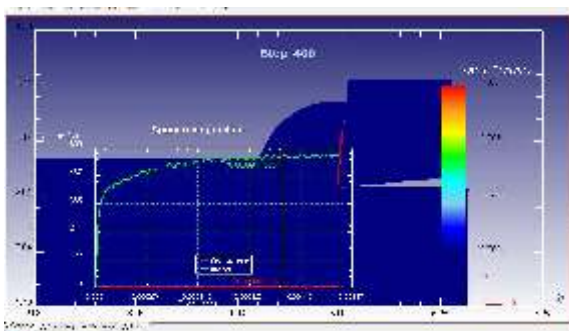


***Fig. 7.*** *The specific pressing on the clearance face*

The specific pressing on the direction X and P, [N/mm$^2$] is shown in Figure 7.

## 3. Interpretation of results

The variables states provided by the simulation of cutting software are very useful in establishing a model based on the mechanical wear of specific cutting. Also, the cutting forces can be calculated on the X, Y direction, highlighting indirectly the state of wear of the cutting tool.

From the temperature state, we can see that the position of the center of wear on the rake face is located at a certain distance from the cutting edge of the tool, which coincides with the maximum depth of crater wear. Isotherms representation are highlighting exactly the shape of the crater wear on the rake face and the wear of the settlement surface. Temperature values will be used in the calculation of the tool wear, based on Usui model.

The database generated by simulating the cutting process can be transferred to the analysis of the tool state of stress and strain, using another finite element program (ANSYS). For this analysis, the initial load status parameters on contour (Boundary Condition) are already stored in the database.

In-depth analysis of the program simulation results and other elements of the cutting process can be identified, which are not directly related to the phenomenon of wear, such as:

Figure 4 presents the maximum stress state of contact between tool and chip to an intermediate position tool (Step 500), as the chip shear zone is very distinctly evidenced.

Also, in this Figure, there is an uneven stress distribution on the contact surface between the tool and the part (the effective sectional area of the chip).

The size of the area affected by the tension in the piece can be observed. The tool wear can be estimated for the same cutting conditions. The estimation of tool wear is brought to an end after three cycles of tool wear calculations.

Machining Deform 2D program is controling the chip formation, and the analysis of heat transfer is watching the analysis process, and the result is then stored in a database. These values are required to estimate the tool wear.

Estimation of tool wear can be simplified assuming that the wear is only created by the cutting process steady state and neglecting the effect of entry or exit phase.

Integrating the mathematical model of tool wear with finite element analysis of steady-state cutting tool wear, the estimation of the tool wear can be implemented.

This will be done using a computer program to calculate the tool wear.

### 3.1. Calculation algorithm of the tool wear at chamfering

To calculate the tool wear in the boring process it was created in Matlab program the program called "The tool wear after simulation. m". The program is designed to perform the calculation of tool wear based on the results of finite element simulations. Thus, after a certain number of steps (Step increments to save = 10) of the simulation data are taken calculated data on the specific pressing, temperature and flow rate of the chip.

After each calculation cycle, the data on chip formation and heat transfer are exported as Matlab files matrices, in order to obtain the input values of variables needed to calculate the wear. The values of these measurements are then processed by the Usui's analytical wear model (equation 1). The procedure for estimating the wear of the tool is shown in Figure 8.

Since the full simulation time is much less than the real operation time of the tool till the admissible wear level is reached, by this computer program can be extended the life of the tool to a value close to the actual values. For this, is considered the assumption of achieving the steady state from the "finite element", after which, both temperature and specific pressing are considered relatively constant.
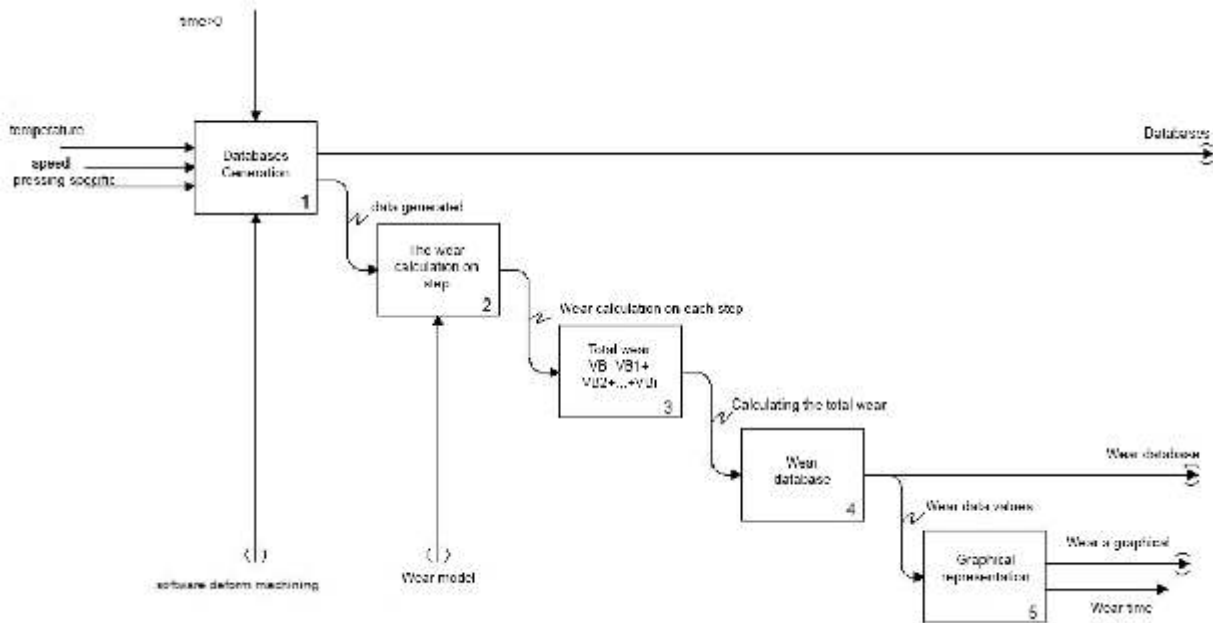


*Fig. 8.* *The steps for calculating the tool wear*
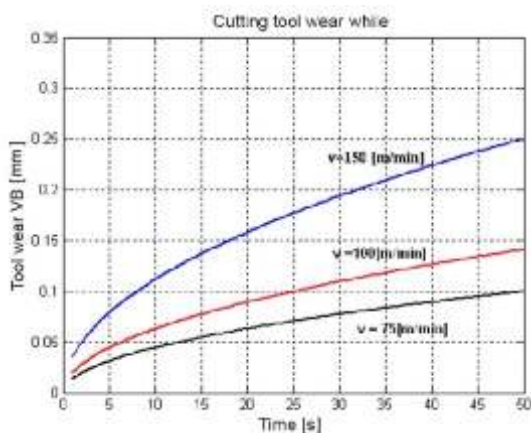


*Fig. 9.* *Tool wear in time based on simulations from the Deform Software*

This way, by extrapolating the calculation of the wear we are close to reality, considering that we stand on the level of normal wear.

For the wear calculation and for plotting the wear curve of Figure 9, were used the results from the three simulations shown in Table 1.

After the running of the program and considering the time, which now has the real value, the theoretical wear curves were plotted as shown in Figure 9.

## 4. Conclusions

The results of finite element simulation show that the chosen solution is feasible and the resulting values are within normal limits.

In terms of cutting tool wear estimation, it is shown in Figure 9 that the proposed solution has a high sensitivity to the changes of the cutting speed (it is normal considering that the tip of the cutting tool has a low volume of material).

## Acknowledgments

## References

[1]. **Popescu L. G. -** *Contributions on the efficiency research activity in industry*, Phd Thesis, "Lucian Blaga" University, Sibiu, 2010.
[2]. **Usui E., Shirakashi S., Kitagawa T. -** *Analitical Prediction of Tool Wear*, in Wear, 1984, 100, p. 129-151.
[3]. **\*\*\* -** www.deform.com/products/deform-2d/

# ANTIMICROBIAL ACTIVITY OF Ag:ZnO/CHITOSAN COMPOSITES

**Mariana (BUȘILĂ) IBĂNESCU[1]\*, Dana TUTUNARU[2], Viorica MUȘAT[1]**

[1]"Dunărea de Jos" University of Galați, Centre of Nanostructures and Functional Materials-CNMF,
111 Domnească Street, 800008, Galați, Romania
[2]"Dunărea de Jos" University of Galați, Faculty of Medicine and Pharmacy,
111 Domnească Street, 800008, Galați, Romania
\*Corresponding author
e-mail: mariana.ibanescu@ugal.ro

## ABSTRACT

*This paper deals with Ag, ZnO and Ag-doped ZnO nanoparticles embedded in chitosan (CS) matrix, prepared by hydrolysis of zinc acetate in isopropanol in the presence of lithium hydroxide (LiOH) in low temperature conditions.*

*The nanoparticles embedded in the chitosan matrix were characterised by X-ray diffraction (XRD) and scanning electron microscopy (SEM).*

*The antimicrobial activity of Ag/CS, ZnO/CS and Ag:ZnO/CS composites with respect to simple CS polymer was investigated by using the paper disc method on Mueller-Hinton agar without blood against the Gram-negative bacteria, Escherichia coli (E. coli) and the Gram-positive bacteria, Staphylococcus aureus (S. Aureus) on Mueller-Hinton agar with blood. The nanocomposites materials showed good antimicrobial activity, that recommends them for applications in medical and food packaging fields.*

KEYWORDS: chitosan, ZnO nanoparticles, antimicrobial activity

## 1. Introduction

Polymer nanocomposites containing semiconductive zinc oxide nanoparticles have attracted a great interest due to their unique chemical and physical properties. The need of elaboration of non-toxic and cost-effective antimicrobial finishing of fabrics grows with progressive production increase of medical, healthcare and protective materials [1]. Embedding of semiconductor nanoparticles in polymeric matrices provide a way for a better exploitation of their optical properties, catalytic and antimocrobiene characteristic. On the other hand, the host polymer may influence the growth and spatial arrangement of the nanoparticles in situ during the synthesis, making them suitable for the preparation of nano patterns with different morphologies [2].

Furthermore, by selecting the polymer with certain favorable properties such as biocompatibility [3], conductivity [4] or photoluminescence [5], it is possible to obtain the nanocomposite materials for various technological purposes. In the last decades the use of biopolymers in research and industry has significantly increased due to their low cost, renewability of sources, and nontoxic, environment friendly (e.g. 'green') processing. This has also been reflected in the metal–polymer nanocomposite research area where polysaccharide biopolymers, such as starch [6-7], and chitosan [8-12], proved to be good environments for controlled growth of semiconductive oxide nanoparticles.

Chitosan, a polysaccharide biopolymer obtained by deacetylation of chitin, due to the presence of both amino and hydroxyl groups in its monomers, exhibits excellent chelating and film-forming properties [13].

Another, widely unnoticed, property of chitosan is its photoluminescence in the ultraviolet region of electromagnetic radiation [14]. Recently, has been was shown that biopolymers containing ultraviolet emitting chromophores can be used to induce photochemical reactions [15-16]. The combination of inorganic agents Ag, ZnO, $SiO_2$, $TiO_2$ with organic polymer-chitosan has attracted intensive research interest because of its important biological applications especially in bactericidal effect. It has a significant potential for preventing infections, for healing wounds [17] and it has anti-inflammatory properties.

Hence, these composites have been incorporated into textile fabrics, polymers, dental material, medical device and burn dressing to eliminate microorganisms.

This paper reports studies on Ag:ZnO/chitosan composites with high antibacterial activities prepared by successfula chemical procedure. The resulting materials were investigated using electron microscopy (SEM). Also, the antimicrobial activity of the as prepared materials was measured.

## 2. Experimental details

### 2.1. Materials and microorganisms

Chitosan (low molecular weight), silver nitrate ($AgNO_3$), zinc acetate dihydrate ($Zn(O_2CCH_3) \cdot 2(H_2O)_2$) and lithium hydroxide (LiOH) were purchased from Sigma–Aldrich and used as received.

Antimicrobial susceptibility was performed on isolated bacteria from urine culture Gram-negative bacteria, *Escherichia coli (E. coli)* and the Gram-positive bacteria, *Staphylococcus aureus (S. Aureus)* on Mueller-Hinton agar.

### 2.2. Synthesis

ZnO is prepared by hydrolysis of zinc acetate in 2-propanol using lithium hydroxide.

Different amounts of $AgNO_3$ (0.1; 5 and 15 at%) and ZnO nanoparticles (0.035 M) were dissolved in 100 mL of 1% of aqueous solution to obtain silver and zinc cations. And 1.0 g of chitosan was added to the above solution. Then the mixture was sonicated for 20 minutes after magnetic stirring and then acidity was adjusted by adding 0.1 M NaOH solution (pH 4.8) to obtain clear sol.

Figure 1 presents the composite sols of ZnO/CS, Ag/CS and Ag:ZnO/CS.
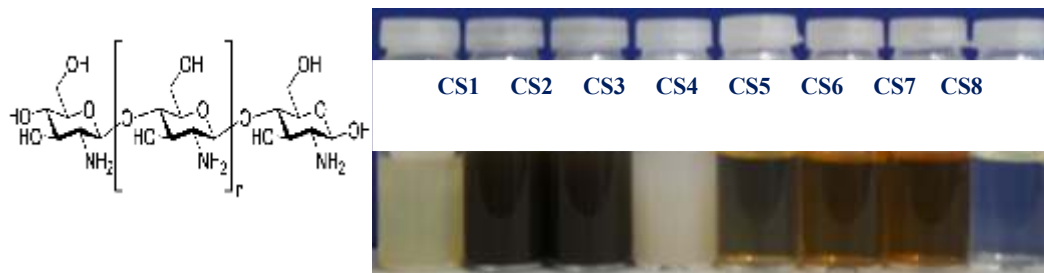


**Fig. 1**. *Aspect of composite sols of ZnO/CS, Ag/CS and Ag:ZnO/CS*

### 2.3. Characterization of Ag:ZnO/chitosan composites

The crystal structures of the product were identified by X-ray diffraction patterns DRON-3 diffractometer system (Burevestnik, USSR) with CoKα radiation, λ= 1.789 Å.

The morphology and the composition of the product were examined by scanning electron microscopy (SEM-Quanta 200), X-ray Energy Dispersive Spectrometer (EDS-FEI).

### 2.4. Antimicrobial testing

The antimicrobial activity of Ag/CS, ZnO/CS and Ag:ZnO/CS composites with respect to simple CS polymer was investigated by using the paper disc method on Mueller-Hinton agar without blood against the Gram-negative bacteria, *Escherichia coli (E. coli)* and the Gram-positive bacteria, *Staphylococcus aureus (S. Aureus)* on Mueller-Hinton agar with blood. For this has been used sterilized paper disc of 6 mm in diameter impregnated with 10 µL (5 mg/1 mL) solution of the composite. In each sterilized culture dish, 0.2 mL fresh broth cultured for 24 h was added followed by 20 mL melted nutrient agar medium at approximately 50 $^o$C. The dishes were then cooled down to room temperature before being ready for use.

The samples were then gently pressed against the medium plate to have good contact with the inoculated agar, then turned flat. The samples stayed in a constant temperature incubator at 37 ± 1 $^o$C for 24 h, before the inhibition zones were measured.

The method for antimicrobial testing was standardized by correlation of zone diameters with minimal inhibitory concentration determined in broth.

## 3. Results and discussions

### 3.1. XRD analysis

Fig. 2 shows the X-ray diffraction patterns of pure CS film (Fig. 2a) and Ag:ZnO/CS composites films (Fig. 2b). The structure of CS was affected by incorporation of Ag and ZnO nanoparticles which disrupted the regular order of polymer chains [18]. Compared to Fig. 1a, the diffraction pattern of the Ag:ZnO/CS composite films exhibited three additional peaks at 35.8$^o$, 36.8$^o$ and 38.4$^o$ (Fig. 1b),

which were assigned to the (1 0 0), (0 0 2), (1 0 1), planes of specific hexagonal zinc oxide nanoparticles. Besides, the peak at 39.5$^o$ indicated the presence of Ag as shown in Fig. 2b. These data revealed that it is the successful formation of Ag:ZnO/CS composites.
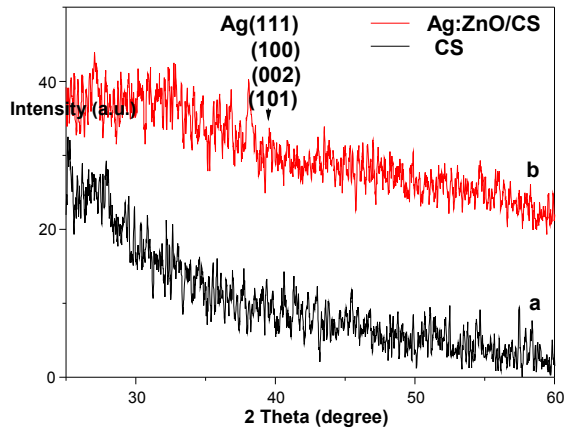


**Fig. 2.** *XRD patterns for a) CS pure film; b) Ag:ZnO/CS composite film*

## 3.2. Surface morphologies

Fig. 3 presents SEM images of pure CS film and Ag:ZnO/CS composite.

The pure chitosan film displayed a smooth surface (Fig. 2d). With doping Ag and ZnO, the surface of blend films became uneven and studded dense granule (Fig. 3a-c). The composite Ag:ZnO/CS is observed more even distribution compared to ZnO/CS where ZnO grain is higher due to agglomeration. Silver plays an important role in the distribution of nanoparticles in the chitosan matrix, as it can be observed in Fig. 3c.

The size of Ag and ZnO nanoparticles was in the range of 20–70 nm. Moreover, the particles had uniform distribution within chitosan polymer. Because the Ag content in the Ag:ZnO/CS composites was lower beyond the detection limit of EDX and Ag signals and the signals of noise coexisted, it only indicated the presence of Ag qualitatively. Fig. 4 illustrates the EDX spectrum of Ag:ZnO/CS, ZnO/CS, Ag/CS and CS nanocomposites. As shown in Fig. 4, C, Zn, O and Ag elements were identified. This result agreed well with XRD analysis.

## 3.3. Antimicrobial activities

The antimicrobial mechanism of chitosan was attributed to interaction with the strongly electronegative microbial surface [19].



**Fig. 3.** *SEM images for a) Ag:ZnO/CS; b) ZnO/CS; c) Ag/CS and pure CS*
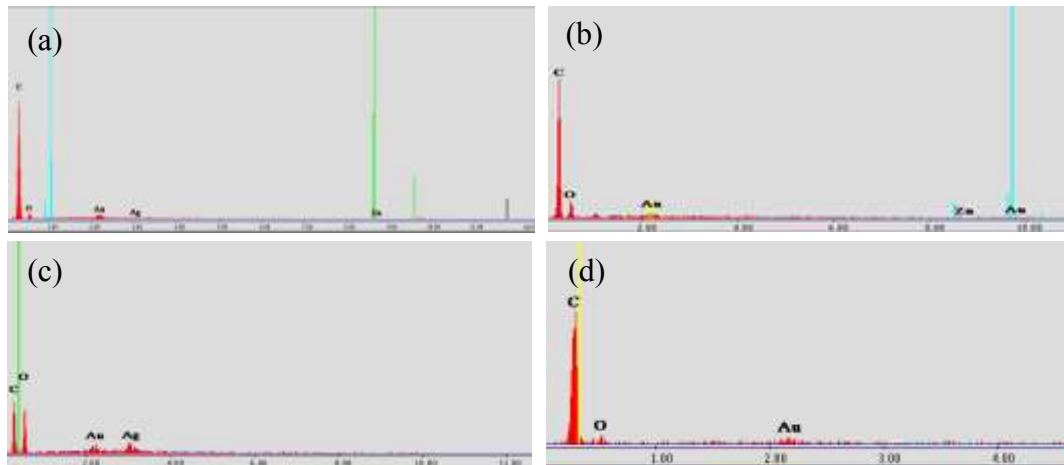
**Fig. 4.** *EDX spectrum for a) Ag:ZnO/CS; b) ZnO/CS; c) Ag/CS and pure CS*

Ag and ZnO nanoparticles embended in chitosan matrix depicted an enhanced antibacterial property. The experimental proofs suggest that the mechanisms of dominant bacterial ZnO is based on the production of reactive oxygen species (ROS - in particular in the presence of ultraviolet light), which chemically interact with the bacterial cell. [20-25]. Under light irradiation ZnO NPs (Eg = 3.37 eV) generated electron–hole pairs. The hole $(h^+)$ reacted with $OH^-$ on the surface of NPs, generating hydroxyl radicals $(OH^•)$, superoxide anion $(O^{2-})$ and perhydroxyl radicals $(HO_2^•)$. These highly active free radicals damaged the cells of microorganism as a result of decomposition and complete destruction [26-27].
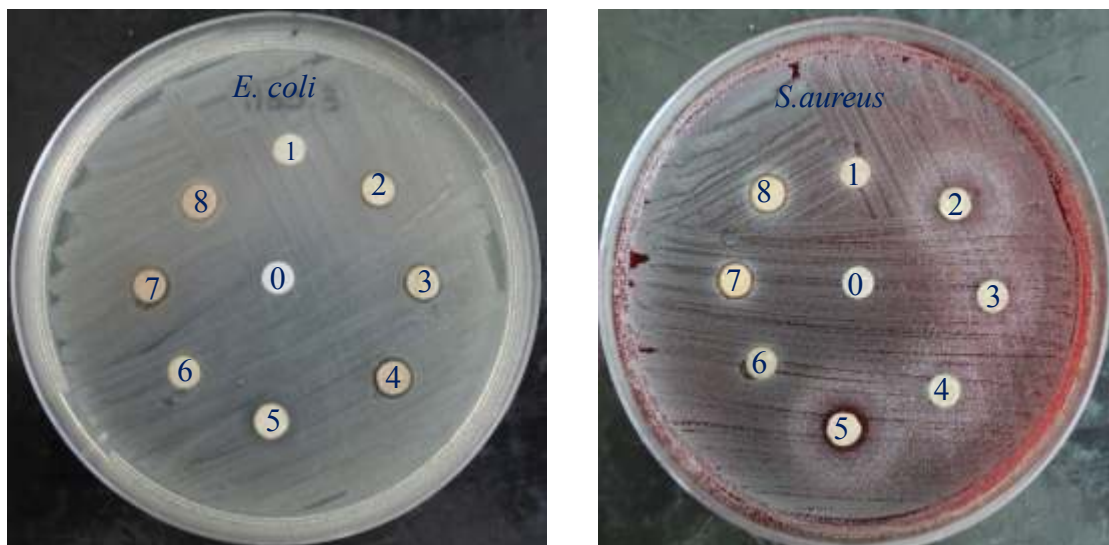


**Fig. 5.** *Zone of inhibition for 1) pure Chitosan (CS8); 2) Ag:ZnO/CS (CS1); 3) Ag:ZnO/CS (CS2); 4) Ag:ZnO/CS (CS3); 5) ZnO/CS (CS4); 6) Ag/CS (CS5); 7) Ag/CS (CS6); 8) Ag /CS (CS7)*

On the other hand, silver ions disrupt the DNA replication and cell division. Both antimicrobial agents appear to compromise the integrity of bacterial membrane because of chemical interactions.

In Fig. 5 is presented the antimicrobial activity of Ag:ZnO/CS, ZnO/CS, Ag/CS and CS nanocomposites. All the samples showed antimicrobial activity with bacterial viability.

The test of antimicrobial activities showed that Ag-doped ZnO/chitosan composite had higher antimicrobial activities than Ag/CS or ZnO/CS,

indicating that the Ag-doped ZnO nanoparticles enhanced the antimicrobial activities of chitosan based composite.

The CS4 sample (Ag:ZnO/CS blend films with 15 wt.% Ag and ZnO) showed excellent antimicrobial activities. Therefore, the presence of Ag and ZnO significantly enhanced antimicrobial ability of chitosan.

This points out that Ag-doped ZnO nanoparticles composite has potential application in medical and food packaging fields.

## 4. Conclusions

Ag:ZnO nanoparticles/chitosan composite were prepared via the sol-gel method. The dispersed ZnO and Ag-doped ZnO nanoparticles with spherical morphology had uniform distribution within chitosan polymer.

The final formulation was applied on filter paper discs for measuring the antimicrobial activities against *E.coli* and *S. Aureus*, using the disc difusion method.

All the samples showed antimicrobial activity with bacterial viability. The test of antimicrobial activities showed that Ag-doped ZnO/chitosan composite had higher antimicrobial activities than Ag/CS or ZnO/CS, indicating that the Ag-doped ZnO nanoparticles enhanced the antimicrobial activities of chitosan based composite. This points out that Ag-doped ZnO nanoparticles composite has potential application in medical and food packaging fields.

## Acknowledgements

## References

[1]. Y. Gao, R. Cranson - *Recent Advances in Antimicrobial Treatments of Textiles,* Textile Res. J., 78, 2008, p. 60-72.

[2]. Q. Lu, F. Gao, S. Komarneni - *A green chemical approach to the synthesis of tellurium nanowires*, Langmuir, 21, 2005, p. 6002-6005.

[3]. B. S. Liu, T. B. Huang - *Nanocomposites of genipin-crosslinked chitosan/silver nanoparticles - structural reinforcement and antimicrobial properties*, Macromol. Biosci., 8, 2008, p. 932–941.

[4]. A. Balamurugan, K. C. Ho, S. M. Chen - *One-pot synthesis of highly stable silver nanoparticles-conducting polymer nanocomposite and its catalytic application*, Synth Met., 159, 2009, p. 2544–2549.

[5]. J. Yang, Y. Zhang, S. Gautam, L. Liu, J. Dey, W. Chen, R. P. Mason, C. A. Serrano, K. A. Schug, L. Tang - *Development of aliphatic biodegradable photoluminescent polymers*, Proc. Natl. Acad. Sci., USA, 106(25), 2009, p. 10086-10091.

[6]. P. Raveendran, J. Fu, S.L. Wallen - *Completely "green" synthesis and stabilization of metal nanoparticles*, J. Am. Chem. Soc., 125, 2003, p. 13940-13941.

[7]. D. K. Božanić, V. Djoković, J. Blanuša, P. S. Nair, M. K. Georges, T. Radhakrishnan - *Preparation and Properties of Nano-sized Ag and Ag2S Particles in Biopolymer Matrix,* Eur. Phys. J. E, 22, 2007, p. 51-59.

[8]. C. M. Shih, Y. T. Shieh, Y. K. Twu - *Preparation of gold nanopowders and nanoparticles using chitosan suspensions*, Carbohydr. Polym., 78, 2009, p. 309-315.

[9]. A. Murugadoss, A. Chattopadhyay - *A 'green' chitosan–silver nanoparticle composite as a heterogeneous as well as micro-heterogeneous catalyst*, Nanotechnology, 19, 2008, p. 015603-01612.

[10]. C. M. Sun, R. J. Qu, H. Chen, C. N. Ji, C. H. Wang, Y. Z. Sun, B. H. Wang - *Degradation behavior of chitosan chains in the 'green' synthesis of gold nanoparticles,* Carbohydr. Res. 343, 2008, p. 2595-2599.

[11]. D. W. Wei, W. P. Qian - *Facile synthesis of Ag and Au nanoparticles utilizing chitosan as a mediator agent*, Colloids Surf. B Biointerfaces, 62(1), 2008, p. 136–142.

[12]. D. W. Wei, W. P. Qian, D. J. Wu, Y. Xia, X. J. Liu - *Synthesis, properties, and surface enhanced Raman scattering of gold and silver nanoparticles in chitosan matrix*, J. Nanosci. Nanotechnol., 9, 2009, p. 2566–2573.

[13]. E. I. Rabea, M. E.-T. Badawy, C. V. Stevens, G. Smagghe, W. Steurbaut - *Chitosan as antimicrobial agent: applications and mode of action.* Biomacromolecules, 4, 2003, p. 1457-1465.

[14]. F. L. Mi - *Synthesis and characterization of a novel chitosan-gelatin bioconjugate with fluorescence emission*, Biomacromolecules, 6, 2005, p. 975-987.

[15]. M. Nowakowska, M. Sterzel, K. Szczubiałka, J. E. Guillet - *Photoactive Modified Hydroxyethylcellulose*, Macromol. Rapid Commun., 23, 2002, p. 972-974.

[16]. S. Wu, F. Zeng, H. Zhu, Z. Tong - *Energy and electron transfers in photosensitive chitosan*, J. Am. Chem. Soc., 127, 2005, p. 2048–2049.

[17]. B. S. Atiyeh, M. Costagliola, S. N. Hayek, S. A. Dibo - *Effect of silver on burn wound infection control and healing: review of the literature*, Burns., 33, 2007, p. 139-148.

[18]. Z. F. Dong, Y. M. Du, L. H. Fan, Y. Wen, H. Liu, X. H. Wang - *Preparation and properties of chitosan/gelatin/nano-TiO2 ternary composite films*, J. Funct. Polym., 17, 2004, p. 61–66.

[19]. S. W. Fang, C. F. Li, D. Y. C. Shih - *Antifungal activity of chitosan and its preservative effect on low-sugar candied kumquat*, J. Food Prot., 57, 1994, p. 136–140.

[20]. X. H. Wang, Y. M. Du, H. Liu - *Preparation, characterization and antimicrobial activity of chitosan-Zn complex*, Carbohydr. Polym., 56, 2004, p. 21–26.

[21]. Y. Inoue, Y. Kanzaki - *The mechanism of antibacterial activity of silver-loaded zeolite*, J. Inorg. Biochem., 67, 1997, p. 377-377.

[22]. A. Bacchi, M. Carcelli, P. Pelagatti, C. Pelizzi, G. Pelizzi, F. Zani - *Antimicrobial and mutagenic activity of some carbono- and thiocarbonohydrazone ligands and their copper(II), iron(II) and zinc(II) complexes*, J. Inorg. Biochem., 75, 1999, p. 123–133.

[23]. Z. H. Yang, C. S. Xie, X. P. Xia, S. Z. Cai - *$Zn^{2+}$ release behavior and surface characteristics of Zn/LDPE nanocomposites and ZnO/LDPE nanocomposites in simulated uterine solution*, J. Mater. Sci. Mater. Med., 19, 2008, p. 3319–3326.

[24]. E. P. Azevedo, T. D. P. Saldanha, M. V. M. Navarro, A. C. Medeiros, M. F. Ginani, F. N. Raffin - *Mechanical properties and release studies of chitosan films impregnated with silver sulfadiazine,* J. Appl. Polym. Sci., 102, 2006, p. 3462–3470.

[25]. Y. M. Qin, C. J. Zhu, J. Chen, Y. Z. Chen, C. Zhang - *The absorption and release of silver and zinc ions by chitosan fibers,* J. Appl. Polym. Sci., 101, 2006, p. 766–771.

[26]. Y. Kikuchi, K. Sunada, T. Iyoda, K. Hashimoto, A. Fujishima - *Photocatalytic bactericidal effect of TiO2 thin films: dynamic view of the active oxygen species responsible for the effect*, J. Photochem. Photobiol. A, 106, 1997, p. 51–56.

[27]. B. Halliwell, J. M. C. Gutteridge - *Oxygen toxicity, oxygen radicals, transition metals and disease,* Biochem. J., 219, 1984, p. 1–14.

# COMPARATIVE CHARACTERISTICS OF MARTENSITE AND BAINITE IN Cu-BASED SMAs

**Elena MIHALACHE, Monica-Nicoleta LOHAN, Bogdan PRICOP,
Leandru-Gheorghe BUJOREANU, Marius-Gabriel SURU***

Faculty of Materials Science and Engineering, "Gheorghe Asachi" Technical University of Iaşi,
61A Avenue D. Mangeron, 700050 Iaşi, Romania
*Corresponding author
e-mail: marius_suru2005@yahoo.com

## ABSTRACT

*The present work reports the evolution of micro-structure and shape memory behavior in a Cu-15 Zn-6 Al (mass. %) shape memory alloy (SMA), as a function of the applied hot working procedure and of the performed heat treatments. To this purpose a special compressed-air forging hammer was employed. The samples were heated up to 1023 K into an electric furnace and swaged on a compressed-air forging hammer, by multiple blows. After several blows, the specimens were prepared, by maintaining the main plastic deformation direction, for structural analysis, being cut, embedded, ground, polished and etched. Structural analysis comprised optical (OM) and scanning electron (SEM) microscopy observations, performed with the view of emphasizing the morphological aspects of martensite and bainite. To reveal the atomic fluctuations, enabled by hot forging, energy dispersive X-ray spectroscopy analysis (EDS) measurements were performed by means of SEM analysis. The paper reports the results of OM, SEM and EDS observations, by corroborating the results obtained in martensite and bainite.*

KEYWORDS: shape memory alloy, hot forging, martensite, bainite, scanning electron microscopy, atomic fluctuations

## 1. Introduction

"Shape memory" is the term used to describe a unique property of some materials that undergo the thermoelastic martensitic reaction [1]. It is widely accepted that there are presently five types of commercial shape memory alloys (SMAs): (i) Ni-Ti-based; (ii) Cu-Zn-Al-based [2]; (iii) Cu-Al-Ni-based; (iv) Fe-Mn-Si-based [3] and (v) Fe-Ni-Co-based. Thus, many alloys exhibit shape memory effect (SME) [4], but Ni–Ti-based shape memory alloys have up to date provided the best combination of materials properties for most commercial applications. Cu-based SMAs [5] are the most promising in practical use because of their low price, high recovery force and because they provide a more economical alternative to Ni-Ti SMAs. Cu–Zn–Al alloys are now the most popular Cu-based SMAs and presently available on the market [6]. However they exhibit poor ductility problems, martensitic stability and intergranular crack, which are disadvantages to their applications [7].

The so-called SME in copper-based alloys is intrinsically related to the martensitic transformation which occurs from the austenite phase (β) [8] to the martensite (β') [9]. Specifically, in Cu–Zn–Al alloys [10], the SME [11] is only observed for a certain range of composition [12] which in general contains Cu–(16–30)Zn–(4–8)Al (wt.%) [13]. With respect to this compositional range, three equilibrium phases (α, β and γ) [14] may occur as well as their respective martensitic ones, typically denoted as α', β' and γ' [15]. The only phase that presents the SME is the β one. The β-phase in Cu–Zn–Al alloys is disordered at high temperatures and has a bcc lattice. During the cooling process, the parent β-phase may give rise to two different superlattice structures, depending on the temperature and alloy composition, by means of an ordering reaction. These structures are normally designated as $\beta_2$ (B2) and $\beta_3$ (L2$_1$). By stress-induced or thermally [16], the $\beta_2$ or $\beta_3$ austenite phases are transformed into the β' one (martensite) which is also known as 9R [17] due to the rhombohedral lattice and stacking of 9 compact plans.

In contrast to martensite transformation, bainite transformation [18] is of diffusion-controlled type because no intermediate, transition lattice was observed even in the very tip of the bainite plate. After several decades of intensive fundamental research of bainite transformation in steels [19], various issues are still not fully understood such as bainite formation from plastically deformed austenite and its large growth rate and autocatalytic nucleation [20]. The purpose here has been to emphasize the comparative morphological aspects of martensite and bainite as a function of the applied hot working procedure and of the performed heat treatments.

## 2. Experimental procedure

A conventional SMA with nominal chemical composition Cu-15 Zn-6 Al (mass %) was melt in an induction furnace, cast and normalized. From the obtained specimens, $5 \times 10^{-3}$ m-thick samples were cut in order to be plastically deformed by hot forging. The plastic deformation process consisted in repetitive forging of billets transversally cut from cylindrical ingots.

The billets were heated up to 1023 K, into an electric furnace and swaged on a compressed-air forging hammer, by multiple blows until sample's thickness was reduced from 5 to $2 \times 10^{-3}$ m. From repeatedly hot forged samples, different specimens were homogenized at 1073 K, tempered at 573 and 673 K and finally cooled in water [21].

For structural analysis, the specimens were cut, embedded, ground, polished and etched. Embedding was performed into bi-component cold mounting resin. Grinding was done with abrasive paper with meshes raging between 600 and 2400, under intense water cooling, in order not to affect the thermomechanical history of the specimens. Polishing was achieved in two stages.

Firstly the specimens were manually polished with 6 μm diamond paste and then were automatically polished with 0.3 μm and finally with 0.04 μm alumina powder solution, diluted in a ratio of 1:10. Chemical etching, which is essential for a proper visualization of surface structure [20] was carried out with 30% $HNO_3$ in 100 ml aqueous solution.

Comparative structural analysis comprised optical (OM), scanning electron microscopy (SEM) and energy dispersive X-ray spectroscopy analysis (EDS), performed with the aiming to emphasize the micro-structural effects, of the above mentioned plastic deformation process and the performed heat treatments, on martensite and bainite plate morphology. OM micrographs were recorded with an OPTIKA XDS-3 MET microscope equipped with OPTIKAM 4083.B5 microscopy digital USB camera and OPTIKAM B5 software. SEM and EDS analyses were recorded using a SEM—VEGA II LSH

TESCAN microscope, coupled with an EDX—QUANTAX QX2 ROENTEC detector.

## 3. Results and discussions

The first series of OM micrographs, revealing general aspects concerning the effects of the hot forging and of the performed heat treatments, are summarized in Fig. 1 The representative detailed aspects of martensite plates of specimens tempered at 573 K are illustrated in Fig. 1(b). The micrographs represent a martensitic type structure (M) with a Zig-Zag morphology. One can, observe on the corners of the plates, the central ribs corresponding to the first twining plan. The variations of martensite plates (V1 and V2) with different contrast (light-dark) are symmetrically disposed to the central midrib. The primary martensite plates can be distinguished easily thanks to their micrometric dimension and the secondary plates are thinner, being disposed within primary ones.
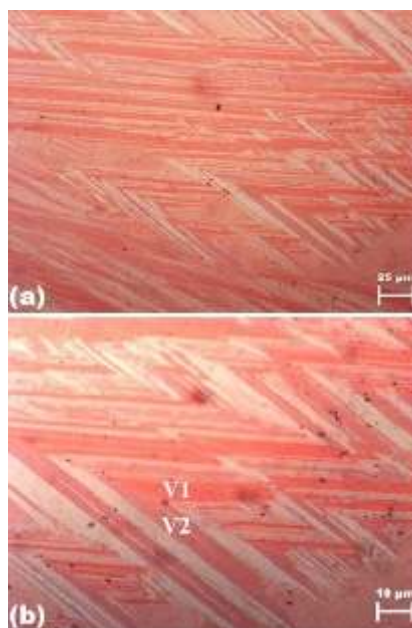


***Fig. 1.*** *OM micrographs of specimens tempered at 573 K (a) general aspect; (b) detailed aspect of martensite plates on the surface of specimens*

The martensite plate variants V1 and V2, which are in the twining relation, together with the presence of central midrib, are characteristic features to the diamond-type structure. In the detwining area the presence of austenite (A) can be observed.

The displacement mode of the bainite lamellar structure on the surface of the specimens is summarized in Fig. 2. In the optical micrographs from Figures. 2(a) and (b) the parallel disposal of bainite plates and their submicron thickness can observed.
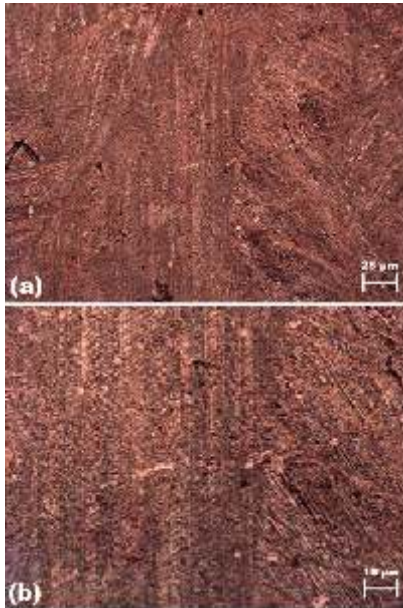
***Fig. 2.*** *OM micrographs of specimens tempered at 673 K (a) general aspect; (b) detail of bainite lamellar structure, illustrating their displacement mode on the surface of the sample*
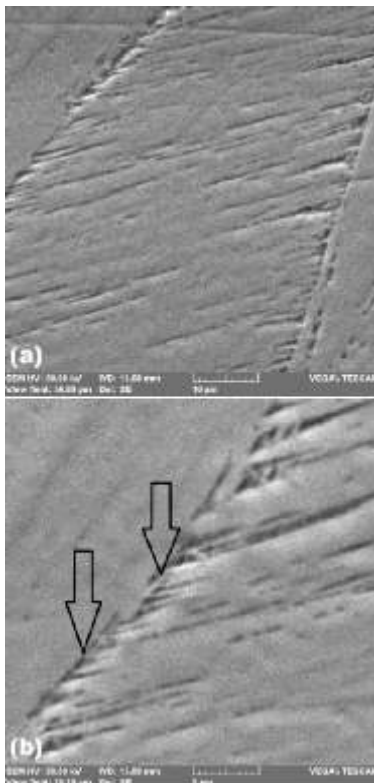


***Fig. 3.*** *Characteristic SEM micrographs of specimens tempered at 573 K (a) general aspect; (b) detail of martensite plates with localization of central midrib*

Figure 3 provides details, by means of SEM micrographs, of martensite plates on the same specimens as Fig. 1. The SEM micrographs are showing parallel and relatively small depth martensite plates. On the micrograph it was marked through a double arrow the position of the central rib, identified in Fig. 1. Thus, the substructure of martensite plates can be observed at higher power magnification, such as Fig. 3(b), where it can be seen that the martensite plates have the thickness order of 10 μm, and the subplates the order of 2-3 μm.
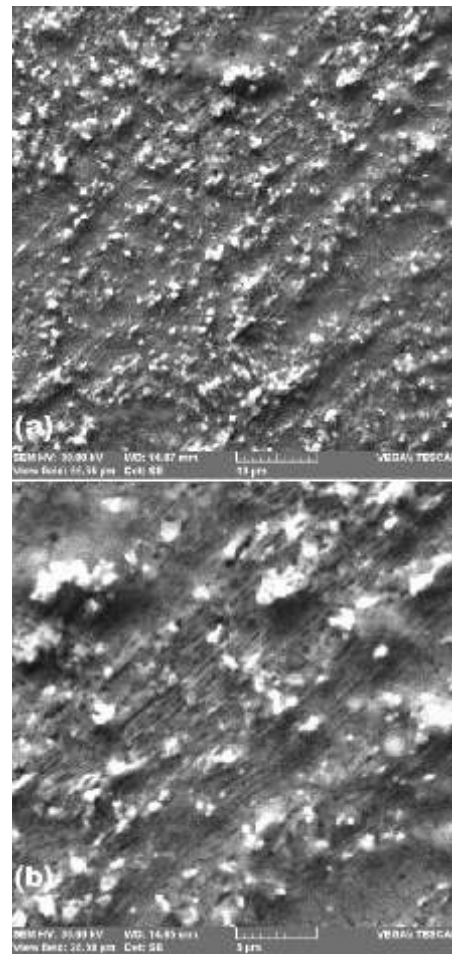


***Fig. 4.*** *Characteristic SEM micrographs of specimens tempered at 673 K (a) general aspect; (b) detail of bainite structure*

A series of additional morphological details are noticeable in Fig. 4, on the same specimens used in Fig. 2. Knowing that bainite features include the platiform aspects, the presence of internal ribs, distributed irregularly and having micro-twining aspect, it can be said that the structure in Fig. 4 belongs to bainite. The internal ribs are so fine that they cannot be observed only at a higher power magnification, such as the example in Fig. 4(b).
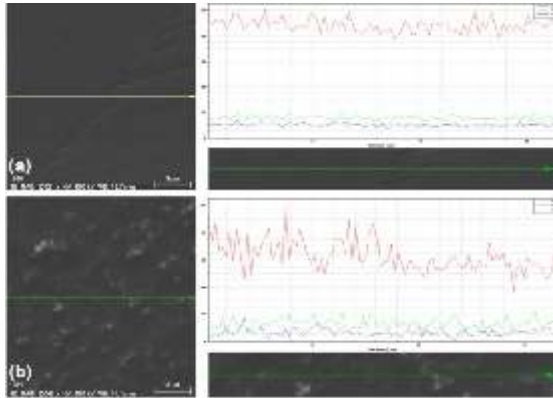
***Fig. 5.*** *Typical EDS analysis illustrating the position of composition line and corresponding atomic fluctuations: (a) martensite (573 K tempering); (b) bainite (tempering 673 K)*

To emphasize the controlled character by diffusion of bainite growth, it was made EDS analysis, aiming at the difference between martensite and bainite, the results are presented in Fig. 5. The results show clearly that between martensite and bainite there is a significant atomic migration. As the martensitic transformation is diffusion free, the one that could produce atomic movement from the equilibrium positions is the increase of bainite that is produced by diffusion.

The chemical composition fluctuations from Fig. 5(a), corresponding to martensite, have cca. 40% at. on Cu and aprox 10% at. on Zn and Al. In contrast with these values, the bainite specimens were max 20% at. on Cu, respectively 5% at. on Zn and Al.

## 4. Conclusions

In this paper the morphological, mechanical and structural main features of martensite and bainite were presented. In this way a bibliographic synthesis, including the historical evolution, the characteristics and development prospects of bainite steels were developed.

Based on the platiform character printed by plates with irregular internal ribs with micro-twin aspect and the controlled increase of bainite, has been identified his present in CuZnAl shape memory alloy, homogenized and tempered at 673 K.

By means of optical and electronic microscopy was revealed a clear differentiation between bainitic and martensitic structures. With the aid of X - ray dispersion analysis (EDS), the study highlighted the atomic fluctuation increase, which assigned the bainite difussional carachter, as follows: on martensite (tempering 573 K) Cu fluctuated by max 20% at., and on bainite (tempering 673 K) fluctuated aprox. 40% at. Similarly at Zn and Al fluctuated by aprox. 10% at. on bainite.

## Acknowledgement

## References

[1]. C. Y. Chung, C. W. H. Lam - *Cu-based shape memory alloys with enhanced thermal stability and mechanical properties*, Materials Science and Engineering: A, 273–275, 1999, p. 622-624.

[2]. M.-G. Suru, C. Moroşanu, L.-G. Bujoreanu - *Variation tendencies of shape memory alloys surface relief as a function of training-cycling parameters*, Journal of optoelectronics and advanced materials, 16, 2014, p. 394 – 400.

[3]. M.-G. Suru, I. Dan, N. M. Lohan, A. L. Paraschiv, B. Pricop, I. P. Spiridon, C. Baciu, L.-G. Bujoreanu - *Effects of hot working procedure on surface relief characteristic in an Fe–Mn–Si–Cr shape memory alloy*, Mat.-wiss. u. Werkstofftech., 45, 2014, p. 44-50.

[4]. H. LIU, N. SI, G. XU - *Influence of process factors on shape memory effect of CuZnAl alloys*, Transactions of Nonferrous Metals Society of China, 16, 2006, p. 1402-1409.

[5]. J. Fernandez, X. M. Zhang, J. M. Guilemany - *A one-cycle training technique for copper-based shape memory alloys*, Journal of Materials Processing Technology, 139, 2003, p. 117-119.

[6]. C. E. Sobrero, P. La Roca, A. Roatta, R. E. Bolmaro, J. Malarría - *Shape memory properties of highly textured Cu–Al–Ni–(Ti) alloys*, Materials Science and Engineering: A, 536, 2012, p. 207-215.

[7]. J. M. Jani, M. Leary, A. Subic, M. A. Gibson - *A review of shape memory alloy research, applications and opportunities*, Materials & Design, 56, 2014, p. 1078-1113.

[8]. L.-G. Bujoreanu - *On the influence of austenitization on the morphology of α-phase in tempered Cu–Zn–Al shape memory alloys*, Materials Science and Engineering A, 481–482, 2008, p. 395–403.

[9]. R. S. Elliott, D. S. Karls - *Entropic stabilization of austenite in shape memory alloys*, Journal of the Mechanics and Physics of Solids, 61, 2013, p. 2522-2536.

[10]. M.-G. Suru, A.-L. Paraschiv, N. M. Lohan, B. Pricop, B. Ozkal, L.-G. Bujoreanu - *Loading Mode and Environment Effects on Surface Profile Characteristics of Martensite Plates in Cu-Based SMAs*, Journal of Materials Engineering and Performance, online first, DOI: 10.1007/s11665-014-0951-6.

[11]. M.-G. Suru, L.-G. Bujoreanu - *Comparative topographic study of surface micro-relief of primary martensite plates in shape memory alloys with different crystalline structures*, Mat.-wiss. u.Werkstofftech, 43, 2012, p. 973-978.

[12]. M. Blanco, J. T. C. Barragan, N. Barelli, R. D. Noce, C. S. Fugivara, J. Fernández, A. V. Benedetti - *On the electrochemical behavior of Cu–16%Zn–6.5%Al alloy containing the β'-phase (martensite) in borate buffer*, Electrochimica Acta, 107, 2013, p. 238-247.

[13]. J. X. Zhang, Y. X. Liu, W. Cai, L. C. Zhao - *The mechanisms of two way-shape memory effect in a Cu-Zn-Al alloy*, Materials Letters, 33, 1997, p. 211-214.

[14]. R. Abeyaratne, J. K. Knowles - *On the kinetics of an austenite → martensite phase transformation induced by impact in a Cu-Al-Ni shape-memory alloy*, Acta Materialia, 45, 1997, p. 1671-1683.

[15]. A. M. Furlani, M. Stipcich, R. Romero - *Phase decomposition in a β Cu–Zn–Al–Ti–B shape memory alloy*, Materials Science and Engineering: A, 392, 2005, p. 386-393.

**[16]. N. F. Kennon, D. P. Dunne -** *Shape strains associated with thermally-induced and stress-induced martensite in a Cu-Al-Ni shape memory alloy*, Acta Metallurgica, 30, 1982, p. 429-435.

**[17]. M. G. Suru, A. L. Paraschiv, B. Pricop, L. G. Bujoreanu -** *A statistical evaluation of thermomechanical loading effects on martensite plate morphology in CuZnAl SMAs*, Optoelectronics and advanced materials – rapid communications, 7, 2013, p. 141 – 144.

**[18]. L. G. Bujoreanu, S. Stanciu, P. Bârsănescu, N. M. Lohan -** *Study of the transitory formation of α1 bainite, as a precursor of α-phase in tempered SMAs*, Proc. of SPIE, 7297, 2009, 72970B-1-5.

**[19]. G. Sidhu, S. D. Bhole, D. L. Chen, E. Essadiqi -** *An improved model for bainite formation at isothermal temperatures*, Scripta Materialia, 64, 2011, p. 73-76.

**[20]. O. Bouaziz, P. Maugis, J. D. Embury -** *Bainite tip radius prediction by analogy with indentation,* Scripta Materialia, 54, 2006, p. 1527–1529.

**[21]. G. Vitel, A. L. Paraschiv, M. G. Suru, N. Cimpoeşu, L.-G. Bujoreanu -** *Tempering effects in a normalized hot forged Cu-Zn-Al shape memory alloy*, Optoelectronics and advanced materials – rapid communications, 6, 2012, p. 339-342.

# DYNAMICS OF NUTRIENTS IN AQUATIC ECOSYSTEMS: THE CASE STUDY OF CIRIC BASIN RIVER AT NORD OF IAŞI CITY

**Lavinia TOFAN[1], Rodica WENKERT[2*],**
**Carmen PĂDURARU[1], Ovidiu TOMA[3]**

[1]Department of Environmental Engineering and Management, "Gheorghe Asachi" Technical University of Iasi, 73, Prof. Dr.D. Mangeron Street, 700050 Iasi, Romania
[2]'Soroka University Medical Center, Beer-Sheva, Israel
[3]Department of Biochemistry, "Al. I. Cuza" University of Iasi, Faculty of Biology,
20A Bd. Carol I, 700505 Iasi, Romania
*Corresponding author;
e-mail: rodicawe@clalit.org.il

## ABSTRACT

*A 1 year dynamics of two biologically limiting nutrients (N and P) has been carried out in the Ciric basin river at nord of Iasi City. The total nitrogen concentrations varied from 7.55-17.55 mg N/L and total phosphorus concentrations fluctuated between 0.84 and 1.428 mgP/L. According to our experimental data concerning the total nitrogen concentrations, the highest level of pollution is recorded in the spring region of the Ciric brook. The results obtained on the phosphorus content confirm the increase of the pollution degree with carrying phosphorus substances. It is obvious that the waters of Ciric lake rapidly shifted to a hypertrophic status.*

KEYWORDS: dynamics, nutrients, total nitrogen, phosphorus, Ciric river

## 1. Introduction

Increasing nutrient enrichment of aquatic ecosystems is a widespread and significant threat around the world. The increased nutrient supply results in higher biological productivity and often leads to undesirable effects including algal blooms and depletion of oxygen in bottom waters.

The process of eutrophication is greatly increased by various human activities. Phosphorus (P) and nitrogen (N) resulting from agricultural and urban activities are now recognized to be major causes of human-driven eutrophication [1].

This is the most common impairment of surface waters, affecting lakes, rivers and estuaries. Among the most threatened lakes and rivers are those located in or near urban settlements, because of various effluent sources [2].

These sources can be separated into point sources such as municipal waste water treatment plants and industrial discharges and nonpoint sources which include agricultural runoff of fertilizers and animal waste, urban runoff such as pet waste, atmospheric deposition and construction runoff.

The relative importance of different nutrient sources varies spatially and temporally. Generally, the nonpoint sources are responsible for most delivery of N and P. According to literature data, over half of the rivers studies received >90% of their N and one-third of the rivers studied received >90% from nonpoint sources [3]. However, point sources of N and P can contribute over half of the N and P load to urban river reaches [3]. Thus, although lake ecosystems constitute an essential resource for many ecosystem service and human activities, urban lakes often exhibit serious degradation and interfere with these services and benefits [4]. However, with a proper management lakes can be important tourist and fish-culture centres capable of stimulating regional revenue. Over the past decades, the Ciric basin river, at nord of Iaşi city, previously an excellent leisure centre has been suffering increasing degradation.

The pond has been threatened for years by phytoplankton, blooms and dense floating growths of maesophytes, both indicating poor ecosystem health.
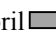
In this context, in order to asses the Ciric's trophic status and to propose measures for controlling its degradation process, a study of nutrient dynamics

in Ciric basin river, at nord of Iaşi city has been carried out.

## 2. Experimental results

Ciric River is part of plain water with a slow flow regime and reduced flow. Dorobant Aroneanu, Ciric I and II lakes, represents the surface water, whose load natural places them in a category lower, especially in summer, when biological growth conditions. Ciric water quality is influenced by the vicinity of the four municipalities located entirely Ciric river basin. The river bathymetry map is presented in figure 1.

Water samples were collected between March and November 2007:
- march-april ⬜ ;
- may-june ▦ ;
- october-november ⬛ .

The sampling station was: 1-from origin of Ciric river; 2, 3-from Dorobant lake; 4, 5-from Aroneanu lake; 6, 7-from Ciric I and 8-from Ciric II.

Analyses performed in the laboratory included:

- Total phosfhorus, ammonium-nitrogen, nitrate and nitrite concentrations was determined by spectrophotometric methods using a spectrophotometer JK-UVS-752N.

- Total nitrogen was determined by Kjeldhal method.



**Fig. 1.** *The map of Ciric river with the four lakes and the sampling stations (1, 2, 3, 4, 5, 6, 7, 8)*

Prior to spectrophotometer measurement, samples were subjected to a mineralization process, using the persulphate digestion technique for total phosfhorus, and a catalytic mixture (1/3 sulfuric acid + 2/3 hydrogen peroxide) for total nitrogen.

## 3. Results and Discussion

### 3.1. Dynamics of N in Ciric basin river

Nitrogen exists in lakes and rivers as *mineral nitrogen* (nitrates, nitrites and ammonium) and *organic nitrogen*, associated to the structures of proteins, peptides, nucleic acids and urea type. In normal conditions of oxygenation, nitrogen is present especially as nitrates. The nitrite and ammonium forms are present in the case of organic disfunctionality, being toxic to the living organisms. Usually these forms are rare and transitive in any case.

The analyses carried out in different sectors of the Ciric basin river have been lead to average values of the total nitrogen concentrations ranged from 10.00-17.55 mg N/L in the period of March-April 2007 and 7.55-13.2 mg N/L in May-June period of 2007, respectively (figure 2). As it was expected, the concentration of total nitrogen exhibits a decrease in the warm period of year, when some structures containing nitrogen are consumed by the phytoplankton.

**Total nitrogen concentrations, mg/L**
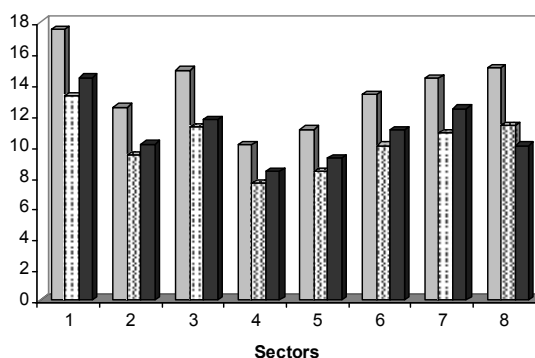


**Fig. 2.** *The gradient of total nitrogen concentrations*

As in all statistical studies is shown, the temperature decrease in the months of fall results in the increases of total nitrogen concentration. The recorded degree of increase is lower than the estimated values. This fact may be explained by correlation with relative high temperatures on the sampling periods. The lowest value of 8.32 mg N /L has been obtained for the sample 4, tail Dorobanţ

lake. According to our experimental data, the highest level of pollution is recorded in the spring region of the Ciric brook. The single explanation is the pollution of the phreatic layer with animal wastes from the former Popricani farm of pigs. The content of nitrate decreases downstream by dilution.

The main component of the total nitrogen is the *organic nitrogen* (figure 3), representing an average of about 61% and 66.7% in the spring and summer period, respectively. In the colder months of fall, the organic nitrogen concentration ranged from 72 to 88% of the total content. The content of organic nitrogen has a complex enough dynamics, depending on the hydrological and hydrobiological regime of waters. Its weight is increasing with lapse to the warm periods of the year. The increasing trend is maintained in the warm periods of the fall, also.

**Organic nitrogen concentrations, mg/L**
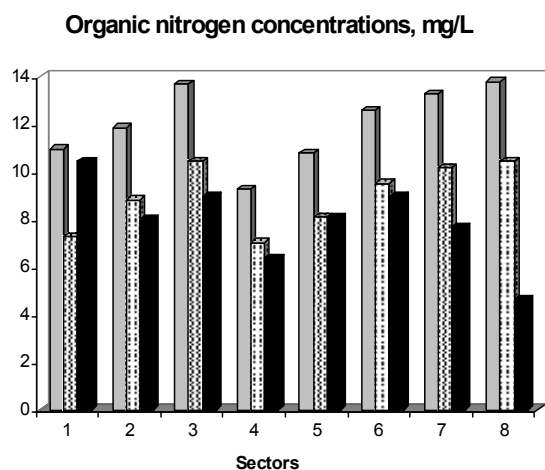


***Fig. 3.*** *The variation of organic nitrogen concentration*

The *mineral nitrogen* reunites the contribution of ammonium ion, nitrates and nitrites (figure 4). The whole of mineral nitrogen records a decrease of its absolute value on the spring-summer lapse. On an average the decrease is of about 43%. The value record an increase to the fall period, correlated to the nitrate content increase, properly to the periods of phytoplankton amount diminishing.

**Mineral nitrogen concentrations, mg/L**
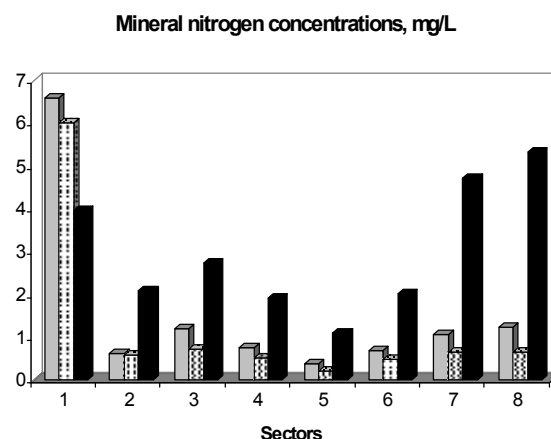


***Fig. 4.*** *The variation of mineral nitrogen concentration*

The concentration of nitrogen from *nitrates* is prevailed in the whole concentration of the mineral nitrogen (table 1). Excepting of the first sample, the content of nitrate (on absolute value) is relatively low, ranging from 0.4-1.3 mgN/L on March – April 2007 period and 0.2 – 0.9 mg N /L in the summer period for all the other samples. These low values are specific to the waters in which this compound is consumed by phytoplankton in the warm periods.

***Table 1.*** *The concentration of nitrogen from nitrates in the water samples under investigation*

| Sectors | Spring March-April 2007 | Summer May-June 2007 | Fall October-November 2007 |
|---|---|---|---|
| | [mg/L] | | |
| 1 | 6.33 | 5.46 | 3.64 |
| 2 | 0.49 | 0.224 | 1.84 |
| 3 | 0.894 | 0.483 | 2.28 |
| 4 | 0.555 | 0.352 | 1.58 |
| 5 | 0.253 | 0.104 | 0.91 |
| 6 | 0.497 | 0.267 | 1.61 |
| 7 | 0.930 | 0.526 | 4.45 |
| 8 | 1.066 | 0.673 | 5.05 |

The values record significant increases running to about an order of magnitude in the cold period of the fall. This trend is in good agreement with the phytoplankton evolution. Again, excepting of values corresponding to the first point of sampling, the content of nitrate ion was recorded in 2007 year an increasing trend during the accumulation of waters discharged by the river localities.

The *nitrites* have significant minor contributions and exhibit a concentration decrease on spring-

summer lapse (table 2). The explanation is based on the unstable and transient character of this structure. It may be noticed that the nitrite consumption in the processes of oxidation or reduction is intensified by the increase of temperature and partners concentration.

*Table 2. The concentration of nitrogen from nitrites in the water samples under investigation*

| Sectors | Spring March-April 2007 | Summer May-June 2007 | Fall October-November 2007 |
|---|---|---|---|
| | [mg/L] | | |
| 1 | 0.094 | 0.054 | 0.0055 |
| 2 | 0.0034 | 0.0020 | 0.0022 |
| 3 | 0.049 | 0.028 | 0.026 |
| 4 | 0.0245 | 0.14 | 0.027 |
| 5 | 0.0082 | 0.0052 | 0.024 |
| 6 | 0.0085 | 0.0052 | 0.028 |
| 7 | 0.0116 | 0.0037 | 0.038 |
| 8 | 0.0048 | 0.0028 | 0.018 |

For the most samples, the values recorded an increase with temperature decrease in the colder months of fall.

The nitrogen content due to the presence of *ammonium* ion records an increase in the summer period (table 3).

This evolution may be explained on the basis of more intense activity of the bacteriophytoplankton specific to the ammonification process.

The obtained values decrease in the fall months remaining superior to those recorded in March-April months.

*Table 3. The concentration of nitrogen from ammonium in the water samples under investigation*

| Sectors | Spring March-April 2007 | Sommer May-June 2007 | Fall October-November 2007 |
|---|---|---|---|
| | [mg/L] | | |
| 1 | 0.164 | 0.476 | 0.328 |
| 2 | 0.148 | 0.338 | 0.254 |
| 3 | 0.264 | 0.776 | 0.421 |
| 4 | 0.171 | 0.551 | 0.319 |
| 5 | 0.119 | 0.464 | 0.174 |
| 6 | 0.205 | 0.721 | 0.379 |
| 7 | 0.120 | 0.446 | 0.239 |
| 8 | 0.171 | 0.726 | 0.262 |

*Table 4. Integration of Ciric waters into quality degrees/N regime*

| Quality degree | | | | | | | | | | | | |
|---|---|---|---|---|---|---|---|---|---|---|---|---|
| | Spring | | | | Summer | | | | Fall | | | |
| Quality indicator | N-NH$_4^+$ | N-NO$_2^-$ | N-NO$_3^-$ | N$_{total}$ | N-NH$_4^+$ | N-NO$_2^-$ | N-NO$_3^-$ | N$_{total}$ | N-NH$_4^+$ | N-NO$_2^-$ | N-NO$_3^-$ | N$_{total}$ |
| Dorobanţ Lake | I | II–III | I | III | I-II | I-II | I | II-III | I | I-II | I-II | II-III |
| Aroneanu Lake | I | I–II | I | III–IV | I-II | I | I | II-III | I | I-II | I-II | II-III |
| Ciric I Lake | I | I | I | III–IV | I-II | I | I | II-III | I | I-II | II | II-III |
| Ciric II Lake | I | I | I | III–IV | I-II | I | I | II-III | I | I-II | II-III | II-III |

The obtained values decrease in the fall months remaining superior to those recorded in March-April months.

On the basis of nitrogen dynamics the Ciric waters may be integrated on the quality grades presented in Table 4.

## 4. Dynamics of P in Ciric basin river

It is unanimously recognized that the phytoplankton development is controlled by the concentration of total phosphorus in water.

However, the researches emphasized that the N: P ratios are more important relative to the level of phosphorus concentration. Thus, numerous studies at scales from algal cultures to whole lakes manipulations have been demonstrated that interactions between N and P can impact algal productivities [5]. It has been noticedd that chlorophyll yield in Japanese lakes was in balance with both total nitrogen and phosphorus concentrations when the ratios of the two nutrients was between 10 and 17 and only on total phosphorus when ratios were >17 [1]. Another study reported that total nitrogen: total phosphorus ratios varied significantly with lake trophic status [6]. The authors of this study found that the total nitrogen: total phosphorus ratios declined in a curvilinear fashion as the amount of total phosphorus increased.

In this context, it is obvious that the phosphorus total content is an important indicator in the establishment of water degree and lake trophic status.

**Total phosphorus concentrations, mg/L**
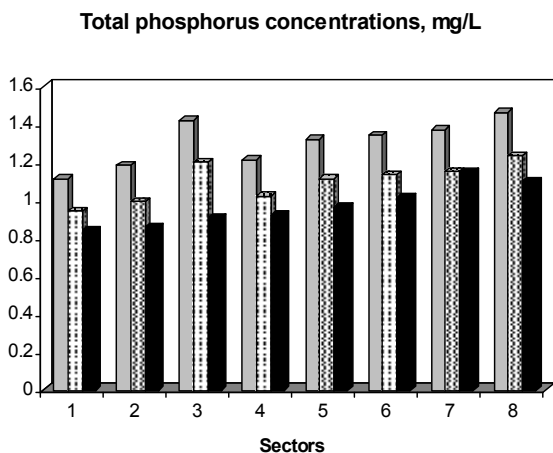


**Fig. 5.** *The gradient of the total phosphorus concentrations*

The results obtained at the analysis of phosphorus content on the water samples from the eight points of sampling, previously established, point out a practical constant increase over the whole flow length (figure 5). This evolution confirms the increase of the pollution degree with carrying phosphorus substances. The advance to the warm seasons of the year results in a decrease of phosphorus content, on an average of about 20%. The recorded dynamics is natural and in good agreement with functioning of microorganisms and phytoplankton.

**Organic phosphorous concentrations, mg/L**
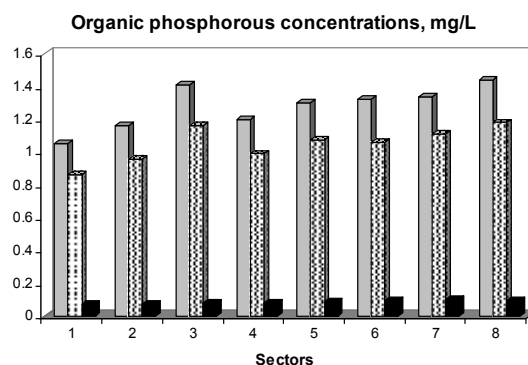


**Fig. 6.** *The variation of the organic phosphorus concentrations*

The cycle of phosphorus in water take place between inorganic and organic species. In spring-summer period the main component of total phosphorus is the *organic phosphorus,* with a contribution on an average of 88-90% (figure 6).

Also, the content of organic phosphorus records during the flow a constant increase, accompanied by a diminishing with an average percent of 9.5% on spring-summer lapse. In the cold periods of the fall the content of organic phosphorus exhibits significant decreases, its contribution being below 8-9 % of total value. In both periods under investigation, the values obtained for the *inorganic phosphorus* were significantly low (table 5). The inorganic phosphorus become the main component of the total phosphorus in fall season.

**Table 5.** *The content of inorganic phosphorus in the Ciric water samples*

| Sectors | Spring March-April 2007 | Sommer May-June 2007 | Fall October-November 2007 |
|---------|------------------------|----------------------|----------------------------|
| | | [mg/L] | |
| 1 | 0.062 | 0.0548 | 0.769 |
| 2 | 0.0108 | 0.0095 | 0.788 |
| 3 | 0.0153 | 0.0134 | 0.832 |
| 4 | 0.0104 | 0.0091 | 0.842 |
| 5 | 0.0124 | 0.0111 | 0.895 |
| 6 | 0.0248 | 0.0218 | 0.912 |
| 7 | 0.025 | 0.0222 | 1.050 |
| 8 | 0.022 | 0.0218 | 1.005 |

The content of the inorganic phosphorus at the sampling points is lower with about 1-2 orders of magnitude and stays almost constant during the whole investigated period (spring-summer). In the third period of sampling the content of inorganic phosphorus increases constantly reaching at the last sampling point a value that is higher with about 30% than the recorded value at the first point. Based on the dynamics of these two biologically limiting nutrients the trophic status of the Ciric lake ecosystem has been evaluated (table 6).

The analyses point out that urgent actions need to be undertaken in order to rehabilitate this lake which rapidly can shifted to a hypertrophic status.

***Table 6.** Evaluation of the trophic status of the Ciric lake*

| Indicator | Spring | | Summer | | Fall | |
|---|---|---|---|---|---|---|
| | Total P | Total N | Total P | Total N | Total P | Total N |
| | [mg/L] | | | | | |
| Dorobant lake | 1.27 Hipertrof | 0.86 Mezotrof - Eutrof | 1.07 Hipertrof | 0.62 Oligotrof – Mezotrof | 0.89 Hipertrof | 2.25 Hipertrof |
| Aroneanu Lake | 1.29 Hipertrof | 0.61 Oligotrof - Mezotrof | 1.08 Hipertrof | 0.41 Oligotrof | 0.97 Hipertrof | 1.6 Eutrof |
| Ciric I lake | 1.36 Hipertrof | 0.885 Mezotrof – Eutrof | 1.14 Hipertrof | 0.57 Oligotrof - Mezotrof | 1.08 Hipertrof | 3.37 Hipertrof |
| Ciric II Lake | 1.42 Hipertrof | 1.15 Mezotrof - Eutrof | 1.19 Hipertrof | 0.75 Mezotrof - Eutrof | 1.12 Hipertrof | 5.02 Hipertrof |

## 5. Conclusions

The results obtained in this study can be viewed as an alarm. Lake management and restoration has an important contribution to positive management of environmental and human health.

Short-term solutions to lake water quality problems based more on political jurisdictions of municipality than sound ecological principles can result in failure.

For the waters of Ciric lake continue to meet both human and ecosystem needs comprehensive integrated management programs must be implemented without delay.

## References

[1]. D. Allan, T. Johengen, E. Rutheford - *Nutrient Loading and its Relevance to the Great Lakes Basin*, University of Michigan, 2002, p. 1-49.

[2]. T. Garmaeva, Lake Baikal - *Model for Sustainable Development of the Teritory*, Lakes reserv.: Research and Management, 6, 2001, p. 253-257.

[3]. A. Newman - *Water Pollution sources stiil significant in urban areas*, Environmental Science and Technology, 29, 1995, p. 114-120.

[4]. R. Quiros, E. Drago - *The environmental state of Argentinian lakes: an overview*, Lake Reserv.: Res. Management, 4, 1999, p. 55-64.

[5]. V. Smith - *The nitrogen and phosphorus dependence on algal biomass: An empirical and theoretical analysis*, Limn. Oceanogr., 27(6), 1982, p. 1101-1112.

[6]. J. Downing, E. MacCauley - *The nitrogen: phosphorus relationships in lakes*, Limn. Oceanogr. 37(5), 1992, p. 936-945.

# EFFECT OF AN OXY-SULPHIDE INOCULANT ENHANCER ON GRAPHITE PARAMETERS IN THE MOULD INOCULATED COMPACTED GRAPHITE CAST IRON

## M. C. FIRICAN*, I. C. STEFAN, I. RIPOȘAN

POLITEHNICA University of Bucharest, 313 Spl. Independentei, RO-060042, Bucharest, Romania
*Corresponding author;
e-mail: firicanmihailciprian@gmail.com

## ABSTRACT

*In compacted/vermicular graphite cast iron production, inoculation is applied to limit the formation of carbides, but usually this treatment also promotes nodular graphite with improved nodularity. The main objective of the present paper is to examine the graphite phase characteristics in these irons, as affected by different in the mould inoculation variants, for resin sand mould castings. Graphite shape factors illustrate the loss of compactness of the graphite particles in the surface layer of the casting and its variation with cooling rate changes, especially with the circularity expression. In the surface layer, up to 0.5 mm from the cast surface, inoculation increased graphite nodularity, with the performance of the inoculant enhancer alloy [OS-IE] treated iron also promoting a high nodularity through the section of casting. A specific effect of inoculation with this alloy is the formation of a high number of small graphite nodules, which is accompanied by higher nodularity and the highest levels for the circularity and sphericity shape factors. Inoculation with the (Ca+OS-IE) dual addition led to the highest compacted/vermicular graphite formation sensitivity, with limited nodular graphite formation.*

KEYWORDS: inoculant, inoculant enhancer, inoculation, compacted graphite cast iron, calcium ferrosilicon, oxide forming elements, graphite, shape factors, nodularity, sulfur, oxygen

## 1. Introduction

Of the present production, iron castings represent more than 70% of all castings worldwide mainly due to the package of physical and mechanical properties associated with competitive costs. In the family of cast irons, compacted/vermicular graphite iron is increasingly attractive for industrial applications. Vermicular or compacted graphite cast iron (C/VGI or CGI) is a type of cast iron in which the graphite is shaped between flake/lamellar and nodular/spheroidal. Compared with flake graphite in grey iron, compacted/vermicular (C/V) graphite is shorter and thicker and shows a curved, more rounded shape intermediate between flake and fully nodular graphite. The name vermicular graphite (VG) relates to the unusual graphite shape, which resembles a worm hence the inference, wormlike graphite. The alternate name, CGI, is associated with a measurement of the graphite shape, the ratio of width

to length, which in CGI is much higher than that of grey iron.

The graphite shapes in CGI consist of vermicular graphite and also some nodular or spheroidal graphite; generally, more than 70% compacted graphite must be present, with the remainder nodular graphite, not flake graphite. Graphite nodularity, usually expressed as a nodular/vermicular graphite ratio (%) is an important control factor for this grade of iron. The presence of lamellar (flake) graphite is prohibited, while the amount of nodular graphite must also be restricted.

Compacted/vermicular graphite cast iron is obtained by a treatment of the base iron in two steps: a compacting or nodulizing first treatment followed by a second graphitizing step using an inoculant, similar to ductile iron production. Elements known for their nodulizing capability, such as magnesium and/or rare earth elements (Ce, La, Pr, Nd, Y) are employed in the first step, while inoculating elements,

such as Ca, Ba, Sr, Ce, La are used in the final treatment.

A residual content of 0.01–0.03% of nodulizing elements is necessary, depending on the presence of anti-nodularizing elements and solidification (cooling) rate, which is influenced by the characteristics of both the castings and mould media. The first treatment must ensure an adequate nodulizing potential to avoid lamellar graphite formation or an excess of nodular graphite, and the role of the second treatment is to avoid carbides forming as well as encourage graphitization. In ductile iron production, inoculation is applied after Mg-treatment to enhance graphite nodularity, which for specific CGI castings could be more than is acceptable.

Several studies proposed and then investigated whether graphite nucleation occurs on sulfide and/or oxide particles, which are formed after the molten iron treatment [1-4]. They found that compounds of magnesium-calcium sulfides act as nucleation sites for graphite particles in irons treated with Mg-bearing ferrosilicon alloys. Consequently, some elements, such as sulphur and oxygen appear to be important to sustain nodular graphite formation.

The main objective of the present paper is to examine the effects of in the mould inoculation of a Mg, RE-MgFeSi treated compacted/vermicular graphite iron, at low anti-nodularizing potential of the base iron. Three inoculant variants were tested: (a) a conventional Ca-FeSi alloy, (b) an oxy-sulphide inoculant enhancer alloy [(OS-IE)] added with a conventional Ca-FeSi alloy, and (c) the OS-IE alloy added as the inoculant treatment.

## 2. Experimental procedure

The base iron was melted in a coreless induction furnace (acid lined, 150 kg, 2400 Hz). The charge mix contained 50 wt.% high purity pig iron and 50 wt.% cast iron scrap with a 520 g graphite powder addition to correct the iron analysis (fig. 1). The thermal regime during the iron melt process was as follows: superheat temperature Ts=1550 ºC; Mg treatment temperature Tm=1530 ºC; pour temperature Tp=1350 ºC.

The base iron was tapped into a tundish cover nodulizing ladle containing FeSiMgRE alloy (table 1). After the nodulizing treatment the melt was poured into a specially designed test mould with a central downsprue feeding Mg-treated iron simultaneously to four separate reaction test chambers: (1) as an un-inoculated reference; (2) 0.1 wt.% Ca bearing FeSi alloy; (3) 0.02 wt.% oxi-sulphide inoculant enhancer; (4) 0.04 wt.% Ca bearing FeSi alloy + 0.015 wt.% [OS-IE]) alloy. Table 1 illustrates the chemical composition of the inoculants used.

$W_3$ chill wedge samples (ASTM A367-85 specification, dimensions 19 x 38 x 100 mm, cooling modulus, CM = 3.5 mm), plate samples (4.5 mm thick) and round bar samples (25 mm diameter) were cast in furan resin sand moulds. A Furan resin (3.0 wt.%) - P-Toluol Sulphonic Acid (PTSA) (6.53 wt.%S content and 1.5 wt.% addition) bonded silica sand (95.5 wt.%) [FRS-PTSA] moulding system was used. No reclaimed moulding material was used and the moulds contained approx. 0.1 wt.%S. In this study, round bar samples were used for structure analysis and thin plate samples for chemical analysis of the final castings.

## 3. Results and discussion

The final chemical composition of the treated irons is slightly hypereutectic, with a carbon equivalent CE = 4.3 – 4.4% (table 2). All the castings contained the nodulizing element Mg at a low level, appropriate for compacted graphite cast iron ($Mg_{res}$ = 0.019 - 0.023%). There is a small difference in the content of trace elements in the heats. The cumulative influence of the pearlite forming elements in the Mg-treated irons (Factor $P_x$) and anti-nodularising elements effect (Factor K) [5] is included in table 2. It could be concluded that the content of anti-nodularising elements in the Mg-treated irons is sufficiently low (K < 0.7). The pearlite factor $P_x$ = 3.9 - 4.9 indicates a medium pearlite forming tendency, for conventional solidification conditions.

Micrographs included in figure 2 illustrate the typical structure of these experimental irons at the same solidification rate 3.96 mm from the surface in a 25 mm round bar. This structure is characteristic for the experimental cast irons chemistry, at around 0.02% $Mg_{res}$.

$$CE = \%C + 0.3(\%Si + \%P) - 0.03\%Mn + 0.4\%S \quad (1)$$

$$P_x = 3.0\ (\%Mn) – 2.65\ (\%Si - 2.0) + 7.75\ (\%Cu) + 90\ (\%Sn) + 357\ (\%Pb) + 333\ (\%Bi) + 20.1\ (\%As) + 9.60\ (\%Cr) + 71.7\ (\%Sb) \quad (2)$$

$$K = 4.4\ (\%Ti) + 2.0\ (\%As) + 2.4\ (\%Sn) + 5.0(\%Sb) + 290(\%Pb) + 370(\%Bi) + 1.6(\%Al) \quad (3)$$

A mixture of compacted and nodular graphite morphologies characterizes these structures, with a relatively high nodularity level (fig. 3). According to figure 3, graphite nodularity is influenced by the applied treatment (un-inoculated and inoculated irons), solidification rate (greater distance from the surface, slower cooling rate) and inoculation choice [Ca-FeSi, OS-IE only or (Ca-FeSi + OS-IE)].
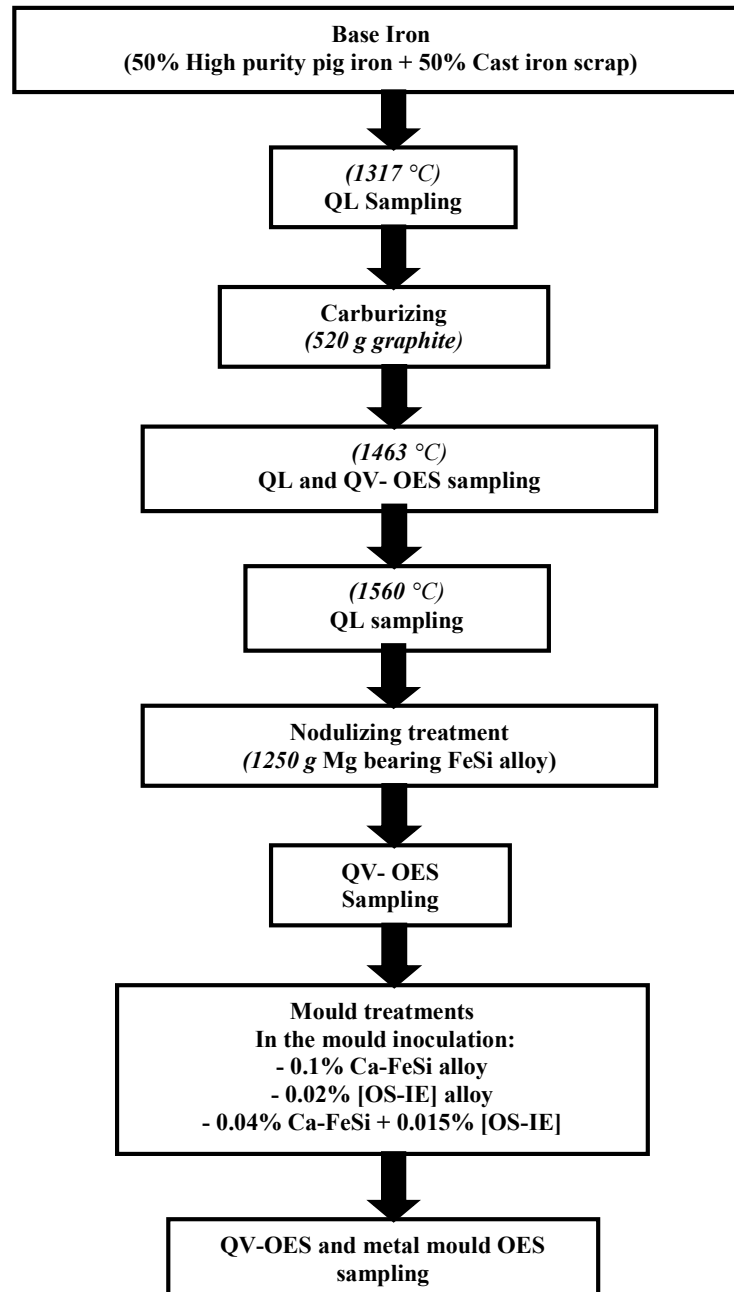
For all of tests, the lowest graphite nodularity (less than 20%) was obtained at the casting surface, despite the highest cooling rate characteristic of this

area, as a result of high heat transfer from the metal to the mould. Generally, a higher solidification cooling rate promotes greater graphite nodularity in Mg-treated irons.

Conversely the same area of casting experiences S-transfer from the mould since P-Toluol Sulphonic Acid (PTSA) influence is at the highest level, which can explain the reduction in graphite nodularity. It is assumed that $SO_2$ will result from the combustion of

PTSA in the resin sand at the casting temperature. $SO_2$ is absorbed at the metal surface, after it has dissociated into atoms. It either diffuses into the molten metal, or will be reduced by iron to form FeS and FeO in solution, which can react with magnesium in the molten iron. As a consequence Mg is partially consumed prior to solidification, and the nodulising potential of the treated iron decreases [6].

**Base Iron**
**(50% High purity pig iron + 50% Cast iron scrap)**

*(1317 °C)*
**QL Sampling**

**Carburizing**
*(520 g graphite)*

*(1463 °C)*
**QL and QV- OES sampling**

*(1560 °C)*
**QL sampling**

**Nodulizing treatment**
*(1250 g Mg bearing FeSi alloy)*

**QV- OES Sampling**

**Mould treatments**
**In the mould inoculation:**
**- 0.1% Ca-FeSi alloy**
**- 0.02% [OS-IE] alloy**
**- 0.04% Ca-FeSi + 0.015% [OS-IE]**

**QV-OES and metal mould OES sampling**

***Fig. 1.*** *Technical schedule [OES/QV - Optical emission spectroscopy; QL - Quick Lab]*

It was found that for the furan resin-PTSA moulding system, sulphur delivered by the mould is an important contributor to graphite degeneration in

the surface layer of Mg treated iron castings. Uncoated FRS-PTSA moulds, which have sulphur in the binder, promoted degenerate graphite in the

surface layer of the test castings, with the thickness of this layer increasing as residual magnesium content decreased: compacted graphite iron is more sensitive to this abnormal surface layer compared to nodular graphite iron, as is a ductile iron with a marginal nodularising potential for similar solidification conditions [7-9]. The lowest nodularity in the surface layer of a casting was obtained in the un-inoculated iron, while inoculation generally increased the graphite nodularity in the experimental conditions in this layer for all the treatment variants. The highest nodularity appears in the iron treated with only the inoculant enhancer alloy [OS-IE], despite a sulphur contribution from this material. This effect is due to the activity of sulphur in the enhancer alloy, which combines with active elements in the melt, promoting the formation of numerous small particles that can act as nucleating agents for graphite.

***Table 1.*** *Chemical composition of the treatment alloys (wt.%)*

| Alloy | Si | Ca | Mg | Al | TRE | Ce | La | Ba | S | O |
|---|---|---|---|---|---|---|---|---|---|---|
| **FeSiMgRE [Nodulizer]** | 44.71 | 1.02 | 5.99 | 0.91 | 0.25 | 0.15 | 0.10 | 0.035 | | |
| **Ca-FeSi [Inoculant]** | 73.80 | 1.02 | | 0.77 | | | | | | |
| **OS-IE [Enhancer]** | 36.90 | 16.29 | 1.96 | 5.74 | | | | | 8.11 | 2.67 |

*TRE-total rare earth elements

***Table 2.*** *Chemical composition of cast irons*

| Inoculation | Chemical Composition [wt.%] | | | | | | | Control Factors | |
|---|---|---|---|---|---|---|---|---|---|
| | C | Si | Mn | P | S | Mg | CE | K | $P_x$ |
| Un-inoculated | 3.59 | 2.49 | 0.43 | 0.040 | 0.023 | 0.020 | 4.42 | 0.645 | 3.879 |
| Ca-FeSi inoculation | 3.58 | 2.48 | 0.41 | 0.058 | 0.029 | 0.019 | 4.42 | 0.551 | 4.416 |
| [OS-IE] inoculation | 3.58 | 2.45 | 0.47 | 0.046 | 0.021 | 0.023 | 4.40 | 0.649 | 4.694 |
| Ca-FeSi + [OS-IE] inoculation | 3.45 | 2.44 | 0.38 | 0.057 | 0.030 | 0.019 | 4.28 | 0.502 | 4.954 |
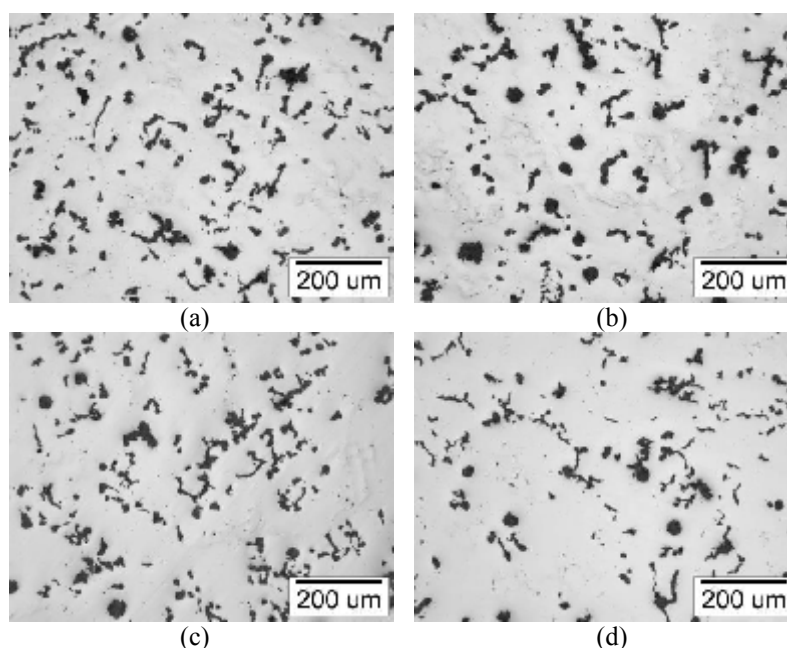


***Fig. 2.*** *Graphite structure at 3.96 mm from the surface [a)-un-inoculated; b) Ca; c) OS-IE; d) Ca+OS-IE; un-etched]*

According to figure 3, the surface layer with lower nodularity thickness is generally no more than 0.5mm. After this, the graphite nodularity is within the 35-50% range, with limited influence from the cooling rate, as defined by distance from the casting surface. Two groups of irons appear to be, concerning the graphite nodularity level: un-inoculated and OS-IE treated irons (40-50%) and Ca and (Ca+OS-IE) treated irons (35-40%), respectively.

Table 3 and figure 4 include the main shape factors used for evaluating the graphite morphology

on a section of the 25 mm diameter round bar samples. The graphite characteristics were evaluated with Automatic Image Analysis [analySIS® FIVE Digital Imaging Solutions software]. Two groups of representative shape factors were considered with higher levels of circularity and sphericity describing more graphite particle compactness, with a value of 1.0 for spherical particles. Circularity and sphericity are different approaches to describe the roundness of a particle. Elongation and aspect ratio at lower levels defined a higher degree of compactness.
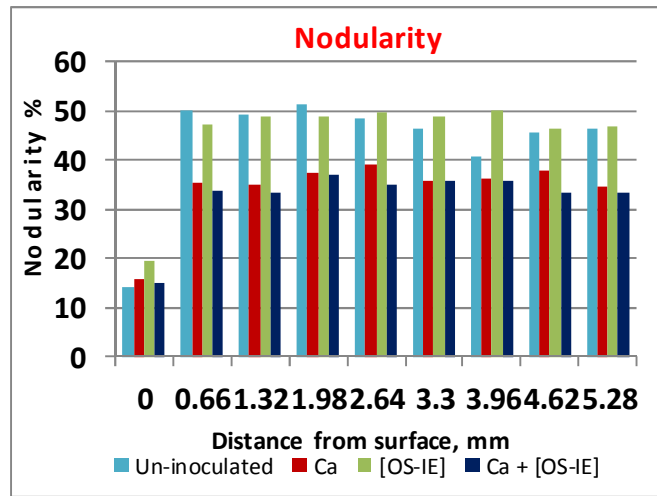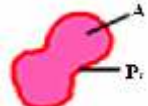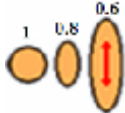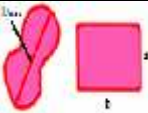


*Fig. 3.* *Graphite nodularity at different distances from the sample surface and different inoculation treatments*

*Table 3.* *The main shape factors used for graphite morphology evaluation*

| No. | Parameter | 2D- Geometrical features | Definition |
|---|---|---|---|
| 1 | Circularity ($F_c$) [$F_c=4\pi A/P_r^2$] $F_c \leq 1$ | | Provides informations about the particle "roundness" by using the area (A) and the real perimeter ($P_r$) of the measured particle |
| 2 | Sphericity ($F_s$) $F_s \leq 1$ | | Describes the spheroidal shape or " roundness" by using the central moments, $\mu_{p,q}$ $\mu_{p,q} = \iint(x-x_c)^p(y-y_c)^q f(x,y)dxdy$ p,q-central moment indices $x_c,y_c$-center of gravity coordinates |
| 3 | Elongation (E) [$E= D_{max}/a$] $E > 1$ | | The ratio of the maximum diameter ($D_{max}$) and the equivalent rectangle shortest side (a) (the rectangular whitch has the same area and perimeter as the particle) |
| 4 | Aspect Ratio [$AR=b/a$] $AR > 1$ | | The maximum ratio of height (b) and width (a) of a rectangular boundary for the measured particle |

Graphite shape factors values confirmed the influence of the casting surface layer at the lower degree of compactness of graphite particles, as all are

different compared to the body of the castings, beyond any influence of the mould (surface *versus* body): $F_c = 0.49 - 0.58 < 0.63 – 0.73$, $F_s = 0.26 – 0.28$

< 0.35 – 0.43, E = 2.4 – 2.7 > 1.7 – 2.2 and AR = 2.0 – 2.2 > 1.6 – 1.8. Considering the graphite shape factors, inoculation appears to have a clear beneficial effect on circularity characterization, with limited benefits for sphericity, but with inconclusive influence regarding the second group of shape factors (elongation, aspect ratio). As distance from the casting surface increases the solidification rate decreases leading to a slow decline of the degree of graphite particles compactness (decreasing $F_c$ and $F_s$ and increasing E and AR shape factors) in the body of the castings. There is limited influence from the inoculation treatment or the inoculant choice. Generally, a small addition of the complex alloy bearing sulfur and oxygen, associated with other active elements, such as calcium, aluminium and magnesium appears to support graphite nucleation with a high degree of compactness. One specific effect of the inoculation with this OS-IE alloy is the formation of a high number of small graphite nodules. A very high nodule count is usually accompanied by more spherical nodules, which explains the high nodularity in this test and the highest levels for circularity and sphericity shape factors.



(a)

(b)

(c)

(d)
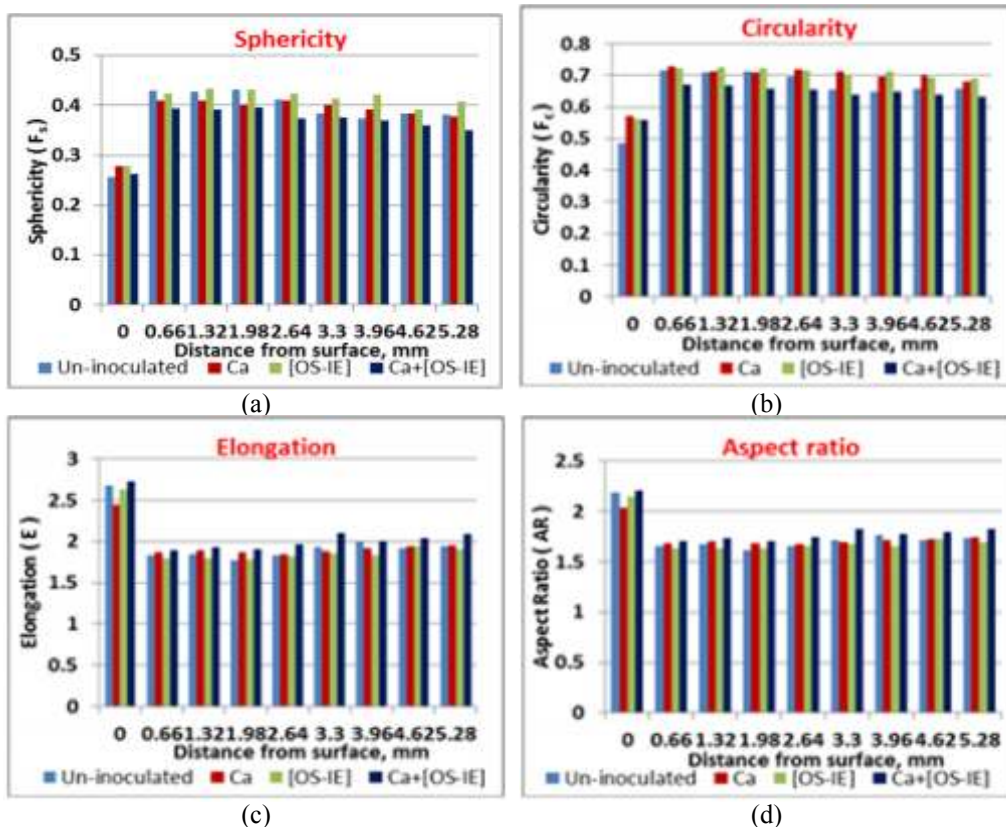
**Fig. 4.** *Shape factors variation for uninoculated and inoculated irons*

In contrast, solidification in these test conditions, using (Ca+OS-IE) inoculation led to the highest compacted/vermicular graphite formation sensitivity, with restricted nodular graphite formation, at under 35% nodular graphite content in this iron.

## 4. Conclusions

*In Mg,RE-FeSi treated, compacted/vermicular graphite cast iron, at 0.019–0.023%$Mg_{res}$, cast in a Furan resin - P-Toluol Sulphonic Acid (PTSA) bonded silica sand [FRS-PTSA] moulds, the graphite phase characteristics are influenced by inoculation, in both the surface layer and in the body of the castings.

*Even with the highest solidification rate at the surface layer the structure has the lowest graphite nodularity (10-20%), due to the mould binder sulfur content, in contrast to 35–50% nodularity in the casting body, for 25 mm round bar sample solidification conditions.

*Graphite shape factors illustrate the loss of compactness of the graphite particles in the surface layer of the casting and how it varies with the cooling rate, especially the circularity factor.

*The inoculation changes have a complex influence on the graphite phase characteristics, in the surface layer versus the casting body, depending on the chosen graphite parameter.

*In the surface layer of the casting, up to 0.5 mm depth, inoculation with only the inoculant enhancer alloy [OS-IE] increased the graphite nodularity, promoting a high nodularity, even through the section of casting.

*A specific effect of inoculation with this alloy [OS-IE] is the formation of a high number of small graphite nodules, which is associated with higher nodularity. This was represented by the highest levels for circularity and sphericity shape factors.

*Inoculation with the (Ca+OS-IE) dual addition led to the highest compacted/vermicular graphite formation sensitivity, with limited nodular graphite formation.

## Acknowledgments

## References

[1]. Chisamera M., Riposan I. - Sulphur Inoculation of Mg-treated Cast Iron - on Efficient Way to Control Graphite Morphology and Nucleation Ability, Fifth International Symposium on the Physical Metallurgy of Cast Iron, Oct. 1994, Nancy, France; Advanced Materials Research, 1997, vol. 4-5, p 293-300.

[2]. Skaland T. - Nucleation Mechanism in Ductile Iron, Proceedings of AFS Conference on Cast Iron Inoculation, Schaumburg, sept. 2005, p.13-30.

[3]. Chisamera M., Riposan I. Barstow M. - The Importance of Sulphur to Control Graphite Nucleation in Cast Iron, AFS Inoculation Conference, April 1998, Chicago, USA, paper no. 3.

[4]. Lalich M. J., Hitchings J. R. - Characterization of Inclusions as Nuclei for Spheroidal Graphite in Ductile Cast Iron, AFS Trans., 1976, vol. 44, p 653-664.

[5]. Thielman T. - Zur Wirkung van Spurenelementen in Gusseisen mit Kugelgraphit, Giessereitechnik, 1970, 1, p. 16-24.

[6]. Xiaogan H., Nodular iron surface deterioration due to PTSA in resin, AFS Trans., 1992, vol. 100, p. 9-15.

[7]. Chisamera M., Riposan I., Ivan N., Stan S. - No-Bake Mould Iron Casting Skin Management – Effect of Magnesium Residual and Mould Coating, Proc. of the 71$^{st}$ World Foundry Congress, May 2014, Bilbao, Spain.

[8]. Riposan I., Chisamera M., Stan S. - Control of Surface Graphite Degeneration in Ductile Iron for Windmill Applications, Int. J. Metalcasting, 2013, 7 (1), p.9-20.

[9]. Ivan N., Chisamera M., Riposan I. - Mg-bearing coating of resin sand – PTSA moulds to control graphite degeneration in the surface layer of ductile iron castings, Mat. Sci. Techn., 2012, 28 (11), p. 1246-1253.

# RESEARCH ON THE WORK PLACE SECURITY AND ENVIRONMENTAL FACTORS AFFECTED BY LATHE WORK

**Georgeta DRAGOMIR, Marian BORDEI,
Ștefan DRAGOMIR**
"Dunarea de Jos" University of Galati, Romania
e-mail: sdragomir@ugal.ro

## ABSTRACT

*Most work place risks are spatially and temporally determined, so a critical early need is to establish the risk of what (is happening) to whom (which part of the environment is affected), where (location) and when (in time).*

*Environmental factors that can be damaged are: soil, water, air, noise, biodiversity, landscape and human settlement.*

*Formulating the problem in clear and unambiguous terms will assist in selecting the level and types of assessment methodology used and will improve, in the context of sustainable development, the risk management decision.*

KEYWORDS: lathe work, place security, environment factors, sustainable development

## 1. Consideration on the work process

Work to the lathe provides machining of ferrous and nonferrous metal elements on normal lathes and special lathes, machinery and equipment of lathe technology. The elements for evaluate the work system are: lathe parts; knife, tools, profiles and devices; electrical outlet; protective equipment: overalls, shoes or boots, helmet, gloves.

The lathe work task mainly has the following components: arrival at work; checking the technical condition of the tools; transport to work of the means of production; process specifications execution.

Work environment usually means to perform activity in cutting processing workshops and reconditioning and repair workshops.

## 2. Identified risk factors

### 2.1. The main risk factors

The main risk factors that characterize the lathe work place (fig. 1) are:
► *Mechanic risk factors:*
F1 - Moving machine parts;
F2 - Catching hand;
F3 - Hanging articles of clothing;
F4 - Rolling parts, materials overthrow tools that are not insured when working at height or below "0";

F5 - Design objects or particles in the air to work with lathe;
F6 - Cutting, stinging contact with hazardous areas.
► *Thermal risks:*
F7 - High temperatures in summer when working outdoors;
F8 - Cold winter when working outdoors.
► *Chemical risk factors:*
F9 -Fine chemical powder.
► *Electric risk factors:*
F10 - Electrocution by indirect contact;
F11 - Electrocution by direct contact;
F12 - Accidental damage to electrical insulation;
F13 - Electrical panels uninsured through their fitting work platform;
F14 - Achieving under voltage the metal surfaces which are accidentally under tension;
F15 - Damage to the circuits binding of the earthing.

### 2.2. Risk factors in the work environment

► *Physical factors:*
F16 - Low temperature in winter and high temperature in summer for the outdoor work;
F17 - Drafts when working outdoors on the ground or at height;

F18 - Low level of lighting to working in closed (confined) spaces;

F19 - Natural disasters: lightning, flood, earthquake.

►*Chemical risk factors:*

F20 - Metal particles;

F21 - Working with the potential explosion hazard (when performing works in areas with high risk of explosion; fuel station).

► *Noise level below the maximum limit but repeated;*

► *Biological factors:*

F22 - Dangerous animals (dogs, rats) and insects (wasps) in different workstations.

► *Physical overload:*

F23 - Physical effort in lifting heavy assemblies;

F24 - Vicious working position;
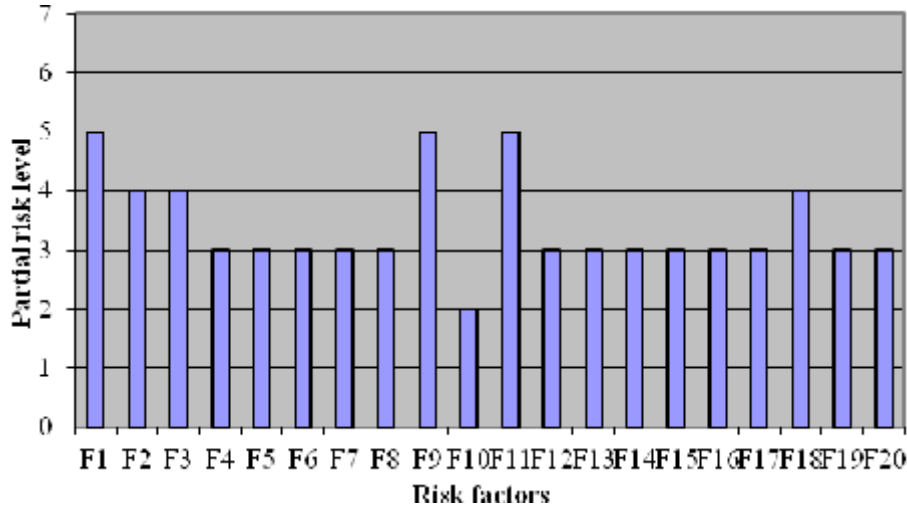
F25 - Permanent demand of attention.



**Fig. 1.** *Partial risk levels of risk factors for the workplace named lathe worker*

## 2.3. Risk factors of the performer

These factors are existing because the worker may do wrong actions during the work process.

►*Wrong actions:*

F26 - Work in an advanced state of fatigue or after administration of drugs;

F27 - Execution of works without being insured (to have a helmet);

F28 - Lowering of the work (in height) in prohibited areas;

F29 - Execution of works in hazardous areas without taking protective measures work;

F30 - Falls from height by stepping into the empty slip, loss of balance;

F31 - Sync mismatch to work in team;

F32 – Fall, flush sliding, stumbling, loss of balance;

F33 - Stopping power tools without providing them in advance (stop task);

F34 - Failure to use personal protective equipment and other protective equipment supplied.

## 3. Calculus of global risk level

In the next part, we well calculate the global risk level in the lathe work place. For that we use the risk factors „ri" and the worthiness note function of periculosity of each risk factor, „Ri", „n" represents the number of risk factors that are taken into account [2]. With next formulas we can calculate the global risk level at the workplace:

$$N_{rr} = \frac{\sum_{i=1}^{n} r_i \times R_i}{\sum_{i=1}^{n} r_i} = \frac{2(6\times6)+3(5\times5)+5(4\times4)+18(3\times3)+4(2\times2)+1(1\times1)}{2\times6+3\times5+5\times4+18\times3+4\times2+1\times1} = 3.69$$

(1)

Overall risk level calculated for work lathe worker equals 3.69, it is a value that falls into the category of jobs with unacceptable risk level, the result is supported by the evaluation form according

which it appears that from the total of 33 risk factors identified in Table 1, and only 10 are ranged as partial risk level 3:

- • 2 factors represent very serious risk consequences 6 - representing 6.1%;
- • 3 risk factors represent serious consequence 5 - representing 9.1%;
- • 5 risk factors represent major consequences 4 - representing 15.15%, the rest falling into the medium risk category.

In Table 1 are shown the worthiness notes for each work place and the safety measures proposed to diminish the work accidents.

**Table 1.** *The worthiness notes for each work place and the safety measures proposed to diminish the work accidents*

| No. | Risk factors | Risk level | Measures proposed<br>Nominating measure | Who is responsible | Time required to fix the problem |
|---|---|---|---|---|---|
| 0 | 1 | 2 | 3 | 4 | 5 |
| 1 | F1 - Moving machine parts | 6 | TECHNICAL MEASURES:<br>- Indication of access roads;<br>ORGANIZATIONAL MEASURES:<br>- Training | Workplace leader | Immediately and permanently |
| 2 | F2 – Impact by means auto, and high, shifting between headquarters and the workplace | 4 | TECHNICAL MEASURES<br>- Indication of access roads<br>ORGANIZATIONAL MEASURES<br>- Training<br>- Proper signage | Workplace leader | Immediately and permanently |
| 3 | F5 - Free fall tools, parts, materials uninsured or improperly handled at higher levels of the job | 4 | TECHNICAL MEASURES<br>- Provision and use of PPE<br>ORGANIZATIONAL MEASURES<br>- Training | Workplace leader | Immediately and permanently |
| 4 | F5 - Design objects or particles in the air to work with lathe | 4 | TECHNICAL MEASURES<br>- Using equipment supplied<br>ORGANIZATIONAL MEASURES<br>- Training | Workplace leader | Immediately and permanently |
| 5 | F21 - Working with the potential explosion hazard (when performing of works in areas with high risk of explosion; fuel station)<br>- Noise level below the maximum limit but repeated | 5 | TECHNICAL MEASURES<br>- Use exhausting installation.<br>ORGANIZATIONAL MEASURES<br>- Training | Workplace leader | Immediately and permanently |
| 6 | F22 - Dangerous animals (dogs, rats) and insects (wasps) in different workstations | 6 | TECHNICAL MEASURES<br>- Checking ground equipment<br>ORGANIZATIONAL MEASURES<br>- Training | Workplace leader | Immediately and permanently |
| 7 | F23 - Physical effort in lifting heavy assemblies | 5 | TECHNICAL MEASURES<br>- Provision and use of PPE (EIP)<br>ORGANIZATIONAL MEASURES<br>- Training | Workplace leader | Immediately and permanently |
| 8 | F26 - Working in an advanced state of fatigue or after administration of drugs | 4 | TECHNICAL MEASURES<br>- Ensure the electrical panels<br>ORGANIZATIONAL MEASURES<br>- Training | Workplace leader | Immediately and permanently |
| 9 | F28 - Lowering of the work (in height) in prohibited areas | 5 | TECHNICAL MEASURES<br>- Prohibition of the use of improvised means for access and working at lower heights<br>ORGANIZATIONAL MEASURES<br>- Training | Workplace leader | Immediately and permanently |
| 10 | F32 – Fall, flush sliding, stumbling, loss of balance | 4 | - Provision and use of PPE (EIP)<br>ORGANIZATIONAL MEASURES<br>- Training | Workplace leader | Immediately and permanently |

We see that there are ten risk factors that are situated at the unacceptable risk level:

F1 - Moving machine parts;

F2 – Impact by means auto, and high, shifting between headquarters and the workplace;

F5 - Free fall tools, parts, materials uninsured or improperly handled at higher levels of job;

F21 - Working with e potential explosion hazard;

F22 - Dangerous animals (dogs, rats) and insects (wasps) in different workstations;

F23 - Physical effort in lifting heavy assemblies;

F26 - Work in an advanced state of fatigue or after administration of drugs;

F28 - Lowering of the work (in height) in prohibited areas;

F32 – Fall, flush sliding, stumbling, loss of balance.

To reduce or eliminate the 10 risk factors (which are situated in the unacceptable level), should be applied the measures presented in the measures file proposed for Turning work.

Regarding the distribution of risk factors on the generating sources, the situation is as follows:

- 45.46% - the means of production factors;
- 18.18% - the working environment factors;
- 18.18% - work task factors;
- 18.18% - factors specific to the performer.

From the analysis of the evaluation form it is found that 66.67% of the identified risk factors may have irreversible consequences for the performer (death or disability).

## 4. Evaluation of environment impact

Assessment of environmental impact shall be carried out using the matrix method (for index of quality) and V. Rojanschi method (calculation of global pollution index) [3].

An assessment of the impact on the environment shall be based on:

- indices of quality on environmental factors (water, air, soil-sub soil, noise, human settlement, biodiversity, landscape) ($I_C$);
- index of global pollution ($I_{PG}$);

Quality of environment factors is falling within the allowed limits of STAS or European Normative Reglementations.

It is estimated effects „project" on the environment based on „factor size" which is to be analyzed taking into account the level of quality indicators that characterize its effects.

The formula of environmental quality index is ($I_c$):

$$I_c = \frac{L_{proiect}}{L_{reglementat}} = k \qquad (2)$$

where: $L_{proiect}$ – project actions;

$L_{reglementat}$ – reglementations of Normative actions;

E – environmental effects.

Interplay between actions project ($L_{project}$) and environmental effects (E) can be highlight by marking the appropriate box of its size estimated by a common system to the whole assembly (with +, - or zero), as follows:

- + positive influence
- 0 zero influence
- – Negative influence

| | |
|---|---|
| $I_c$ = **0** to +1 | - positive influences; Environment is influenced within admissible limits. |
| $I_c$ = **- 1** to **0** | - negative influences; Environment is influenced above admissible limits. |
| $I_c$ = **0** | - Environment is not influenced. |

### 4.1. An assessment of the impact on environmental factors by the quality indexes (Ic)

**Table 2.** *Matrix for impact assessment*

| Environmental actions | Effects on environmental factors | | | |
|---|---|---|---|---|
| | Air | Water | Soil | Noises |
| *Air* | - | + | + | 0 |
| *Water* | 0 | - | + | 0 |
| *Soil* | + | + | - | 0 |
| *Landscape* | 0 | 0 | 0 | 0 |
| *Noises* | 0 | 0 | + | - |
| *Human settlement* | 0 | 0 | 0 | 0 |
| ***Effects E*** | **0** | **+1** | **+2** | **-1** |

The values of Effects (E) are: For air, E =0; For water, E =+1; For soil, E=+2; For noises, E=-1.

### 4.2. Assessment of quality index values

This assessment is based on:

- Quality index values ($I_c$) for each environmental factors;
- Worthiness note that corresponds to $I_C$ values like in Table 3.

**Table 3.**

| Worthiness note | $I_C$ value | Environmental effects |
|---|---|---|
| **10** | **$I_c$ = 0** | Environment is not affected by the developed activity. |
| **9** | **$I_c$ = 0.0 ÷ 0.25** | Environment is affected within admissible limits. Level 1. Positive effects. |
| **8** | **$I_c$ = 0.25 ÷ 0.50** | Environment is affected within admissible limits. Level 2. Positive effects. |

| Worthiness note | IC value | Environmental effects |
|---|---|---|
| 7 | $I_c = 0.50 \div 1.00$ | Environment is affected within admissible limits. Level 3. Positive effects. |
| 6 | $I_c = -1.0$ | Environment is affected above admissible limits. Level 1. Negative effects |
| 5 | $I_c = -1.0 \div -0.5$ | Environment is affected above admissible limits. Level 2. Negative effects |
| 4 | $I_c = -0.5 \div -0.25$ | Environmental is affected above admissible limits. Level 3. Negative effects |
| 3 | $I_c = -0.25 \div -0.025$ | Environment is degraded, level 1. The effects are harmful in case of **long** periods of exposure. |
| 2 | $I_c = -0.025 \div -0.0025$ | The environment is degraded, level 2. The effects are harmful in case of **medium** periods of exposure. |
| 1 | $I_c = $ under $-0.0025$ | The environment is degraded, level 3. The effects are harmful in case of **short** periods of exposure |

$$\mathbf{I_{PG}} = S_i/S_r$$

$$\boldsymbol{I_{PG} = 1}, \textit{ no pollution existence}$$

### 4.3. Quality scale by global polluted index

In the Table 4 in function of $I_{PG}$ value:

**Table 4**

| $I_{PG} = 1$ | - Environment is not affected by human activity |
|---|---|
| $I_{PG} = 1...2$ | - Environment is affected within admissible limits |
| $I_{PG} = 2...3$ | - Environment is affected and there is a discomfort for life forms. |
| $I_{PG} = 3...4$ | - Environment is affected and there are troubles for life forms. |
| $I_{PG} = 4...6$ | - Environment is severely affected and there are multiple dangers for life forms. |
| $I_{PG} = 6$ | - Environment is degraded, unsuitable for life forms. |

### 4.4. The calculus of global pollution index ($I_{PG}$)

It is considered a number of four environmental factors affected by pollution risk such as: air, water, soil-subsoil, noises.

Global Pollution Index $I_{PG} = S_i/S_r$;

$S_i$ value (ideal state) – resulting geometrical figure has the surface:

$$S_i = 200 \text{ cm}^2$$

$S_r$ value (real state).

It was built by pooling related points values Nb (note worthiness) for each environmental factor taken into account.

$N_b$ value shall be obtained for each environmental factor scale of worthiness as a function of the value of the pollution index:

$N_b$ for AIR:
$\qquad I_c = -1.0 \, ð \qquad N_{bair} = 7$

$N_b$ for WATER:
$\qquad I_c = 0.25 \, ð \qquad N_{bwater} = 8$

$N_b$ for SOIL:
$\qquad I_c = -1.0 \, ð \qquad N_{bsoil} = 9$

$N_b$ for NOISES ($N_{bnoises}$):
$\qquad I_c = 0.5 \qquad N_{bnoises} = 5$

Surface Sr: $S_r = 101.46^2$

$$I_{PG} = \frac{S_i}{S_r} = \frac{200 \ cm^2}{101.46 \ cm^2} = 1.97$$

The index of global pollution value is:
$I_{PG} = 1.79$.

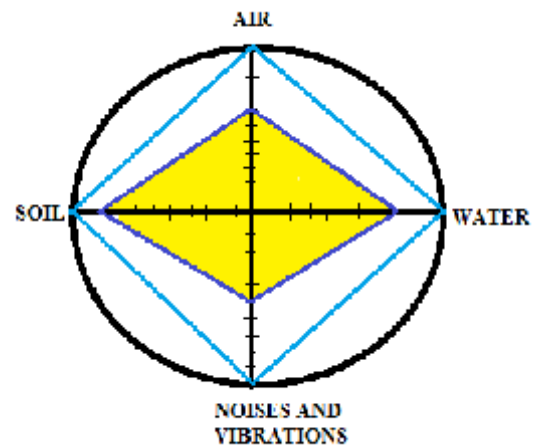The graphical representation of the Index of global pollution is shown in Figure 2.



**Fig. 2.** *Graphical representation of the Index of global pollution*

**Index of global pollution value is**:

$I_{PG}$ = **1.97** -> This value of global pollution index show us that environment is affected within admissible limits.

## 5. Conclusions

In practice, the risk factors will usually accompany development of the conceptual model. Screening can be used to determine which risks should be investigated in greater detail using techniques suitable to the nature of the risk and to the quality of the evidence.

If effective, screening should also identify those features that will not receive further analysis. Prioritization allows for the efficient allocation of resources. Justifying and recording the accompanying rationale for screening risks are valuable [4].

At this stage, risk assessors may develop an early view as to whether they have sufficient data to support a quantitative assessment of the risk if this is deemed necessary, or whether additional data and evidence to support such an assessment might be required. Quantitative risk analysis (QRA) is an expert discipline, expensive to undertake, and requires substantive data and analysis. This may include formal mathematical modeling. Not all risks will require QRA however, either because they are deemed to be insignificant on the basis of the evidence already assembled, or because the risk manager is already confident about their significance and can progress to deciding how to manage the risk.

Risk screening is useful, therefore, for highlighting those risks where uncertainty could affect the management decision and its success in the entrepreneurial system. Such risks may need to be analyzed in greater detail with more sophisticated methods.

## References

**[1]. Costel C. Negrei -** *Bazele economiei riscului de mediu*, EDP, 2007.
**[2]. Freeman M. -** *The Benefit of Environmental Improvements*, John Hopkins University press, 2009.
**[3]. Vladimir Rojanski, Florina Bran -** *Elemente de economia si managementul mediului*, Editura Economica, 2004.
**[4]. Bouder F., Slavin D., Lofstedt R., Lofstedt R. E. -** *The Tolerability of Risk – A New Framework for Risk Management*, London: Earthscan publishing, 2007.

# THE EVOLUTION OF THE CHARACTERISTICS OF MECHANICAL RESISTANCE FOR THE NITRO-CARBURIZED TREATED STEEL, AFTER THERMO-MAGNETIC TREATMENT

**Carmen Penelopi PAPADATU**

"Dunarea de Jos" University of Galati, Romania
e-mail: cpapadatu@ugal.ro

## ABSTRACT

*The aim of the research was to study the evolution of the characteristics of mechanical resistance for one type of steel. The material was subjected to the thermo-chemical (nitro-carburized treatment in plasma) treatment applied after thermo-magnetic treatments. The structural and diffractometric aspects of the superficial layers of the steel are studied after the wear process, using an Amsler type machine, taking two sliding degrees at different contact pressures and testing in time. The tests were done to detect the sustainability to the material, the evolution of the superficial layer characteristics through different tests and to establish the influence of these thermo-magnetic treatments regimes.*

*The magnetic field modifies the grain size in the material structure. It was obtained a small grain size in the middle of the sample and the orientation of these grains is in the same direction with the lines of the magnetic field.*

*It was made a balance sheet between classic treatment and unconventional (thermo-magnetic) treatment.*

KEYWORDS: durability, characteristics of mechanical resistance, thermo-magnetic treatments, thermo-chemical treatment, hardness, wear process

## 1. Introduction

The study of the contact aspects between machine elements is essential due to the fact that more than 60% of provided energy is lost by friction resulting from the relative movements between the elements.

The conventional machining methods such as turning and milling leave inherent irregularities on the surface and it becomes necessary to very often resort to a series of finish operations with high costs.

In last 20 years, the technical progress made it possible to develop the use of very hard materials in several fields like manufacturing parts for the car industry, the railroad coaches, the nuclear power, for the aeronautics and for the mechanical industries. In this paper, it was study the evolution of the superficial layer for an un-conventional treated steel, during the wear tests.

The superficial layer is defined according to the type of interaction between the external action and materials.

In figure 1 was presented one of the first model of the superficial layer [2, 4, 5, 15].
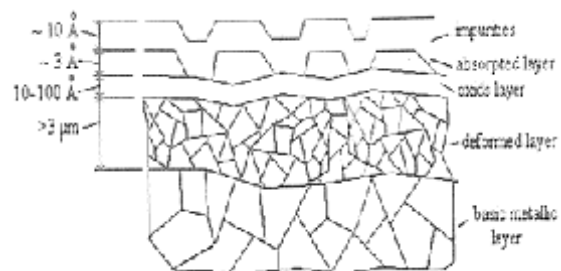


**Fig. 1**. *One model for the superficial layer (J. Caubet)*

Introducing a surface treatment as nitro-carburized process with plasma (ionic) nitro-carburized, the wear resistance increases and the resistance of corrosion increase too.

The diffusion process and the interaction of the nitrogen and carbon with the basic material lead to structural constituents whose nature determines a major hardness of the nitro-carburized layer.

Plasma nitriding/nitro-carburizing modify the strain limit, and the fatigue strength of the metals being treated.

For instance, mechanical properties of austenitic stainless steel like wear process can be significantly reduced and the hardness of tool steels can be double on the surface [1-3, 5, 14, 15].

## 2. Experimental researches

For experiments it was used 38MoCrAl09 steel grade samples. The material considered in this study is a steel of standard quality known as SAE 4038.

The material was subjected to the plasma nitro-carburizing treatment regime, after thermo-magnetic treatment regimes. The classic treatment, without magnetic field applied, was considered too. It was necessary to consider the classic treatment regimes to make the balance-sheet between the classic regimes and the un-conventional regimes.

Wear tests are designed to estimate the material resistance. It was used an Amsler type machine, taking two sliding degrees at different contact pressures and testing time (see figure 3).

The tests were done to detect the evolution of the superficial layer through different tests. It was established the influence of the tribological factors (operating parameters) on the superficial layers.

The chemical analysis obtained by atomic absorption primarily revealed a basic composition presented in Table 1. The steel analyzed reach a max score 4.5 from inclusions and a fine grain (score 8-9).

Table 2 presents the standard mechanical characteristics of the steel 38MoCrAl09 (SAE 4038) [2, 4], corresponding to The Society of Automotive Engineers (SAE) and The American Iron and Steel Institute (AISI).

*Table 1. Chemical composition of the materials [6, 8]*

| Steel grade | C | Mn | Si | P | S | Cr | Cu | Mo | Al |
|---|---|---|---|---|---|---|---|---|---|
| | [%] | | | | | | | | |
| 38MoCrAl09 | 0.38 | 0.50 | 0.25 | 0.026 | 0.020 | 1.38 | 0.058 | 0.17 | 1.18 |

*Table 2. Mechanical characteristics of the steel [6, 8]*

| Steel grade | $Rp_{0,2}$ | $R_m$ | $A_5$ | Z | $KCU_{300/2}$ | $KCU_{300/5}$ | HB (State of annealing) |
|---|---|---|---|---|---|---|---|
| | [daN/mm²] | | [%] | | [daJ/cm²] | | [daN/mm²] |
| 38MoCrAl09 AISI(SAE) 4038 | 85 | 100 | 15 | 50 | 9 | 6 | 229 |

Were applied the following treatment regimes:

a) t1 = martensitic hardening process at 920 °C and high recovery at 620 °C → classic treatment (Magnetic field intensity is H =0 A/m);

b) t3 = quenching (hardening) (920 °C) and high tempering (620 °C) applied to steel 38MoCrAl09, cooling being performed in alternative current (a.c.) magnetic field (H = 1300 A/m);

c) t4 = quenching (920 °C) and high tempering (620 °C), cooling being performed in d.c. (direct current) magnetic field (H = 1300 A/m).

The samples of the steel suffered a Martensitic hardening process at 920 °C and high recovery at 620°C (classic improvement treatment which was noted with "t1") followed by nitro-carburizing process at 530 °C. It was noted T12=T1' = t1 + ionic nitro-carburizing (plasma nitro-carburizing) at 530°C.

T13 = T3' = t3 + ionic nitro-carburizing (plasma nitro-carburizing) at 530 °C.

T14 = T4' = t4 + ionic nitro-carburizing (plasma nitro-carburizing) at 530 °C.

The treated samples were used for wear tests on Amsler machine (see figure 3) and the diffractometric analysis were performed by means of a Dron 3. It were determined the durability of the rollers and the surface structure evolution for different parameters of testing regimes.

The other factors which influence the wearing process are: the contact geometry of the friction couple (roller on roller, roller on ring etc.), the technological parameters (surface quality, heat treatments etc.) and the exploitation conditions (the thermal solicitation, for example).

Wear tests were carried out on an Amsler machine (see figure 3), using several couples of rollers (see figure 2), each couple corresponding to different sliding degrees ξ, defined as:

$$\xi = [ (v_1 - v_2) / v_1 ] \, 100 \, [\%] \qquad (1)$$

where $v_1$ and $v_2$ are the peripheral velocities of the rollers in contact, each one having their specific peripheral velocity due to a particular combination of angular speeds ($n_1$, $n_2$) and diameter sizes ($d_1$, $d_2$).

Index 1 or 2 are added for the roller 1 or 2, respectively, both of the same tested friction couple. For instance, ξ = *10%* is obtained for a pair of tested rollers having $d_1$ = 40 mm, $n_1$ = 180 rpm and $d_2$ = 40 mm, $n_2$ = 162 rpm; ξ = *18%* is obtained for a pair of tested rollers having $d_1$ = 44 mm, $n_1$ = 180 rpm and $d_2$ = 40 mm, $n_2$ = 162 rpm; the level of the stress is corresponding to a specific load of 150 daN (as normal load is Q = 1.500 N) and the contact between roller is b = 10 mm [2, 4, 6, 8].

Magnetostriction may cause local plastic deformations, thus determining a cold hardening of the residual austenite. Furthermore, this implies higher material hardness and for many applications good endurance characteristics (see Figure 4).

Introducing a thermo-chemical treatment as nitro-carburizing process with plasma (ionic nitro-carburizing), the wear resistance increase and the resistance of corrosion, increase too.



***Fig. 2.*** *Couples of rollers corresponding to different sliding degrees ξ* [6, 8]

In figure 3 was presented the Amsler machine for wear tests.



***Fig. 3.*** *Wear tests were carried out on an Amsler machine* [6, 8]

## 3. Experimental results

In figure 4, was presented the evolution of the hardness number function by the magnetic field regimes applied. The specific regime for optimal hardness was considered the un-conventional treatment.
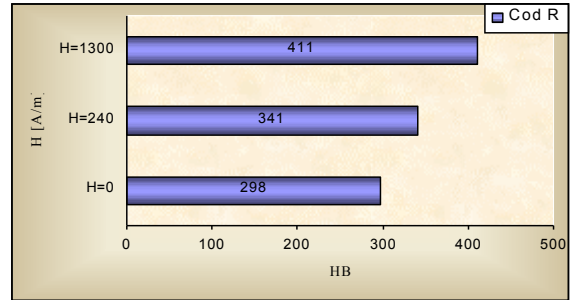


***Fig. 4.*** *The influence of the magnetic field regimes on the hardness value, for code R samples (38MoCrAl09)* [6, 8]

Plasma nitro-carburized layers had a different evolution during wear process.

In table 3 are presented: characteristics, symbols, mathematical relations, which were used during the study of the superficial layers. It were tested the tribological evolution corresponding to wear process (damp wear case).

Using an Amsler machine, it were obtained the following results:

***Table 3.*** *Characteristics, symbols, mathematical relations used during the study of superficial layers tribological evolution* [2, 13]

| Characteristics | Symbol | u.m. | Relations |
|---|---|---|---|
| *The diameters of the rollers* | $d_1, d_2$ | *Mm* | - |
| *The width of the rollers (dimension of the contact)* | *B* | *Mm* | - |
| *Longitudinal Elasticity Module (the equivalent size)* | *E* | *MPa* $(N/mm^2)$ | $E = 2E_1E_2 / (E_1 + E_2)$ |
| *Speed of the rollers* | $n_1, n_2$ | *Rot./min.* | - |
| *Specific glide* | *ξ* | *%* | $\xi = 2 (1 - k\, d_2 / d_1) / (1 + k\, d_2/d_1)\ 100\%$ |
| *Task loading (the force applied)* | $Q_i$ | *N (daN)* | - |
| *The radius of curvature equivalent* | *P* | - | $\rho = d_1d_2 / 2(d_1+d_2)$ |
| *Hertsiana maximum pressure* | $p_m$ | - | $P_m = 0.418 (QE / b\rho)^{-2}$ |
| *Testing time* | *T* | *s* | - |
| *Moment of friction* | $M_f$ | *N mm* | *Will be measured* |
| *Coefficient of friction* | *M* | - | $\mu = 2M_f / d_1Q$ |
| *Length of friction* | $L_f$ | *mm* | $L_f = \pi d_1 n_1 t / 60$ |
| *The used layer depth* | $U_h$ | *mm* | *Will be measured* |
| *The wear strenght (intensity of the wear)* | $I_u$ | - | $I_u = U_h / L_f$ |
| *Wear class* | | - | *See table 4* |

In Figure 5, was presented the influence of the thermo-magnetic treatment regimes applied before of the plasma nitro-carburizing on the used layer depth evolution (Uh), during wear tests, for task loading Q = 150 daN. In Figure 6 was presented the influence of thermo-magnetic treatment regimes applied before of

the plasma nitro-carburizing on the mass loss evolution, during wear tests, for task loading Q=150

daN ($\xi$ = 10%) (conducting roller).
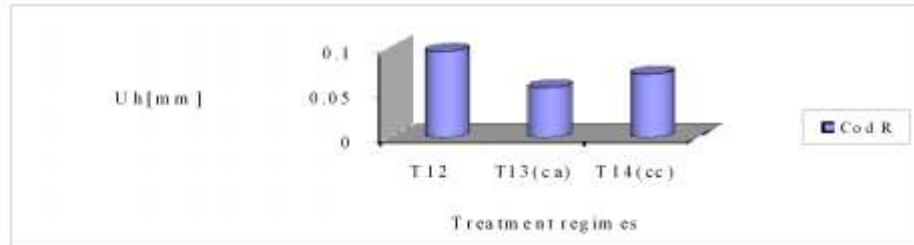


**Fig. 5.** *The influence of the un-conventional treatment on the used layer depth (Uh), during the wear tests (Q= 150 daN)*
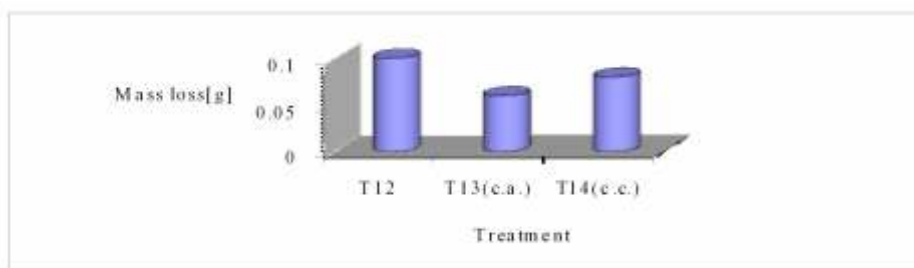


**Fig. 6.** *The influence of the un-conventional treatment on the Mass loss [Δm] evolution, during the wear process*

The cumulated metal weight loss represented by the value of *Δm* was evaluated using the following expression:

$$\Delta m_i = (m_{i-1} - m_i) + \Delta m_{i-1} \qquad (2)$$

where *Δmi* characterizes the wear which results from the contact between the rollers in contact. Wear tests are carried out on a basis of 60 min. duration, three times.

In Figures 7, 8, 9 are presented the superficial layers un-conventional treated, before the wear tests [6, 8, 12].



**Fig. 8**. *Superficial layer thickness before wear tests, for of T13' treatment regime (x100) (with a.c. magnetic field regime)*



**Fig. 7**. *Superficial layer thickness before wear tests, in the case of T12 treatment regime (x100). Nital attack 2%*



**Fig. 9.** *Superficial layer thickness before wear tests, for T14 treatment regime (x100) (with d.c. magnetic field regime)*

# 4. Conclusions

The positive influence of the thermo-magnetic treatment on the surface layer treated thermo-chemically resulted in a higher hardness [4].

The wear resistance increase and the depth of the used layer decrease [5, 7] by approx. 50%. In the case of alternative current (a.c.) or direct continuous (d.c.) magnetic field applied to the steels (T13, T14), it were observed a higher initial quantity of martensite and a higher quantity of carbo-nitrurs, comparing with the classic treatment.

During the wear process, the martensite quantity increase and the carburs quantity decrease very rapidly. Mass loss ($\Delta mi$) had a maximum value in the classic treatment case and it had a minimum value in the case of a.c. magnetic field applied.

# References

[1]. Berkowitz, A. E., s. a. - *Magnetism and Metallurgy*, Academic Press, New York and London, 1969.

[2]. Gheorghies C., Papadatu C. P. - Stefanescu I., *Study on the model of behaviour of some non-conventional treated steels, during friction process*, CENTIMFE, Marinha Grande, Portugal, 2004,

[3]. Gheorghies C. - *Modele 2D ale stratului superficial al materialelor metalice*, Buletinul AGIR, nr. 3/2008, Bucuresti.

[4]. Bozorth R. M. - *Feromagnetism*, New York, Van Nastrand, Co. Inc., 1951.

[5]. Cedighian S. - *Materiale magnetice*, Editura Tehnica, Bucuresti, 1974.

[6]. Papadatu C. P. - *Cercetări privind ameliorarea proprietăţilor şi creşterea fiabilităţii unor oţeluri folosite în construcţia utilajelor metalurgice*, Ph.D. Thesis, Galaţi, 2005.

[7]. Popescu N., s. a. - *Tratamente termice neconvenţionale*, Editura Tehnice, Bucureşti, 1990, p. 105-117.

[8]. Papadatu C. P. - *Posibilitati de imbunatatire a calitatii unor oteluri utilizate in industria metalurgica*, Editura Fundatiei Universitare "Dunarea de Jos", 2007, ISBN 978-973-627-371-1, Galati.

[9]. Stefanescu I. - *Contribuţii la studiul influenţei tratamentelor termomagnetice asupra unor caracteristici mecanice ale oţelurilor de rulmenţi RUL1*, 1981, Suceava.

[10]. Vonsovschi S. V. - *Teoria modernă a magnetismului*, Editura Tehnica, Bucureşti, 1956.

[11]. Papadatu C. P., Stefanescu I. - *Experimental study on the behaviour of some non-conventional treated steels during friction process (I)*, 2005, Tanger, spol.s.r.o., Ostrava.

[12]. Papadatu C. P. - *The possibility to increase the durability of the steels overlapping a magnetic field on the convention al heat treatment before thermo-chemical treatment*, Annals of "Dunarea de Jos" University of Galati, Fascicle II, Year III, (XXXIV), 2011, p. 175-182.

[13]. Stefanescu I. - *Incercari tribologice. Teste de uzura*, Indrumar de laborator, Galati, Universitatea "Dunarea de Jos", 2004.

[14]. Papadatu C. P., Vasilescu E. - *Some Aspects Regarding the Influence of the Tribologycal Factors on the Superficial Layers of Treated Steels with Plasma Nitriding*, The Annals of "Dunarea de Jos" University of Galati, Fascicle IX, Metallurgy and Materials Science, No. 4, 2012, p. 88-94, ISSN 1453-083X.

[15]. Levcovici S., s. a. - *Ingineria suprafetelor*, Note de curs, 2006.

# CORRELATION BETWEEN THE PROPERTIES OF OLD SLAGS AND THE RECYCLING SOLUTIONS

**Anisoara CIOCAN, Florentina POTECAȘU,
Tamara RADU**

"Dunarea de Jos" University of Galati, Romania
e-mail: aciocan@ugal.ro

## ABSTRACT

*The blast furnace and basic oxygen furnace route of steel making (from iron ores and coke to steel) or the so called integrated steel production generates simultaneously solid waste products. The slag is predominant, consisting of blast furnace (BF) slag and basic oxygen furnace (BOF) slag. The major share of this has been stored with no control near industrial area forming a metallurgical waste dump. For solving the problems of metallurgical residues and wastes stored in the old dump, the authority develops an appropriate environment policy for a proper management. The landfilled slag is exploited under supervision. The paper presents the sustainable recycling solutions applied in correlation with the properties of old slags. The performance of recycling solutions for each slag type is discussed according to the chemical composition and structure. Specific cooling conditions (as well as the chemical composition) of slag dumped under the action of variable weather conditions are analysed.*

KEYWORDS: slag, dump, properties, recycling solutions

## 1. Introduction

The slag is the predominant co-product of the iron and steel making industry. An integrated steel mill plant generates different types of slag resulting from multiple sources/sectors. Iron and steelmaking slags (ferrous slags) are the most important. Additional slag types (e.g., de-sulphurisation slag of hot metal, ladle furnace or secondary steel making) are formed during diverse supplementary metallurgical processes (Figure 1).

The slags can be reutilized in various applications such as construction or agriculture. Also they come as valuable secondary raw for own sectors of integrated steel plants for internal recycling and for other users. EUROSLAG through its members (European steelworks and processing companies) has reported for 2010 a production of 45.3 million tons of ferrous slag (23.5 million tons of blast furnace slag and 21.8 million tons of steel slag). The steel slag produced in 2010 consisted of 48% BOF slag, 31% EAF slag (carbon steel), 13% secondary steel slag, 8% EAF slag (high alloy steel) and it was used in diverse application (Figure 2).
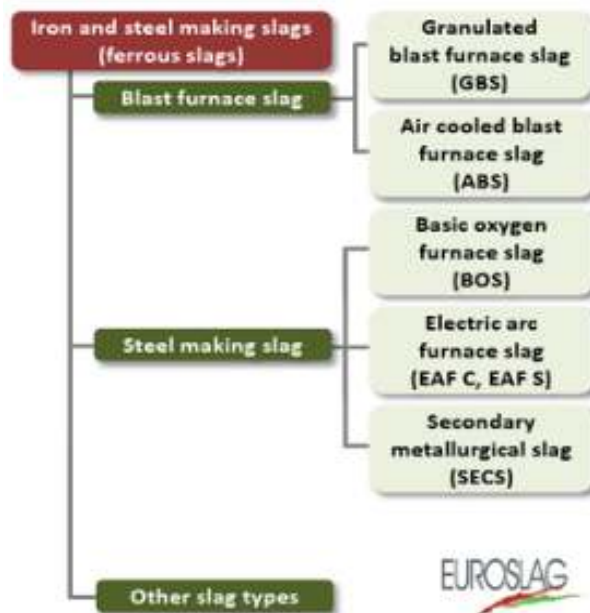


**Fig. 1.** *Slag families identified in Europe today*
(Source: Euroslag.com)

a.



b.
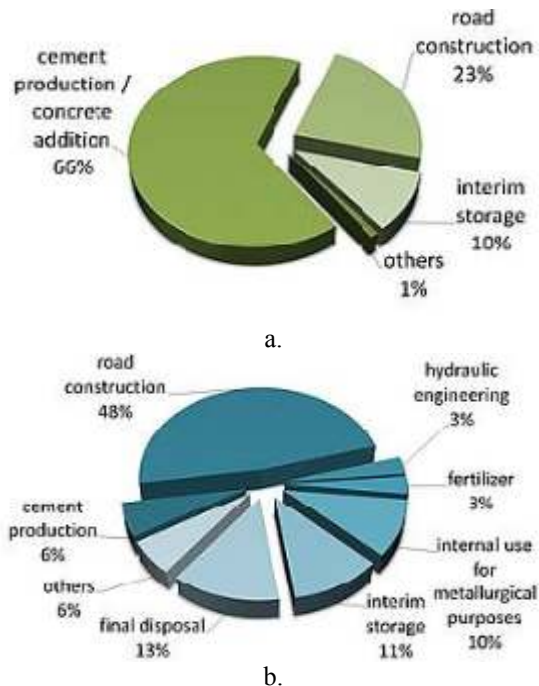
**Fig. 2.** *Use of ferrous metallurgical slag by EUROSLAG members in 2010 (Source: Euroslag.com): a. Blast furnace slag (Data from: A, B, FIN, F, D, I, L, PL, E, SK, S, NL, UK), b. Steel slag (Data from: A, B, DK, FIN, F, D, GR, I, L, PL, RO, E, SK, SLO, S, NL, UK)*

## 2. Research and discussions

### 2.1. Description of dump and of slags stored

The metallurgical plant of Galati was founded in 1961. It is located in Smârdan industrial park, occupying an area of 1.594 ha, at 3 km west of Galati. Here the steel is produced via the integrated route that uses a blast furnace to produce molten pig iron from iron ore, coke, and limestone. This pig iron is subsequently processed in a basic oxygen furnace to produce molten steel. Also for many years functioned within the plant an electric arc furnace sector where the steel was obtained exclusively by melting of steel scrap. In 1966, the plant started the production with one sintering plant, one blast furnace (1.700 cubic meters) and one steel melting shop [1]. On July 24, 2001, the government signed a privatization contract with LNM Holdings, the fourth largest world steel producer at the time [2]. The integrated steel mill plant has been acquired by ArcelorMitall Company. This was the largest steel producer of Romania, and the second largest in Central and Eastern Europe (Figure 3). The metallurgical plant has an estimated annual production capacity of 10 millions tons. After

1989 the production level was decreased to roughly half, from 8.4 to 4.5 ktones in 2003 [3]. Today it operates with a capacity of 5.5 million tons per year.



**Fig. 3.** *View of the integrated steel mill plant of Galati* (Wikipedia.org)

The blast furnace and basic oxygen furnace route of steel making (from iron ores and coke to steel) or the so called integrated steel production generates simultaneously solid waste products. Thus an average of about 400 kg of solid by-products is generated in the steel industry per ton of crude steel. The major share of this (70-80%) consists of blast furnace (BF) slag and basic oxygen furnace (BOF) slag [4].

The major solid wastes of the steel plant have been dumped. So since 1968, near the industrial area and Galati city, a metallurgical tailing dump has been formed from slag, used refractory materials, dusts, sludges and other mass waste (Figure 4).
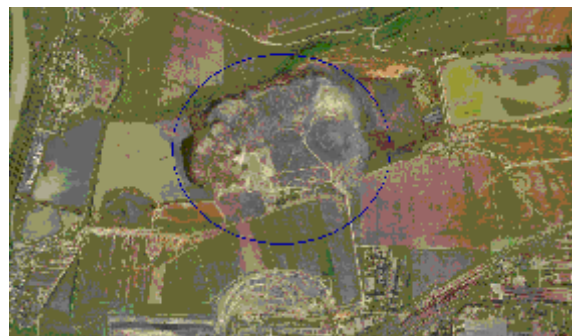


**Fig. 4.** *Image from satellite of landfill with location of the metallurgical wastes dump* (Google earth)

In 2002 the site had an area of 100 ha and heights ranging from 25 to 60 m [1]. This is currently called "slag dump" because the slag is the main metallurgical waste landfilled in cone-shaped heaps (Figure 5). Between 1968 and 2006 the slag dump has been landfilled with about 36.50 mil tons of blast furnace slag and approx. 14.50 mil.t of steel slag [5].

The wastes dumped are an ecological hazard. These are a permanent source of pollution to the environment and people's health.



**Fig. 5**. *Huge piles of slag dump* [5]

The high cost of slag disposal, beside their negative impact on environment and the lack of natural aggregate resources, led to the reutilization of steel slag in various applications. According to the environmental Romanian national regulations (harmonized with the European legislation) was imposed a new approach for solving the problems of metallurgical residues and wastes: those stored in the old dump and the newly ones generated by the activity of the integrated steel mill plant. In 2009 the wastes storage in the historical dump was stopped completely. Also the authority develops an appropriate environment policy for a proper management, both the slags collected on dumps and the slags generated by ongoing production processes. Principally, there have been applied modern solutions to their minimizing at source. On the other hand, the wastes can be considered as a reservoir of valuable materials and consequently they must be valorised. So, by using the attractive solutions, there can be reduced and eventually eliminated the disposed wastes and thereby the minimizing of related environmental pollution. The saving of natural resources and energy is possible.

Considering the specific quantity produced for BF slag (ranged from 175–350 kg/t hot metal) and BOF slag (between 120 and 160 kg/t liquid steel) [6, 7], between 1968-2006 in the old dump of Galati have been deposited about 36.50 mil. tons of BF slag and approx. 14.50 mil. tons of steel slag [5]. Many efficient solutions to convert the metallurgical slag waste in a recyclable material have been applied. So, the slags from dump has lately been exploited and valorised. Despite the efforts there are still certain amounts of slags landfilled in old dump. Lately the Romanian authorities have intensified the efforts to eliminate from the historical dump the residual mill wastes located near Galati town. First, they strive to use slag in areas where they have demonstrated skills to use it. Secondly, they seek new solutions for its recycling. When adopting recycling, solutions must be correlated the properties of different types of ferrous slag exploited from dump with the technical requirements for the applying domain proposed.

## 2.2. Correlation between properties of ferrous slags and recycling solutions

The BF slag and BOF slag had some major differences in their chemical composition. The chemical composition and mineralogy determine the properties and the performance of recycling solutions for each slag type. In point of structure, all slags are unstable materials, subjected to changes under the action of variable weather conditions (temperature variations that determine the freezing and thawing in the presence of water, reactions between the slag and water/atmosphere, reactions caused by rain and changes in the pH of percolating water [8]). The cooling conditions (as well as the chemical composition) determine the formation of a crystalline or amorphous mineral structure, which furthermore influences durability, solubility and reactivity of the slags. Also the long-stay in the waste dump leads to mineral alterations by aging and disintegration. This involves the formation of secondary minerals through weathering of the primary minerals. At storage under weather conditions the transformations produced into slags are not complete.

The **blast furnace slag** dumped is a homogeneous material. On average, the blast furnace slag contains about 0.5–0.8 % FeO, 35–42% CaO, 35–40% $SiO_2$, 8–9% MgO, 8–15% $Al_2O_3$, 0.3–1.0% MnO and 0.7–1.5% S in weight. The slag basicity $CaO/SiO_2$ is in the range of 0.95–1.25 [9, 10]. The results of analytical quantitative determinations showed the main oxides existent in the ferrous slags from Galati metallurgical plant (Table 1) [11].

The mineralogy and physical properties of this slag are influenced by itschemical composition and cooling conditions. The literature shows that the most common minerals found in the air-cooled blast furnace slag are akermanite, gehlenite, wollastonite, dicalcium silicate, merwinite, anorthite, monticellite [12]. The liquid slags were discharged to waste dump by ladles and naturally cooled into ambient air with temperature variable depending on the season. So, it has been provided a slow cooling by air contact from around 1500 °C (the tapping temperature of slag from blast furnace) and it was formed a crystalline structured rock-like mass. The degree of crystallization depends primarily on the mineralogical structure of the basic constituents of slag. In slow cooling, BF slags precipitate into crystallized silicate phases (for example, melilite and merwinite). The main component of basic slags is dicalcium silicate. This compound has the property that at a slow cooling it goes through several states. Its structural changes, accompanied by volume expansion of

approximately 12vol-%, can convert the slag into a powdery material. For the slag dumped the alteration of minerals can occur due to weathering processes in nature. The minerals react with moisture, $CO_2$, etc. during storage and to some degree they undergo phase transformations [13]. This is the so called mineral aging process, when a primary mineral undergoes transformation and a secondary mineral is formed. In slow cooled slag the only crystalline compound which has cementitious properties is $\beta$-$2CaO \cdot SiO_2$. Due to the low iron content, the BF slag is not considered as valuable iron-rich waste justified to be recovered in steel mill plant. After excavation this is sorted, crushed and valorised as aggregate, ballast and lightweight building material, not as a cementing component.

**Table 1.** *Composition of metallurgical slag from metallurgical plant Galati*

| Type of slag | Chemical composition, [%] | | | | | | | | |
|---|---|---|---|---|---|---|---|---|---|
| | CaO | MgO | $SiO_2$ | $Al_2O_3$ | $Fe_2O_3$ | FeO | MnO | Other | S |
| BF slag | 41 | 7-8 | 36 | 7-9 | 0.8 | 0.5-0.8 | 0.2-1 | ~1.3 (P) | 0.8 |
| Steel slag | 42-44 | 5-7 | 30-35 | 2.5-3.7 | 15-20 | 2.5-5 | 3-6 | ~0.5 (Cr and V) | - |

The **steel making slags** stored in dump are BOF slags and EAF slags. Their chemical properties are variable. So is more difficult to use the steel slags compared to the BF slag. On average, the BOF slag in literature has Fe 2–8%, CaO 40–60%, MgO 3–10%, MnO 1–8%. The slag basicity from BOF slag is in the range of 3.5. The major phases present in LD slag are dicalcium ferrite, calcium alluminate and wüstite, but it contains also some reactive mineral phases, such as $2CaO \cdot SiO_2$, $3CaO \cdot SiO_2$, free CaO and MgO [14, 15]. These are observed in microstructures of slags samples presented in Figure 6.

There are steel slags collected from two areas of the dump.
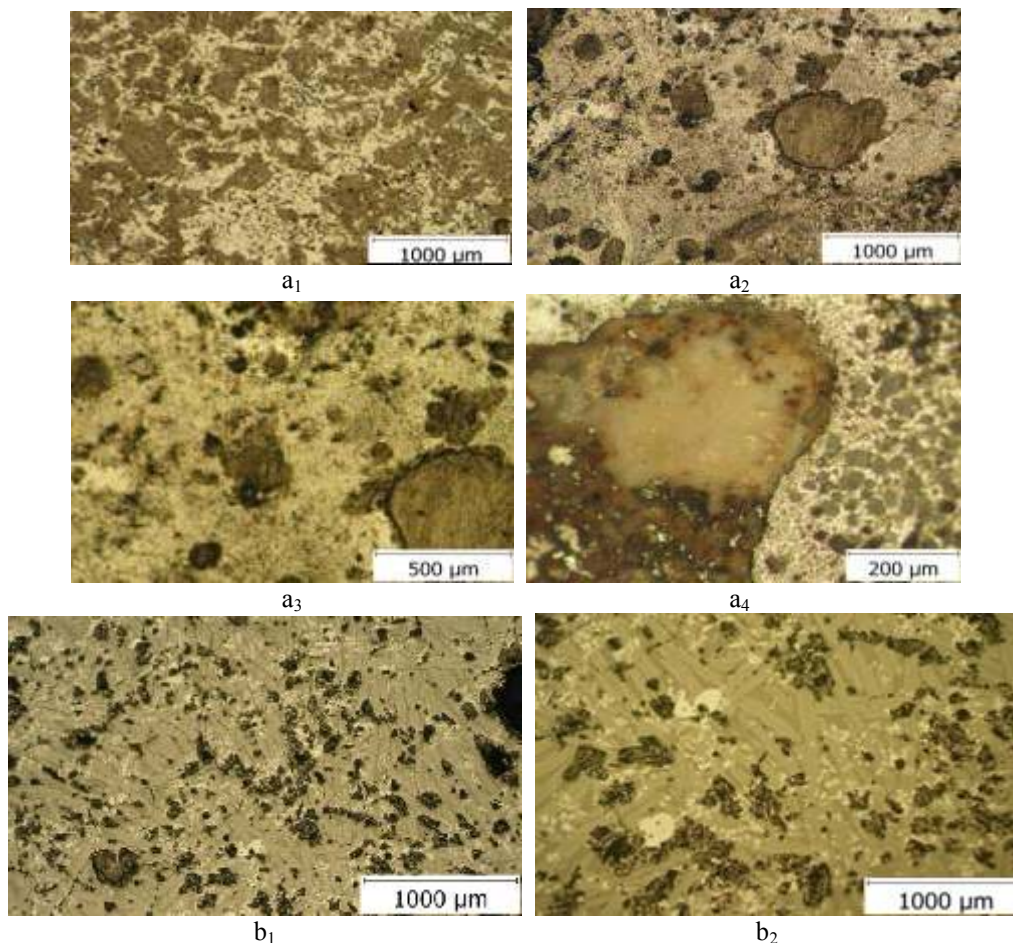


**Fig. 6.** *Microstructures of samples of steel slag collected from dump*

The presence of metallic phase can be observed. This is distributed into matrix of slag as white and bright globular formations. A non-uniform structure with very different distribution of metallic phase was observed. In some areas the metallic phases are absent, and other areas are rich in such phases.

The metallic phase appears as bright white formations, predominantly globular. These are dispersed in a matrix of iron silicate with variable proportion of iron oxides (wustite and magnetite). Some vitreous phase was observed. Free CaO (and MgO) has been found in the slags from the integrated steel plant of Galati (Table 1) [11]. Because of their lime contents (and periclase) they expand in reaction with water. After this expansion they can be stabilized by "natural ageing" for long periods outdoors in natural rainfall [16]. The slow cooling under natural condition of humidity and the longer stationary period in the dump can ensure the conditions required for minerals crystallizing and chemical stabilization of this slag. Slow air cooling favours to a great extent crystallization but, at the same time, allows the unfolding of polymorphic transformation reactions of type β calcium silicate into γ calcium silicate in basic slag (the pH of ferrous metallurgical plant slag varies from 10 to 12) [11].

Also these steel slags (in comparison to BF slags) have higher iron contents than oxides or than fine metallic particles.

The removal of metallic iron from the slag by magnetic separation is necessary. Due to the high content of iron oxides, the steelmaking slags must be exploited for an efficient recovering of their valuable iron units. Magnetic products may be utilized as a component for sintering mixture.

## 2.3. Valorisation solutions of old slags

The impressive slag dump near Galati can be considerably reduced by introducing into the economic circuit the mineral aggregates obtained by processing metallurgical slag in accordance with legal requirements.

The metallurgical slag as aggregates is valorised in various applications in the construction industry. Their performance characteristics have proved effective in their use in Romania since 2002.

The steel slag is exploited from slag dump by mechanical operations: excavation, transport, crushing, milling, magnetic separation, and screening (Figure 7).



**Fig. 7.** *Plant for exploitation of old slag* [16]

Several different types of materials with variable iron content and different grain size are obtained: larger pieces of the steel scrap; diverse non-magnetic fines or coarse non-magnetic fractions. Also, the non-magnetic fractions are sorted by classes, more or less rich in iron.

The high iron fractions sorted from steel slag are valuable for internal recycling into sintering process. The nonferrous fractions are transferred into a special zone. Here the slag is treated for ageing about six months by an amount of water that is sprayed onto its surface. In this way are reduced the expansive oxide contents.

The slag aggregates called *Lidonit* are obtained from steel slag excavated from the slag dump of Galati.

From the technological point of view, the obtaining of this product is similar to the classical method for producing natural aggregates exploited from rock quarry [17].

Only a supplementary pre-treatment for removal of metallic rich iron fractions from the slag by magnetic separation is necessary.

After crushing, sieving and removal of magnetic matter, they achieve granularity appropriate to different applications. Another product from slag named *Benolite* is currently undergoing certification for use [18].

The slag from blast furnace is processed through a screening and crushing plant and is processed into many sizes for use primarily as a construction aggregate.

## 3. Conclusions

The metallurgical slags landfilled in the dump located near Galati are a permanent source of pollution of the environment and people's health.

The EU Directives and national legislations demand their elimination. Also the remediation and restoration of areas contaminated are imposed. The recycling solutions can be applied. For each type of slag (BF slag and steel slag) the solution that must be applied are different.

The solution is also different as fo the new slag generated by the activity of integrated steel mill plant. The chemical composition, cooling condition, action of variable weather conditions lead to some structure transformation in the slag dumped. Several different types of structures and fractions of slag with variable iron content and different grain size are observed. The slags processed in special flow are used primarily as construction aggregates.

The high iron fractions are recycled in the steel plant of Galati, into sintering process.

## References

[1]. *** - *Local Agenda 21 – Local plan for sustainable development of Galati municipality*, 2002.

[2]. A. Sznajder - *Effects of EU Accession on the Politics of Privatization*, The Steel Sector in Comparative Perspective, http://blog.richmond.edu/asznajder/files/2008/02/sznajder_erbe_des_beitritts.pdf.

[3]. R. Berger - *Romanian Steel Industry: Forging ahead*, Romanian Business Digest, 2004.

[4]. *** - *Management of Steel Plant Solid Wastes*, http://www.tifac.org.in/index.php?option=com_content&id=736&Itemid=205.

[5]. M. Luca, R. P. Balan - *Monitoring the exploitation of the industrial waste dump*, Buletinul Institut Pol. din Iasi, Tomul LIV (LVIII), Fasc. 2., Hidrotehnica, 2008, p. 25-36.

[6]. *** - *Eurofer,* Review blast furnace slag processing, 2007, p. 5.

[7]. M. H. Joulazadeh, F. Joulazadeh - *Slag; Value Added Steel Industry Byproducts*, Archives of Metallurgy and Materials, vol. 55, Issue 4, 2010, p. 1137-1145.

[8]. Y. Sueoka, M. Sakakibara - *Primary Phases and Natural Weathering of Smelting Slag at an Abandoned Mine Site in Southwest Japan*, Minerals, 2013, 3, p. 412-426.

[9]. M. Reuter, Y. Xiao, U. Boin - *Recycling and environmental issues of metallurgical slags and salt fluxes*, VII International Conference on Molten Slags Fluxes and Salts, The South African Institute of Mining and Metallurgy, 2004.

[10]. J. Brito, N. Saikla - *Recycled Aggregate in Concrete*, Use of industrial, Construction and Demolition Waste, Chapter 2, Industrial Waste Aggregates, 2013, www.springer.com.

[11]. M. Cioroi, L. Nistor (Cristea) - *Recycling Possibilities of Metallurgical Slag*, The Annals of "Dunarea de Jos" University of Galati, Fascicle IX, Metallurgy and Materials Science, no. 1, 2007, p.78-82.

[12]. D. W. Lewis - *Properties and Uses of Iron and Steel Slags*, Symposium on Slag National Institute for Transport and Road Research South Africa, February, 1992, http://www.nationalslag.org.

[13]. S. Diener - *Mineral phases of steel industry slags used in a landfill cover construction*, Master thesis, Technische Universität Dresden, 2006.

[14]. T. A. Branca, V. Colla - *Possible Uses of Steelmaking Slag in Agriculture: An Overview*, www.intechopen.com.

[15]. F. Engström - *Mineralogical Influence of Different Cooling Conditions on Leaching Behaviour of Steelmaking Slags*, Licentiate thesis, Luleå University of Technology, Department of Chemical Engineering and Geosciences, Division of Process Metallurgy, 2009.

[16]. *** - *Lidonit. Agregate din zgura de otelarie*, http://www.dsu.ro/ro/lidonit.php.

[17]. L. Cristea - *Utilizarea agregatelor Lidonit la construcțiile de drumuri*, Revista Construcțiilor decembrie 2012, p. 38-39, http://www.revistaconstructiilor.eu.

[18]. L. Cristea, D. Iofcea, M. Badiu - *Atestarea conformitatii agregatelor „Benolite" pentru aplicarea marcajului CE*, Revista Constructiilor, nr. 83, iulie 2012, p. 36.

# RESEARCH ON THE INFLUENCE OF THE COMPLEMENTARY PHASE PERCENTAGE ON THE PROPERTIES OF COPPER-BASED COMPOSITES

**Simona BOICIUC, Petrică ALEXANDRU**
"Dunarea de Jos" University of Galati, Romania
e-mail: simonaboiciuc@yahoo.com

## ABSTRACT

*The article presents the method to obtain copper matrix composite with Cu-Al-Fe alloy particles as complementary phase. The samples were obtained by powder metallurgy methods using different percentages of complementary phase: 10, 20, 30, 40, 50% Cu-Al-Fe of average size of 100 μm. After cold pressing at a pressure of 863 MPa samples were sintered at 910 °C for 90 minutes. Characterization of the samples was focused on the microstructural aspects and abrasive wear behavior.*

KEYWORDS: powder metallurgy, microhardness, abrasive wear

## 1. Introduction

The major essential advantage of composites is the possibility to modulate the properties, thus obatining a very large range of materials whose use may extend to almost all technical fields.

In most cases, the composite material comprises a core/base matrix, where the additional/complementary material is dispersed into as fibers or particles, and the main properties that are intended to be obtained in an improved form are: breaking resistance, resistance to wear, density, high temperature resistance, surface hardness, dimensional stability, vibration damping ability [1, 4, 8]. Metal matrix composites have been developed primarily from the need to reduce the weight of machinery and equipment and to extend their service life, a very important objective in the aviation industry or the construction of vehicles. Compared to polymer matrix composites, metal composites are more resistant to high temperatures and are not flammable or hygroscopic. As complementary material, use is made of metal fibers, nonmetal fibers or various particles diversified by their chemical nature, type and size [1, 4, 8].

Copper chosen as matrix has in this case very good electrical and thermal conductivity, as well as the advantage that it can be manufactured/processed easily. It is used in the production of conducting and superconducting composite materials as well as those intended for bearings and filters [1, 4, 8]. Particles, large or small (micro, nano), spherical, flat or of other configuration, are mainly used to produce composites of high resistance to wear, ensuring a lightweight product, outstanding dimensional stability and high vibration damping capacity [1, 4, 8]. Biphasic aluminum bronzes which form the complementary phase particles are known for their outstanding resistance to abrasion, cavitation, corrosion, etc., being used in naval, petrochemical, chemical industry, etc. (bearings, rods, valve, pump impellers, shafts sleeves for anchor, worm and impeller of the compressor, etc.). In the special Cu-Al alloys there are additions of Fe, Ni, Mn, which change the solubility of aluminum in copper and lead to new phases. Iron finishes the grain and improves mechanical and anti-friction properties. Nickel and manganese increase corrosion resistance and contribute to additional hardening by alloying solid solutions [1, 4, 8].

The research undertaken in this paper aimed to achieve, by powder metallurgy methods, copper matrix composites using the complementary phase of Cu-Al-Fe alloy particles. Samples thus obtained were characterized in terms of microstructural and wear behavior.

## 2. Experimental conditions

To obtain the samples two types of powder were used: one composed of pure copper which has ensured the matrix and another one of Cu-Al-Fe alloy that formed complementary phase, and has the following chemical composition: 9.5%Al; 2.2%Fe;
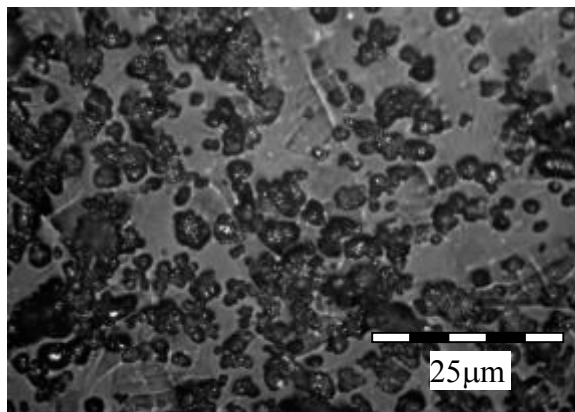
88.3%Cu. The size of the powder particle Cu-Al-Fe was about 100 μm.

Copper powder has an irregular shape determined by the atomization in water and Cu-Al-Fe alloy powder has a spherical shape due to gas atomization. The micrographs of this powder are shown in Fig. 1.
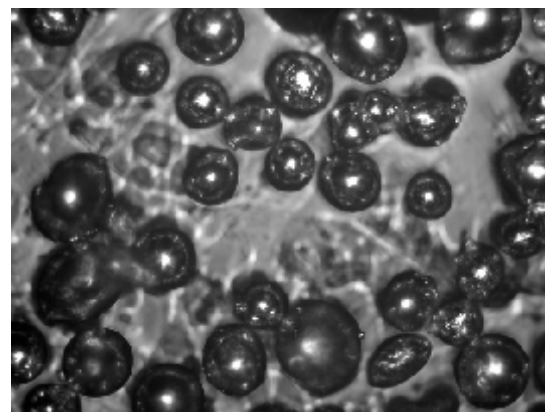
There have been several samples with different concentrations of complementary phase as shown in Table 1.

*Table 1. Composition of powder tablets*

| Sample code | Composition |
|---|---|
| A1 | 90%Cu + 10% Cu – Al – Fe |
| A2 | 80% Cu + 20% Cu – Al – Fe |
| A3 | 70%Cu + 30% Cu – Al – Fe |
| A4 | 60% Cu + 40% Cu – Al – Fe |
| A5 | 50%Cu + 50% Cu – Al – Fe |

The sample tablets were cylindrical of approximately 8x6 mm.

The compression method used was cold pressing by the universal mechanical testing machine. Powder compacting pressure used was 863 MPa, determined after making several attempts.

Sintering of powder tablets was carried out in an electric furnace. The sintering temperature was 910 °C and 90 minutes exposure time. After sintering, all samples were cooled slowly in the furnace.

The samples were placed in a ceramic cylinder and graphite was added. The graphite has an important role in the prevention of entry of the cooling air inside the cylinder, thus ensuring a protection atmosphere.

The main purpose of sintering is to reduce porosity. The sintering process is most often accompanied by changes in the material, some desired and some not: there are changes in the mechanical strength, hardness; also are affected by the size and shape of the particles; there is variation in the shape and size of the pores; the chemical composition and the crystal structure can be altered due to the chemical reaction processes in solid phase.



a.                                    b.

*Fig. 1. Aspect of copper powder – a, and Cu-Al-Fe alloy powder – b*

The microscopic analysis of the powders and samples obtained was performed using a microscope Neophot 2 with computerized data acquisition.

The microhardness measurements were carried out using microdhardness meter PMT 3.

The wear behavior of the samples obtained was studied using the method for determining the mass abrasion wear on a rotating disk. It uses a friction pin/disc coupling, class IV-1. The method involves successively pressing, under the same conditions, the two samples of size 8x6 mm, one of the examined material, the product of composite powders and the other of the material chosen for comparison-sintered copper on a rotating disc covered with sanding paper grit of 120 granulation. A mechanism for radial displacement of the specimen by 0.5 mm/rev provides

spiral path on the rotating disk surface. A device for applying a load of 6229 N ensures pressing of the specimen perpendicular to the sandpaper to 0.123 $N/mm^2$ pressure. At a speed disc of 25 rev/min, a lenght of 11.6 m has been run.

## 3. Results and discussions

For a metallographic study, powders were embedded in a cyanoacrylate adhesive and metallographically prepared by grinding and chemical attack with a suitable reagent. Microscopic analysis (Fig. 2) performed on copper powder particles embedded, polished and attacked with ferric chloride highlights their irregular shape and good compactness. Microhardness determined on the

polished section of the copper particles under 10 g load was HV0.01 = 516.2 MPa.

In the case of Cu-Al-Fe alloy powder, the microscopic analysis on samples embedded, polished and attacked with ferric chloride highlights spherical particles and their good compactness. The particles feature a very fine acicular structure of martensite type. Microhardness determined on the polished section of the particles under 100 g load was HV0.1 = 2766.5 MPa.



a.                                b.
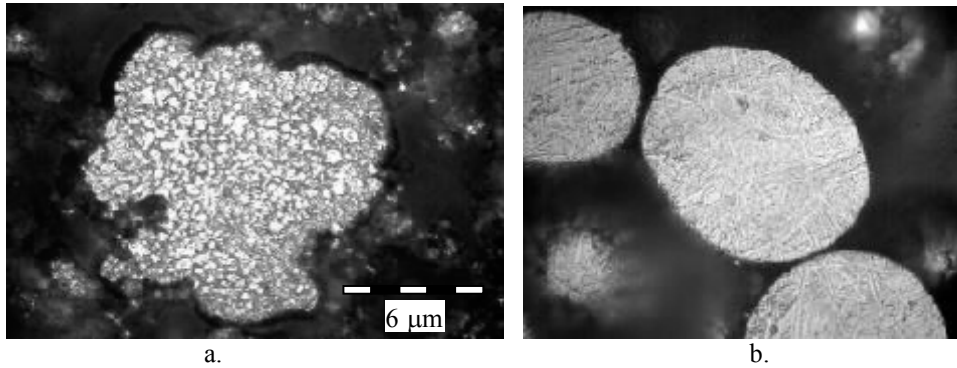
**Fig. 2.** *Microstructure of Cu powder – a and Cu-Al-Fe alloy powder – b*

Microscopic analysis of pressed tablets reveals the presence of pores and their shape (Figure 3).

Looking at Fig. 3 it can be seen that with the increasing of the powder alloy Cu-Al-Fe, of spherical shape, there is also an increase in the included phase. However there is a decrease in the sample compactness with increasing percentage of the included phase.

This is due to the different capacity of deformation of the two types of powder.

Fig. 4 illustrates the microscopic appearance of the unattacked sintered samples. It is noted their reduced porosity and the higher compaction.

Fig. 5 shows the microscopic appearance of the tablets obtained with Cu matrix reinforced with Cu–Al–Fe alloy particles, sintered and attacked with ferric chloride reagent. It can be seen that their structure consists of Cu showing twinned with particles of Cu–Al–Fe alloy comprising intermetallic compounds Fe–Al.



A1- 90% Cu + 10% Cu – Al – Fe



A2- 80% Cu + 20% Cu – Al – Fe



A3 - 70% Cu + 30% Cu – Al – Fe



A4 - 60% Cu + 40% Cu – Al – Fe

| | |
|---|---|
| A5 - 50% Cu + 50% Cu – Al – Fe | 100% Cu |
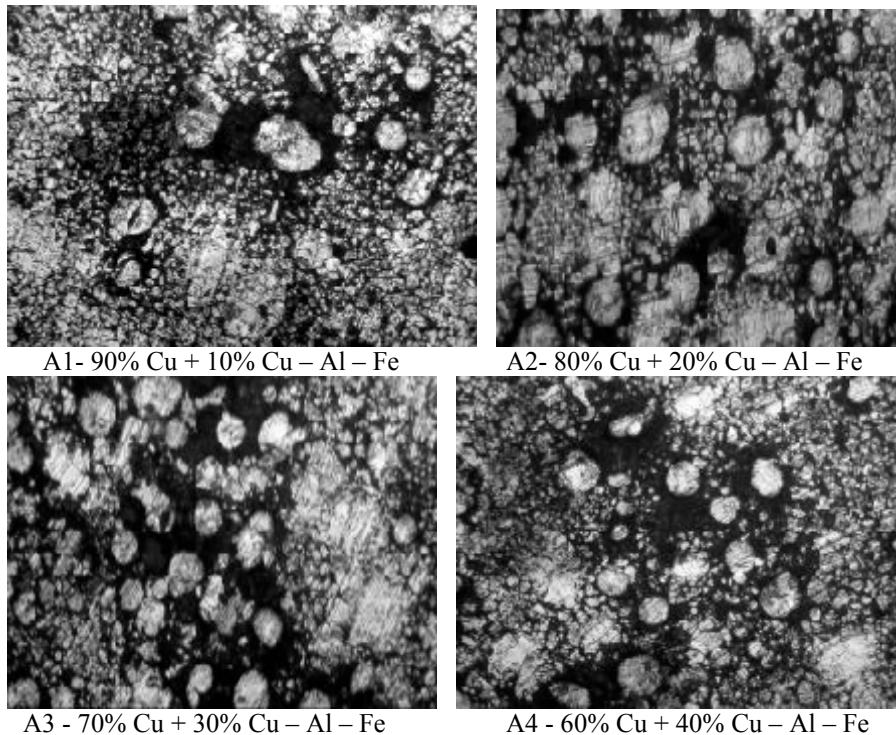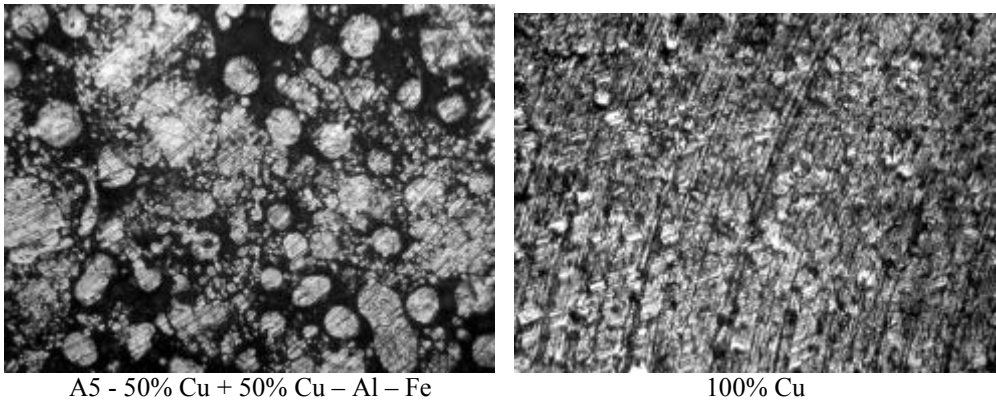
**Fig. 3.** *Microstructure of pressed powder tablets in Cu matrix reinforced with Cu–Al–Fe alloy particles*



| | |
|---|---|
| A1- 90% Cu + 10% Cu – Al – Fe | A2- 80% Cu + 20% Cu – Al – Fe |
| A3 - 70% Cu + 30% Cu – Al – Fe | A4 - 60% Cu + 40% Cu – Al – Fe |
| A5 - 50% Cu + 50% Cu – Al – Fe | 100% Cu |
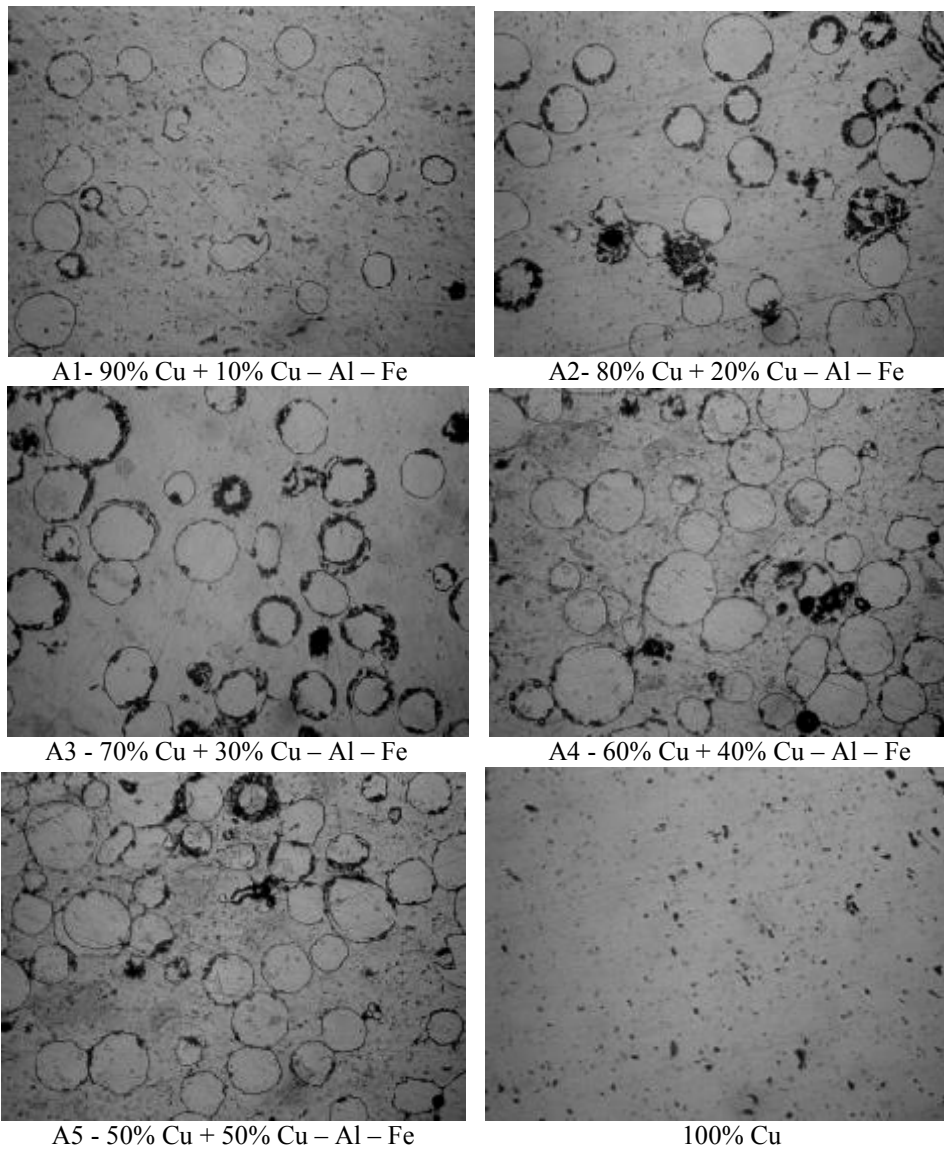
**Fig. 4.** *Microstructure of sintered, unattacked powder tablets in Cu matrix reinforced with Cu–Al–Fe alloy particles*

A1- 90% Cu + 10% Cu – Al – Fe

A2- 80% Cu + 20% Cu – Al – Fe

A3 - 70% Cu + 30% Cu – Al – Fe

A4 - 60% Cu + 40% Cu – Al – Fe

A5 - 50% Cu + 50% Cu – Al – Fe

100% Cu
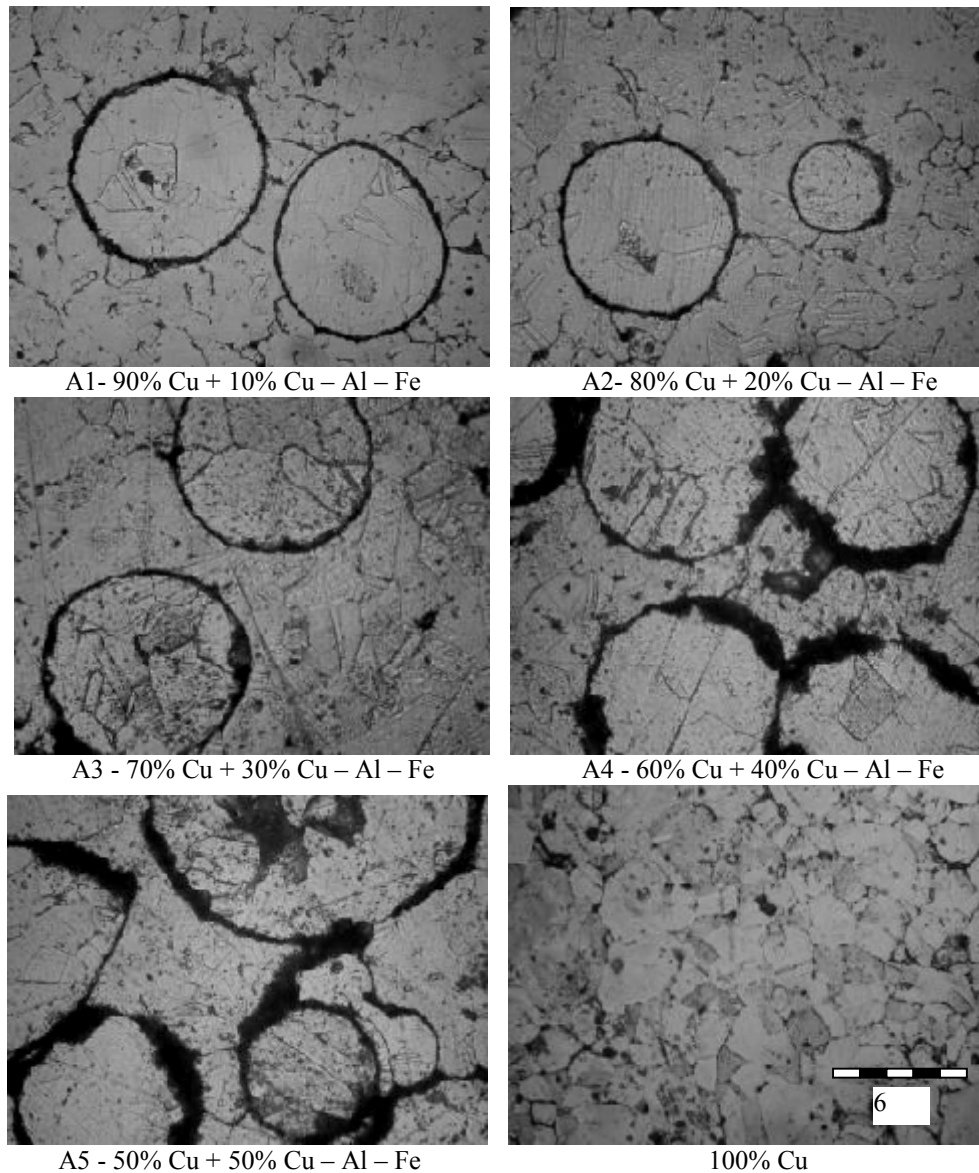
***Fig. 5.*** *Microstructure of sintered powder tablets in Cu matrix reinforced with Cu-Al-Fe alloy particles, subjected to ferric chloride attack*

***Table 2.*** *Abrasive wear behavior of sintered powder products*

| Samples | Initial mass [g] | Final mass [g] | Mass wear [g] | Wear/length run [g/m] |
|---|---|---|---|---|
| Cu | 23.7362 | 23.6964 | 0.0398 | 0.003431 |
| A1 - 90% Cu + 10%  Cu – Al – Fe | 24.1758 | 24.1434 | 0.0324 | 0.002793 |
| A2 - 80% Cu + 20%  Cu – Al – Fe | 24.1611 | 24.1249 | 0.03620 | 0.00312 |
| A3 - 70% Cu + 30%  Cu – Al – Fe | 24.1358 | 24.0761 | 0.0597 | 0.00514 |
| A4 - 60% Cu + 40%  Cu – Al – Fe | 24.085 | 24.0242 | 0.0608 | 0.005241 |
| A5 - 50% Cu + 50%  Cu – Al – Fe | 24.5141 | 24.452 | 0.0621 | 0.005353 |

The Cu sintered samples and the composite ones were tested to wear on rotary disk and sanding paper. The results obtained are shown in Table 2, which are the average of three determinations. Analyzing the Table above we can see that the best reaction to wear is that of samples A1 and A2. The increase in the proportion of powder Cu-Al-Fe by 20% leads to a decrease in wear resistance because of their pluking during the test. This may also be due to the reduced compaction of the tablets when increasing the

included phase. These particles, running between the abrasive surface and the surface of the sample being analyzed, give rise to additional wear of the surface examined, Fig. 6. In Fig. 7-12 there are 3D images of the surfaces obtained after the abrasive wear test conducted with an Image J software. Analyzing

Figures 7-12 we see good wear behavior from samples A1 and A2, better than that of Cu sintered sample. In the darker areas it can be observed the absence of reinforcement particles that, running between the sample surface and abrasive, have led to additional wear.
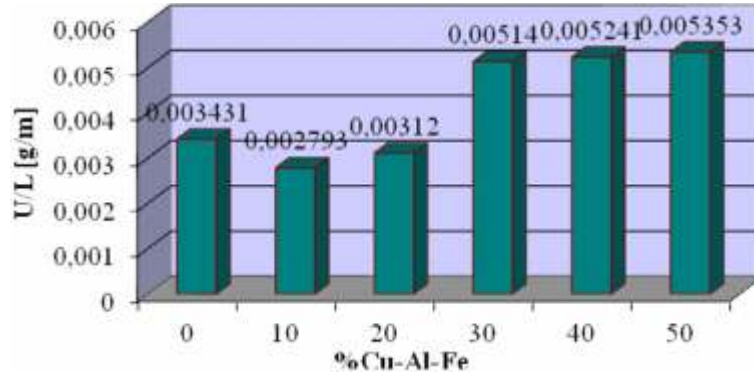


**Fig. 6.** *Abrasive wear behavior of sintered powder products*
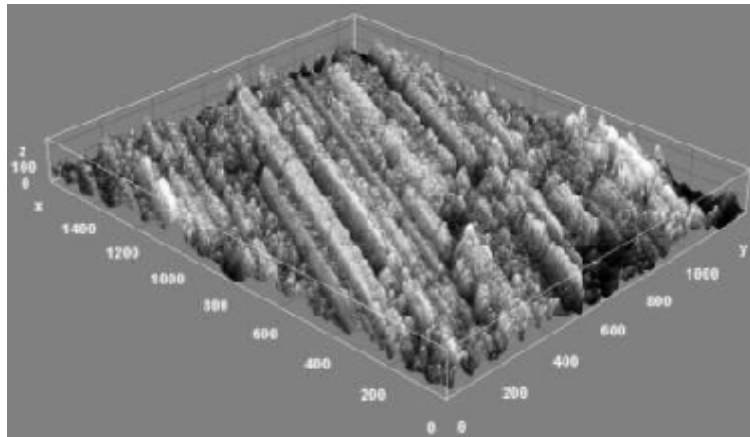


**Fig. 7.** *3D image of the Cu sample surface subjected to abrasive wear*
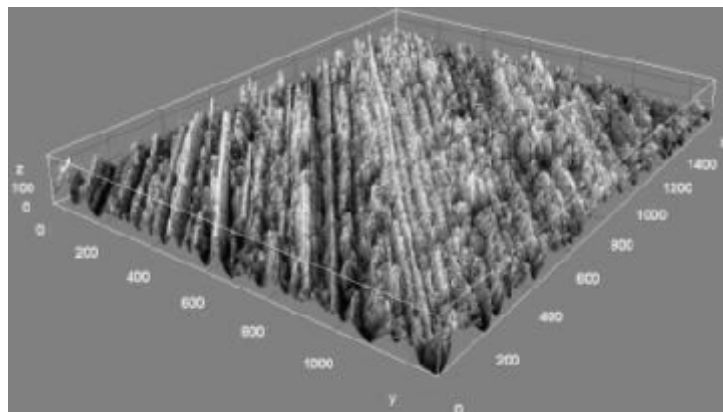


**Fig. 8.** *3D image of the A1 sample surface subjected to abrasive wear*
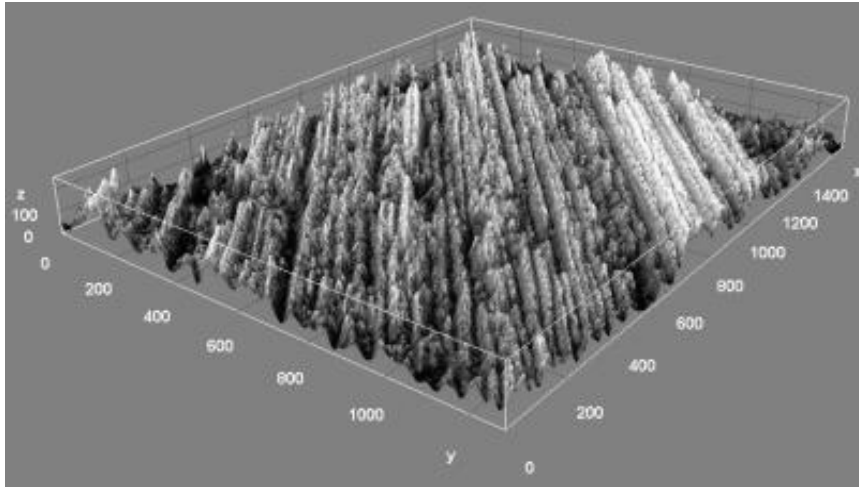
**Fig. 9.** *3D image of the A2 sample surface subjected to abrasive wear*
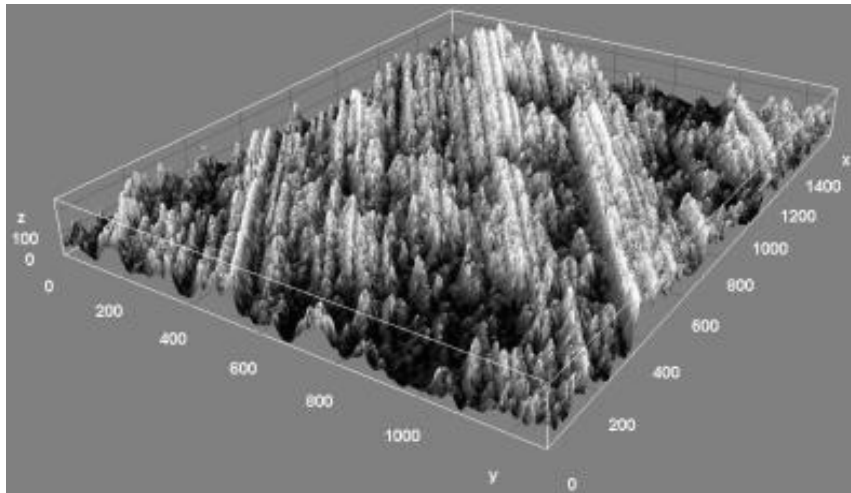


**Fig. 10.** *3D image of the A3 sample surface subjected to abrasive wear*
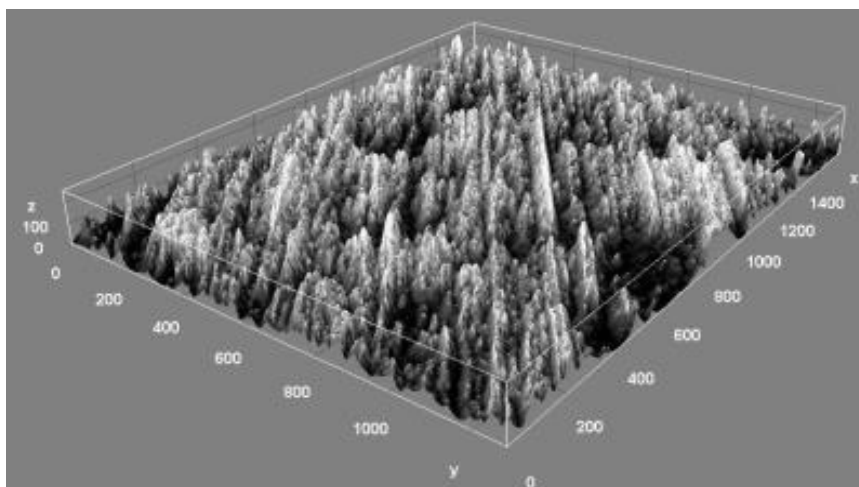


**Fig. 11.** *3D image of the A4 sample surface subjected to abrasive wear*
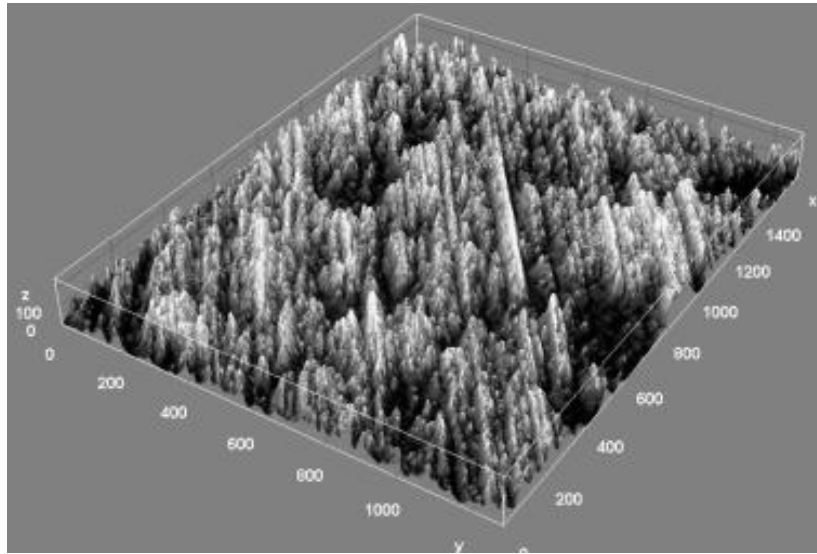
***Fig. 12.*** *3D image of the A5 sample surface subjected to abrasive wear*

## 4. Conclusion

❖ Obtaining composites reinforced with particles of CuAlFe alloy revealed the following:

❖ The powder used in experimental research as matrix has irregular shape caused by atomization in water;

❖ The powder used in experimental research as reinforcement element has spherical shape specific to atomization in gas;

❖ The compaction pressure was 863 MPa;

❖ It has been found that with increased content of CuAlFe powder, of spherical shape, it is increasing the percentage of the inclusion; however there is a decrease in the degree of the sample compactness obtained through different deformation capacity of the powders;

❖ Tablets powder sintering at 910 °C, for 90 minutes has reduced their porosity;

❖ Microstructure of composites reinforced with Cu-Al-Fe alloy particles show a relatively uniform distribution of the included phases; it is made from Cu matrix consisting of twinned particles and copper based alloy comprising intermetallic compounds (FeAl$_3$) distributed in a very fine mass;

❖ As far as the resistance to abrasive wear is concerned, it was found that the best reaction to wear is shown by samples A1 and A2 with 10 and 20% Cu-Al-Fe alloy; the increase in the Cu-Al-Fe powder proportion over 20% leads to a decrease in wear resistance due to their plucking during the test. These particles give rise to additional wear of the surface considered;

❖ The 3D analysis of the surface resulting from the wear test conducted with Image J software, shows additional wear as a result of the separation of the hard particles from the Cu-Al-Fe alloy.

## References

[1]. H. N. Ch'ng, J. Pan - *Modelling microstructural evolution of porous polycrystalline materials and a numerical study of anisotropic sintering*, J. Comput. Phys., 204, 2005, p. 430-461.
[2]. D. Bernard, D. Gendron, J. M. Heintz, S. Bordere, J. Etourneau - *First direct 3D visualisation of microstructural evolutions during sintering through X-ray computed microtomography*, Acta Materialia, 53, 2005.
[3]. K. K. Chawla - *Composite Materials: Science &Engineering*, 2$^{nd}$ edition, Springer-Verlag, New York, 1999.
[4]. R. M. German - *Sintering Theory and Practice*, John Wiley & Sons, New York, 1996.
[5]. Deleanu L., Ciortan S. - *Evaluating Tribological Damages by 3D profilometry*, EHD Lubrication and Traction, May 6-8, 2010 VAREHD 15, 2010, Suceava, Romania, http://www.varehd.usv.ro/, ISSN 1844-8917, p. 163-169.
[6]. E. Drugescu, O. Potecaşu, F. Potecaşu, M. Marin, V. Mereuta, L. Deleanu - *Mechanical properties, abrasive wear behavior and surface quality evaluation of new sintered iron alloys*, Rotrib, Universitatea Tehnică „Gh. Asachi", Iaşi, Tomul LVII (LXI), fasc. 1, 2011.
[7]. Deleanu L., Cantaragiu A., Ciortan S. - *Surface Quality evaluated by 3D Functional Parameters,* Proceedings of 10th Intern. Conf. "Research and Development in Mechanical Industry", RaDMI 2010, 16-19 September, Donji Milanovac, Serbia, p. 311-318.
[8]. T. Surdeanu, M. Perneş - *Piese sinterizate din pulberi metalice,* Editura Tehnică, Bucureşti, 1984.

MANUSCRISELE, CĂRŢILE ŞI REVISTELE PENTRU SCHIMB, PRECUM ŞI ORICE
CORESPONDENŢE SE VOR TRIMITE PE ADRESA:

MANUSCRIPTS, REVIEWS AND BOOKS FOR EXCHANGE COOPERATION, AS WELL
AS ANY CORRESPONDANCE WILL BE MAILED TO:

LES MANUSCRIPTS, LES REVUES ET LES LIVRES POUR L'ECHANGE, TOUT AUSSI
QUE LA CORRESPONDANCE SERONT ENVOYES A L'ADRESSE:

MANUSCKRIPTEN, ZIETSCHRITFTEN UND BUCHER FUR AUSTAUCH SOWIE DIE
KORRESPONDENZ SID AN FOLGENDE ANSCHRIFT ZU SEDEN:

**AFFILIATED WITH:**
        **- ROMANIAN SOCIETY FOR METALLURGY**
        **- ROMANIAN SOCIETY FOR CHEMISTRY**
        **- ROMANIAN SOCIETY FOR BIOMATERIALS**
        **- ROMANIAN TECHNICAL FOUNDRY SOCIETY**
        **- THE MATERIALS INFORMATION SOCIETY**
            **(ASM INTERNATIONAL)**

# Edited under the care of
# Faculty of
# MATERIALS AND ENVIRONMENTAL ENGINEERING
**Annual subscription (4 issues per year)**